GROW THICK, ETCH DEEP: NOVEL WAVEGUIDE GEOMETRIES AND MATERIAL SYSTEMS FOR INTEGRATED PHOTONICS

Simen Mikalsen Martinussen

Members of the dissertation committee:

Chairman and secretary:
Prof. dr. J.L. Herek   University of Twente

Supervisor:
Prof. dr. S.M. García-Blanco   University of Twente

Committee Members:
Dr. M.C. Pujol Baiges   Universitat Rovira i Virgili

Prof. dr. J.D.B. Bradley   McMaster University

Prof. dr. W.H.P. Pernice   University of Münster

Prof. dr.ir. G.R.B.E Römer   University of Twente

Prof. dr.ir. D.A.I. Marpaung   University of Twente

GROW THICK, ETCH DEEP: NOVEL WAVEGUIDE GEOMETRIES AND MATERIAL SYSTEMS FOR INTEGRATED PHOTONICS

DISSERTATION

to obtain
the degree of doctor at the Universiteit Twente,
on the authority of the rector magnificus,
prof. dr. ir. A. Veldkamp,
on account of the decision of the Doctorate Board
to be publicly defended
on Friday 9 April 2021 at 16.45 hours

by

Simen Mikalsen Martinussen

born on the 7th of July, 1988
in Bodø, Norway

This dissertation has been approved by:

Prof. dr. S.M. García-Blanco (Promotor)

Table of Contents

Summary

Integrated optics is a key enabler both for the most futuristic and most mundane high tech developments. Quantum computing, searching for exoplanets, rapid medical diagnosis, shorter refresh times on social media and sewage monitoring illustrate the scope of optics. To be useful in such a wide range of applications, it is essential that integrated optical devices can have many functionalities.

Electronic devices can have diverse requirements like fast switching times and low power consumption for a computer, or low noise and high power operation for an amplifier. In the same way, optical devices can have requirements like low loss and low confinement for a sensor, or low loss, high confinement, and dispersion engineering for a frequency comb.

Reaching such different requirements requires different approaches to the very structuring of the device. Often the technique to create one device is antithetical to another. For example, a thin waveguide with low confinement in a sensor is very different from a thick, dispersion engineered waveguide in a frequency comb. Having the technology for one does not guarantee that you can create the other. A wide process window is therefore necessary to make a material system truly versatile.

This thesis documents the development of techniques that extend our range of options for designing optical components in potassium yttrium double tungstate ($KY(WO_4)_2$), silicon nitride (Si_3N_4) and aluminum oxide (Al_2O_3). The focus is on developing dispersion engineered ring resonator structures suitable for nonlinear optics.

Each material system has its own strengths and weaknesses: $KY(WO_4)_2$ is an excellent laser and amplifier material, but developing high index contrast waveguides has been highly challenging so far. Silicon nitride is one of the most successful and versatile materials in integrated optics, however thick layers cannot be grown by the standard methods. Aluminum oxide is also a promising material for lasers, sensors and integration with other materials, but until now the technology to create frequency combs has not existed.

Chapter 2 shows the development of a technique for structuring $KY(WO_4)_2$ using an inductively coupled plasma reactive ion etcher. The developed process is highly efficient, robust with regards to machine instabilities, and has sufficient selectivity to enable several µm deep etching.

Chapter 3 presents a number of techniques that are useful in standard lithography and etching techniques on $KY(WO_4)_2$, especially for deep etching and especially for small samples. Although photoresist spin coating on small samples is problematic because of a resist buildup on the edges and corners, we demonstrate that performing the spin coating in a specially designed chuck can reduce this problem. Furthermore, we present a technique that reduces the risk of sample chipping when performing hard contact lithography. We use an aggressive HCl wet etching procedure to remove redeposited material from $KY(WO_4)_2$ sidewalls. Finally, we combine these techniques with the process from chapter 2 to demonstrate deep etched structures.

Chapter 4 demonstrates a technique for creating pedestal disk resonators in KYW. The technique is based on wet etching a $KY(WO_4)_2$ substrate which has undergone swift heavy ion irradiation. The irradiation process produces an amorphous layer below the surface. We access the amorphous layer by focused ion beam milling through the undamaged surface and etch it away with a gentle version of the wet etch developed in chapter 3. The process is carefully timed to achieve the desired dimensions. The etching generates by-products which we remove by a cleaning TMAH etch, and we show that successive etching and cleaning steps can create caverns 10s of µm deep.

Chapter 5 documents the design, fabrication and characterization of aluminum oxide racetrack resonators exhibiting anomalous dispersion. The sputtered aluminum oxide used has higher refractive index than that used in previous publications, indicating a denser and likely nanocrystalline layer. The microdisks show losses of 0.48 dB/cm and Q factors of 670000, bringing frequency combs closer to realization.

Chapter 6 presents silicon nitride on sapphire, a novel material system suitable for nonlinear optics with access to the mid-infrared. In a single deposition and etching step, we reach unprecedented layer thicknesses of 1350 nm, without cracks and with arbitrary waveguide widths. This remarkable thickness is made possible by an 88% stress reduction enabled by sapphire substrates rather than thermally oxidized silicon.

This thesis expands the repertoire of future researchers and engineers who wish to work with these materials. KY(WO$_4$)$_2$ may now be formed into geometries that can be useful for resonators, and the developed techniques may also be applicable to other crystalline materials with similar fabrication challenges. Nonlinear optics in aluminum oxide, never shown outside of exotic proof-of-concept devices, is now within reach. Silicon nitride nonlinear devices also have a novel path to their fabrication, which may be exploited to realize frequency combs and other devices operating at longer wavelengths than before.

Samenvatting

Geïntegreerde fotonica levert een belangrijke bijdrage aan de meest futuristische en alledaagse high-tech ontwikkelingen. De reikwijdte hiervan beslaat onder andere quantum computers, de zoektocht naar exoplaneten, snelle (medische) diagnostische tests en kortere laadtijden op sociale media. Het is essentieel dat geïntegreerde fotonica een hoge mate van functionaliteit bevat om een zo breed mogelijk spectrum van toepassingen te faciliteren.

Elektronische componenten zijn onderhevig aan diverse criteria, zoals snel schakelen en een laag vermogensgebruik voor computers, of een lage ruis en hoog vermogen voor versterkers. Op eenzelfde wijze zijn er diverse criteria voor optische componenten, zoals een laag verlies en een lage veldopsluiting voor een sensor, of een laag verlies, hoge veldopsluiting en specifieke dispersie voor een frequentie pulstrein.

Verschillende aanpakken voor het ontwerp van optische componenten zijn noodzakelijk om aan zulke verschillende criteria te voldoen. Het blijkt vaak dat de aanpak om een component te realiseren niet compatibel is met die van een ander component. Zo is voor het ontwerp van een sensor een kleine golfgeleider met een lage veldopsluiting gewenst, terwijl de golfgeleider voor een frequentie pulstrein groot moet zijn voor een hoge veldopsluiting en een specifieke dispersie. Het is noodzakelijk om een flexibel en breed toepasbaar proces te ontwikkelen om een zo divers mogelijk veld van toepassingen te bereiken.

Dit proefschrift beschrijft de ontwikkeling van fabricatietechnieken die het toepassingsveld uitbreidt voor optische componenten in de materialen kaliumyttrium dubbel wolframaat ($KY(WO_4)_2$), siliciumnitride (Si_3N_4) en aluminiumoxide (Al_2O_3). Dit proefschrift is met name gericht op de realisatie van ring resonatoren met specifieke dispersie voor non-lineaire optica.

De bestudeerde materialen hebben elk hun zwakke en sterke kanten: $KY(WO_4)_2$ is uitermate geschikt voor lasers en optische versterkers, maar het blijkt lastig om er golfgeleiders met een hoog brekingsindexcontrast mee te maken. Ondanks dat siliciumnitride een van de meest succesvolle en veelzijdige materialen in geïntegreerde fotonica is, kunnen er geen dikke lagen van gemaakt worden met standaard fabricatietechnieken. Aluminiumoxide is

een veelbelovend materiaal voor lasers, sensoren en hybride integratie met andere materialen, maar mist nog de techniek voor frequentie pulstreinen.

Hoofdstuk 2 beschrijft de ontwikkeling van een techniek om $KY(WO_4)_2$ te vormen door middel van een inductief gekoppelde plasma-reactieve ionenetser. De techniek is zeer efficiënt, robuust met betrekking tot machine-instabiliteit, en heeft voldoende selectiviteit om meerdere µm diep te etsen.

Hoofdstuk 3 presenteert verscheidene technieken die bruikbaar zijn in standaard lithografie- en etstechnieken op $KY(WO_4)_2$. Deze zijn vooral geschikt voor diep etsen en voor kleine monsters. Hoewel fotoresist-spincoating op kleine monsters problematisch is vanwege de opbouw van resist op de randen en hoeken, wordt getoond dat het uitvoeren van de spincoating in een speciaal ontworpen houder dit probleem kan verminderen. Verder wordt een techniek gepresenteerd die het risico van afbrokkelen van monsters verkleint bij hardcontactlithografie. Een agressieve HCl-natte etsprocedure is gebruikt om materiaal van $KY(WO_4)_2$-zijwanden te verwijderen. Ten slotte worden deze technieken gecombineerd met het proces uit hoofdstuk 2 om diep geëtste structuren te demonstreren.

Hoofdstuk 4 beschrijft een techniek voor het creëren van $KY(WO_4)_2$-resonatoren op een voetstuk. De techniek is gebaseerd op het nat etsen van een $KY(WO_4)_2$-substraat dat een ionenbestraling heeft ondergaan. Het bestralingsproces produceert een amorfe laag onder het oppervlak. De amorfe laag wordt bereikt door het lokaal verwijderen van materiaal met een gefocusseerde ionenbundel en wordt verwijderd door te etsen met een zachtere versie van de natte ets ontwikkeld in hoofdstuk 3. Het proces wordt zorgvuldig getimed om de gewenste afmetingen te bereiken. Het etsen genereert bijproducten die verwijderd worden door een TMAH-ets. Opeenvolgende ets- en reinigingsstappen kunnen holtes van tientallen µm diep creëren.

Hoofdstuk 5 beschrijft het ontwerp, de fabricage en de karakterisering van aluminiumoxide resonatoren die afwijkende dispersie vertonen. Het gesputterde aluminiumoxide heeft een hogere brekingsindex dan die in eerdere publicaties werd gebruikt, wat kan duiden op een dichtere en nanokristallijne laag. De resonatoren vertonen verliezen van 0,48 dB/cm en Q-factoren van 670.000. Dit is een significant stap voor de realisatie van frequentie pulstreinen in aluminiumoxide.

Hoofdstuk 6 presenteert siliciumnitride op saffier, een nieuw materiaalsysteem dat geschikt is voor niet-lineaire optica voor infrarood golflengtes. In een enkele depositie en etsstap zijn ongekende laagdiktes van 1350 nm bereikt. Het materiaal is niet beschadigd en bevat geen scheuren. Er kunnen willekrige golfgeleiderbreedtes in gerealiseerd worden. Het gebruik van een saffiersubstraat maakt deze dikte mogelijk door een stressvermindering van 88% ten opzichte van het gebruik van thermisch geoxideerd silicium als substraat.

Dit proefschrift breidt het repertoire uit van toekomstige onderzoekers en ingenieurs die met deze materialen willen werken. $KY(WO_4)_2$ kan nu worden gevormd tot geometrieën die nuttig kunnen zijn voor resonatoren, en de ontwikkelde technieken kunnen ook worden toegepast op andere kristallijne materialen met een vergelijkbare lastige fabricatie. Niet-lineaire optica in aluminiumoxide, nooit getoond buiten exotische proof-of-concept-apparaten, is nu binnen handbereik. Niet-lineaire optische componenten van siliciumnitride hebben nu ook nieuwe fabricatiemogelijkheden, die benut kunnen worden voor frequentie pulstreinen en andere apparaten die op langere golflengten werken dan voorheen.

CHAPTER 1

Introduction

1.1 Integrated photonics

In the second half of the 20th century, microelectronics emerged as a world-changing technology. Millimeter-sized circuits gave birth to computers, space travel, the Internet, cell phones and many more technologies that now taken for granted. In the new millennium, similar circuits driven by light rather than electric current stand poised to keep up the momentum of the ever-continuing high-tech revolution. Thanks to technological advances, integrated photonics has evolved from its birth in the 60s [1–6] to its current position as a driving force in the 21st century [7].

Already, photonic microchips are well established in devices such as tunable laser light sources [8,9], transmitters, receivers [10], and multiplexers [11] in fiber optic telecommunication systems Real-time water quality monitoring [12], miniaturized LIDAR [13,14], medical diagnostic devices [15], and gyroscopes [16,17] based on integrated photonics are all in the early phases of commercialization. Applications in computing include high-performance data centers [18,19], quantum information technology [20], and programmable photonic circuits [21,22] for artificial intelligence [23] and machine learning [24]. Improvements in data centers, for example, will enable higher performance online gaming [25], video streaming, and social media [26].

This section will cover the fundamental aspects of integrated photonics. Main focus will be given to concepts required in the design of resonators for generating frequency combs: Resonators, dispersion and third order nonlinear optics.

1.1.1 Fundamentals of waveguide optics

The key enabling element in integrated optics is the dielectric waveguide. It allows light to remain confined to a high refractive index region called the core, surrounded by a lower refractive index medium, which is either air or a cladding. The higher the refractive index contrast, the stronger the light is confined to the core. Not only does this allow for more compact devices than free-space or fiber systems, but a single miniaturized chip also has better inherent mechanical stability.

A schematic example of a strip waveguide is shown in Figure 1.1, in this case 2.2 µm wide, 1.35 µm thick Si_3N_4 ($n\approx2$) on sapphire ($n\approx1.75$), fabricated in this thesis. Figure 1.1(a) shows the shape of the channel waveguide with the direction of propagation into the paper (z), and (b) shows a cross-section along the direction of propagation. Also shown in (b) are the electric field distributions of the fundamental (E_{00}^x) and first-order (E_{01}^x) transverse electric, or x-polarized, modes.
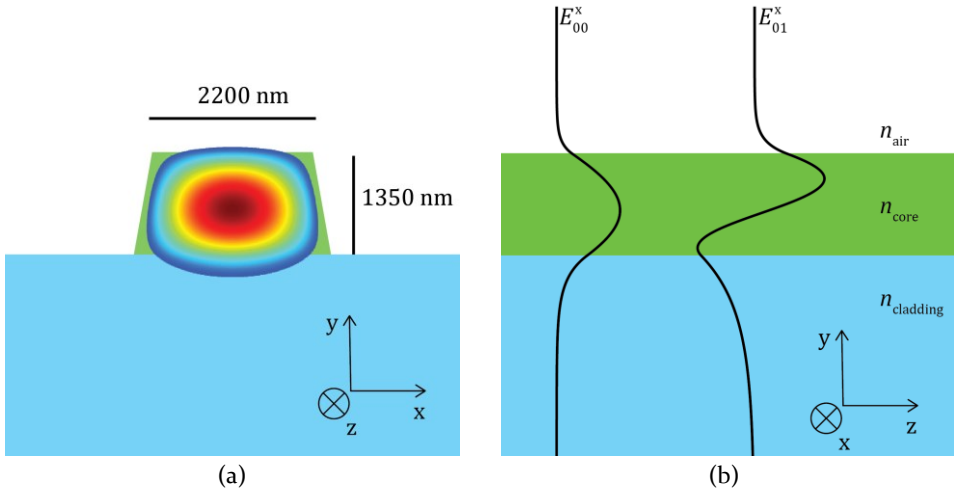
Figure 1.1: Schematic of a Si_3N_4 waveguide on sapphire, with the fundamental TE mode E_{00}^x intensity superimposed. (a) Cross-section view perpendicular to the direction of propagation. (b) Cross-section view parallel with the direction of propagation, showing the electric fields of the fundamental- and first order modes.

The modes can be calculated by discretizing the refractive index distribution and solving Maxwell's equations [27] using a finite difference eigenmode (FDE) approach, taking into account the discontinuities along the waveguide boundaries [28]. This is a powerful approach, which is applicable to arbitrary

waveguide geometries, unlike semi-analytical techniques like Marcatili's method [2], which is only applicable to rectangular waveguides. In this work, mode solving is performed using the commercial software package Ansys Lumerical MODE, using an FDE solver.

Solving Maxwell's equations for a given frequency, f, yields one or more expressions for the electric and magnetic fields, i.e., the optical modes. The total electric field can be written as the sum of several modes

$$\mathbf{E}(\mathbf{r}) = \sum_i \mathbf{E}_i(x,y)e^{-j\beta_i z} \tag{1.1}$$

where β_i is the propagation constant of mode number i, and $\mathbf{E}_i(x, y)$ is the transverse electric field distribution of that mode. The propagation constant is linked to an effective refractive index, $n_{\text{eff},i}$, by the relation

$$n_{\text{eff},i} = \beta_i \frac{\lambda}{2\pi} \tag{1.2}$$

The effective refractive index of a mode describes the propagation of the mode in an inhomogeneous medium, analogous to the material refractive index n. It can be viewed as a weighted average of the core index, n_{core} and the surrounding indices n_{cladding} and n_{air}, depending on the mode overlap with the core and the surroundings. An effective index close to n_{core} indicates a high degree of confinement to the core. A more precise measure of the confinement is given by the effective mode area, given by Equation (1.3) [29].

$$A_{\text{eff}} = \frac{(\iint |E|^2 dxdy)^2}{\iint |E|^4 dxdy} \tag{1.3}$$

1.1.2 Dispersion

In the general case, the effective index is dispersive, i.e. dependent on the frequency of the electromagnetic field. For convenience, the propagation constant of a given mode can be approximated by a Taylor expansion around a central frequency, ω_0, using the m-th order derivatives of β:

$$\beta(\omega) = \beta_0 + \beta_1(\omega - \omega_0) + \frac{1}{2}\beta_2(\omega - \omega_0)^2 + \cdots \tag{1.4}$$

$$\beta_m = \left(\frac{d^m\beta}{d\omega^m}\right)_{\omega_0} \tag{1.5}$$

The significance of this is made visible when considering the group velocity v_g, the group index, n_g and, the group velocity dispersion, $GVD(\omega)$ or $D(\lambda)$ [30].

$$v_g = {1}/{\beta_1} \tag{1.6}$$

$$n_g = {c}/{v_g} = c\,\frac{d\beta}{d\omega} = c\,\beta_1$$

$$= n_{eff} + \omega\,\frac{\partial n_{eff}}{\partial \omega} \tag{1.7}$$

The group index is unitless and carries information about the *slope* of n_{eff}, while D, the group velocity dispersion, describes the *curvature* of n_{eff}, or the slope of n_g. The group velocity dispersion is commonly expressed by either the GVD parameter, with units $fs^2\,m^{-1}$, or as the dispersion parameter $D(\lambda)$, with units $ps\,nm^{-1}\,km^{-1}$. In this thesis, $D(\lambda)$ is most commonly used, and β_2 denotes the group velocity dispersion.

$$GVD(\omega) \equiv \beta_2 = \frac{d}{d\omega}\frac{1}{v_g} \tag{1.8}$$

$$D(\lambda) = -\frac{2\pi c}{\lambda^2}\beta_2 = -\frac{\lambda}{c}\frac{\partial^2 n_{eff}(\lambda)}{\partial \lambda^2} \tag{1.9}$$

Dispersive effects arise both from waveguide dispersion and material dispersion. Waveguide dispersion refers to the influence of the waveguide geometry on β, while material dispersion refers to the wavelength dependence of the bulk refractive index, n.

The material dispersion can be described by many mathematical models, which are appropriate for different materials. For example, metals are commonly modeled with the Drude model [31], dielectrics with the Sellmeier [32] or Cauchy models [33], and compound media with various effective medium approximations [34]. In the Cauchy model, the refractive index of a material is expressed as

$$n(\lambda) = A + \frac{B}{\lambda^2} + \frac{C}{\lambda^4} + \cdots \tag{1.10}$$

where *A*, *B*, *C* and possible higher order terms are material dependent. In simulations, the refractive index is commonly derived from a polynomial fit of sampled data from published datasets such as Palik [35]. Measurements gathered from the individual layers using methods like ellipsometry may also be used. For example, the Cauchy coefficients of the Al_2O_3 material used in this work are given in Table 1.1. These values were measured by ellipsometry on the layers used in chapter 5.

Table 1.1: Measured Cauchy coefficients for Al_2O_3.

A	1.722
B	0.0102
C	0

Figure 1.2 (a) shows the calculated effective index of the fundamental transverse electric (TE) mode of the Si_3N_4 waveguide shown in Figure 1.1 for wavelengths ranging from 1 µm to 2 µm. The effective index, n_{eff}, is strongly dependent on the wavelength, and is linear at first glance. Figure 1.2 (b) shows n_g and $D(\lambda)$, which shed light on the curvature of n_{eff}. It is visible that $D(\lambda)$ is zero at the wavelength where n_g is at a minimum. This point is referred to as a zero-dispersion wavelength.

In the region where $D(\lambda)$ is negative, the dispersion is said to be normal, and positive values of $D(\lambda)$ indicate anomalous dispersion. The anomalous dispersion region is highly significant because of its role in soliton formation [30] and phase matching for nonlinear devices such as frequency combs and optical parametric oscillators [36].
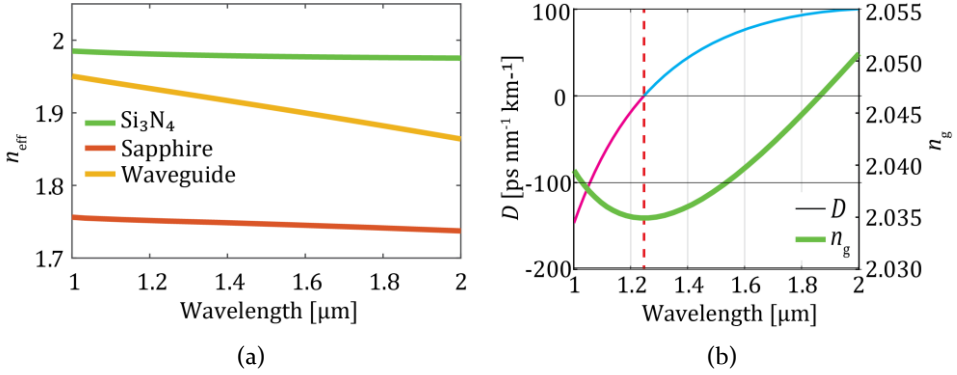
Figure 1.2: (a) Wavelength dependent calculated effective refractive index of the fundamental TE mode in the Si₃N₄ waveguide of Figure 1.1, compared with the bulk refractive indices of Si₃N₄ and sapphire. (b) Group index and group velocity dispersion, $D(\lambda)$ of the same waveguide. The zero-dispersion wavelength is marked with a red dotted line. The pink line indicates normal dispersion, and the cyan line indicates anomalous dispersion.

Although higher order dispersion terms are not described here in detail, they influence the plot of $D(\lambda)$. In the case where there is no third order dispersion, the plot of $D(\lambda)$ should be flat. However, with non-zero third order dispersion $D(\lambda)$ has a slope, and with fourth order dispersion $D(\lambda)$ has a curvature. For these reasons they are essential in determining the zero-dispersion wavelength, which is critical for the operating bandwidth of any device.

1.1.3 Ring resonators

Ring and racetrack resonators are among the most common and versatile building blocks in integrated optics. The fundamental design consists of a waveguide looped back on itself, sufficiently close to a bus waveguide to form a directional coupler. In a ring resonator the waveguide is circular. In a racetrack resonator, a straight section is introduced to make the directional coupler longer to allow for higher tolerances in manufacturing.

As light circulates through the cavity, resonant wavelengths build up in intensity [37]. These wavelengths are not transmitted and appear as sharp dips in the transmission spectrum. These dips are useful for implementing filters [38], switches [39], biosensors [15], and gyroscopes, [16] among other functionalities. The electric field enhancement can also be exploited to use low-power pumps for phenomena that normally need high intensities. This includes ring lasers [40], optical parametric oscillators [41] and Kerr frequency combs [42].
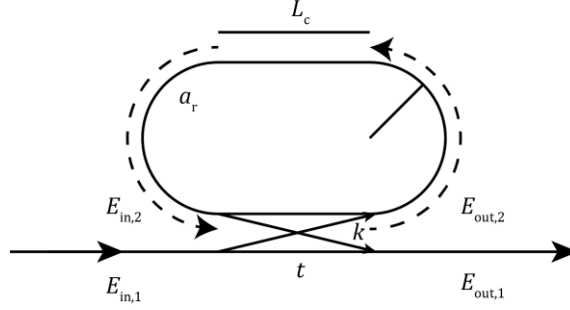
Figure 1.3: Schematic of a racetrack resonator coupled to a single bus waveguide.

A schematic of a racetrack resonator is shown in Figure 1.3. In the following section the transfer function of such a resonator is derived. An electric field, $E_{\text{in},1}$ is injected into the bus waveguide. A complex fraction of this field, k, couples into the resonator field, $E_{\text{out},2}$ while another complex fraction, t, is transmitted along the bus, into the field $E_{\text{out},1}$. In the low coupling regime, the magnitude of k is directly proportional to the length L_c of the coupling region. Assuming lossless and reciprocal coupling, the fields are related [37] by (1.11), where k^* and t^* signify the complex conjugates of k and t:

$$\begin{bmatrix} E_{\text{out},1} \\ E_{\text{out},2} \end{bmatrix} = \begin{bmatrix} t & k \\ -k^* & t^* \end{bmatrix} \begin{bmatrix} E_{\text{in},1} \\ E_{\text{in},2} \end{bmatrix} \tag{1.11}$$

The fields within the racetrack resonator are related by (1.12), with the roundtrip phase shift θ being given by (1.13). Here, a_r is the fraction of the field amplitude that is transmitted around the ring, and is called the loss coefficient:

$$E_{\text{in},2} = a_r e^{j\theta} \cdot E_{\text{out},2} \tag{1.12}$$

$$\theta = \frac{2\pi L n_{\text{eff}}}{\lambda} \tag{1.13}$$

Combining (1.11), and (1.12) gives

$$E_{\text{out},1} = \frac{-a_r + t e^{-j\theta}}{-a_r t^* + e^{-j\theta}} E_{\text{in},1} \tag{1.14}$$

The coupler adds a phase shift φ, such that $t = |t|e^{j\varphi}$. Following this, the power transmission of the resonator can be derived [37]:

$$T = \frac{|E_{out,1}|^2}{|E_{in,1}|^2} = \frac{a_r^2 + |t|^2 - 2a_r|t|\cos(\theta + \varphi)}{1 + a_r^2|t|^2 - 2a_r|t|\cos(\theta + \varphi)} \tag{1.15}$$

When the total phase adds up to a multiple of 2π,

$$\theta + \varphi = 2\pi n, n \in \mathbb{N} \tag{1.16}$$

the resonator is on resonance and the transmission drops sharply. The shape and depth of the resonances is given by the parameters a_r and t [43]. T is minimized when $a_r = t$, which is called critical coupling. The spacing between the resonances, or free spectral range (*FSR*) in units of length, can be derived from (1.13) and (1.16), and is closely approximated [37] by

$$FSR = \frac{\lambda^2}{n_g L} \tag{1.17}$$

Three more important parameters can also be introduced [37], namely the full with half maximum (*FWHM*), the *Q*-factor, the finesse *F*, and the extinction ratio *ER*:

$$FWHM = \frac{(1 - a_r|t|)\lambda^2}{\pi n_g L \sqrt{a_r|t|}} \tag{1.18}$$

$$ER = \left(\frac{(a_r + |t|)(1 - a_r|t|)}{(a_r - |t|)(1 + a_r|t|)}\right)^2 = \frac{T_{max}}{T_{min}} \tag{1.19}$$

$$Q = \frac{\lambda_0}{FWHM} \tag{1.20}$$

$$F = \frac{FSR}{FWHM} \tag{1.21}$$

FWHM is the full width half maximum wavelength of the resonance located at λ_0. The physical interpretation of Q is the number of oscillations of the field in the ring before it is reduced in intensity by a factor e^{-1}. The finesse, *F*, is the number of round-trips of the field in the cavity before its intensity decays by a factor e^{-1} [44]. These figures are essential to the performance of a resonator.

Q and ER determine how sharp the transmission dips are, which is crucial for it to perform as a filter or sensor. F is proportional to the intensity buildup in the cavity, which lowers the threshold for high intensity effects such as lasing and nonlinear frequency generation.

Resonators can be used to extract the propagation losses of the waveguide, by dividing a_r by the round-trip length. To find a_r, a quadratic equation can be constructed using the extinction ratio and finesse, where a_r and t are the roots [43]:

$$A = \frac{\cos(\pi/F)}{1 + \sin(\pi/F)} \tag{1.22}$$

$$B = 1 - \frac{1 - \cos(\pi/F)}{1 + \cos(\pi/F)} \frac{1}{ER} \tag{1.23}$$

$$(a_r, t) = \left(\frac{A}{B}\right)^{1/2} \pm \left(\frac{A}{B} - A\right)^{1/2} \tag{1.24}$$

It is mathematically impossible to distinguish between a_r and t using these equations, as they are symmetric, in the same way as (1.15). However, characterizing resonances over a sufficiently wide wavelength range can reveal which parameter is which. This is because scattering losses decrease at longer wavelengths, while coupling strength increases [33].

In addition to the waveguide second order dispersion, $D(\lambda)$, it is possible to consider another form of dispersion in a resonator. This is the so called "integrated dispersion", $D_{int}(\mu)$, which measures the deviation of the resonance frequencies of the resonator modes from an ideal, evenly spaced frequency grid [45,46]. To derive $D_{int}(\mu)$, the mode spacing is broken down into a polynomial form with many dispersion terms, D_j, $j = 1, 2, \dots$. The dispersion terms D_j are determined by Taylor expanding the resonance frequencies around the pumped mode ω_0:

$$\omega_\mu = \omega_0 + \sum_j \frac{D_j \mu^j}{j!} \tag{1.25}$$

In this approach, $D_1/2\pi$ is the central FSR at ω_0 and D_2 is proportional to the group velocity dispersion (β_2):

$$D_2 = -\left(\frac{2\pi}{L}\right)^2 \frac{\beta_2}{\beta_1^3} \tag{1.26}$$

A more complete derivation of this result is given in appendix A.

Analogous to waveguide dispersion, the integrated dispersion is normal when D_2 is negative, and anomalous when D_2 is positive [47]. In an ideal, nondispersive resonator, only D_1 is non-zero. This leads to a constant *FSR* in terms of frequency, although the *FSR* wavelength spacing depends on the wavelength, as follows from (1.17). Finally, the total integrated dispersion takes into account all dispersion terms as a whole, and is measured as the difference between a mode frequency and it's expected frequency in the absence of dispersion.

$$D_{\text{int}}(\mu) = \omega_\mu - (\omega_0 + D_1\mu) \tag{1.27}$$

A low integrated dispersion is a key factor in designing resonators for nonlinear applications, as an even mode spacing ensures that the frequency-symmetric comb generation process can pump all modes evenly.

1.1.4 Nonlinear integrated photonics

So far, we have assumed that light does not interact with light, and barring intensities that break down vacuum itself [48], this generally holds true. However, the polarization of a medium can become nonlinear under sufficiently intense electric fields. In the case of monochromatic light, the polarization is given by

$$P = \epsilon_0\left(\chi^{(0)} + \chi^{(1)}E + \chi^{(2)}EE + \chi^{(3)}EEE + \cdots\right) \tag{1.28}$$

Where $\chi^{(q)}$ is the q-th order susceptibility tensor. However, not all terms exist in all materials [49]. The even order terms $\chi^{(0)}, \chi^{(2)}$ and higher are only present in non-centrosymmetric crystals. The most important of these are $LiNbO_3$ [50], perovskites [51], certain potassium phosphates [52] and GeTe [49]. $\chi^{(2)}$ effects can also be induced at interfaces [53] and in nanostructured materials like ABC-type nanolaminates [54,55] or strained waveguides [56]. Such $\chi^{(2)}$-active materials can be used as ferroelectrics [49] or for frequency doubling applications [30]. However, they will not be considered further in this thesis.

The even order terms become zero in glasses and centrosymmetric crystals, as can be demonstrated by symmetry arguments considering the full tensorial form of $\chi^{(2)}$ [49]. Furthermore, the higher order terms $\chi^{(5)}$, $\chi^{(7)}$ etc. are vanishingly small [30], and as such typically only $\chi^{(3)}$ needs to be considered.

Third order nonlinearity is responsible for non-linear effects such as Kerr effect, self-phase modulation (SPM), and four-wave mixing (FWM). In the Kerr effect, the refractive index experienced by a high-intensity optical field is given by

$$n = n_0 + n_2 I \tag{1.29}$$

Here n_0 is the linear refractive index discussed previously and n_2 is the nonlinear refractive index. The main consequence of the Kerr effect is the introduction of a phase shift proportional to the intensity. For a beam in a bulk medium this will cause self-focusing [30]. However, in fibers and waveguides it leads to self-phase modulation (SPM). SPM refers to the effect where a pulse accumulates phase more rapidly near its spatiotemporal peak than at the tails. In a Gaussian unchirped pulse in a normally- or non-dispersive medium, this causes spectral broadening and chirping. The first arriving wavelengths are longer than those in the original pulse, and the last arriving wavelengths are shorter. This is called positive chirp. The spatiotemporal pulse length also increases, and nonlinear effects create a complex spectral distribution characterized by several intensity peaks and dips [29].
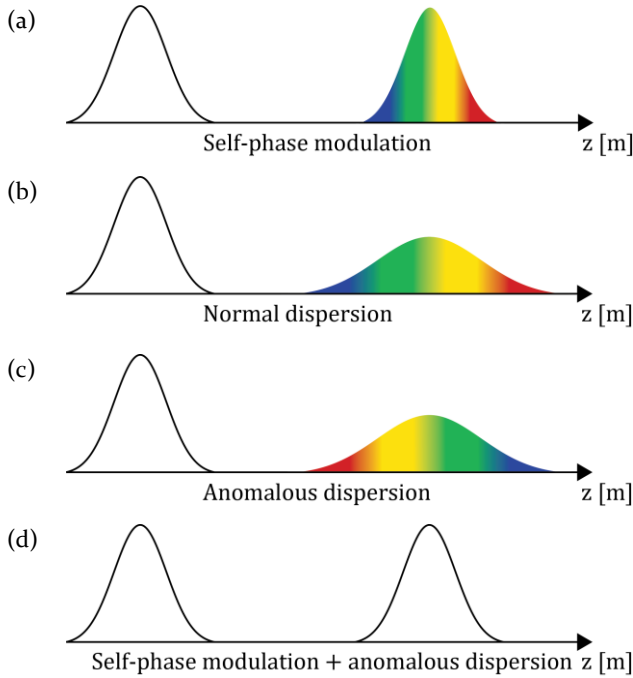
Figure 1.4: The effects of dispersion and SPM on the propagation of an initially unchirped Gaussian pulse. (a) SPM causes a positive frequency shift in the leading edge of the pulse and a negative frequency shift in the trailing edge. This is termed positive chirp. However, in the absence of dispersion this does not cause pulse broadening. (b) In normal dispersion, high frequency components have a higher group velocity than low frequencies. This causes a positive chirp and broadens the pulse. (c) Anomalous dispersion broadens the pulse and causes negative chirp, by the same mechanism as normal dispersion. (d) SPM and anomalous dispersion cancel out, and the pulse retains its shape and spectral distribution.

A pulse containing multiple wavelengths will be chirped in any dispersive medium. Under normal dispersion, long wavelengths see a lower group index and propagate faster, leading to the same chirp as that caused by SPM. However, under anomalous dispersion short wavelengths arrive first, and under specific circumstances it is possible for SPM and anomalous dispersion to cancel each other out and allow a pulse to propagate without chirping or broadening. A pulse that fulfills these requirements, as illustrated in Figure 1.4, is called a soliton [33]. The balance of dispersive and nonlinear effects required to form a fundamental soliton is expressed by the dispersion, peak power P_0, pulse time T_0, and the nonlinear parameter γ [29]. The soliton peak power, P_0, can be given as

$$P_0 = \frac{1}{|\gamma|T_0{}^2}\left|\frac{\partial^2\beta}{\partial\omega^2}\right| = \frac{|D(\lambda)|\lambda^2}{2\pi c|\gamma|T_0^2},\tag{1.30}$$

Where γ is a figure of merit for the nonlinearity of the waveguide or fiber, taking into account its mode confinement, and is given by

$$\gamma = \frac{n_2\omega}{A_{\text{eff}}c}\tag{1.31}$$

Higher order solitons are also possible, but will not be discussed here.

Typical values of γ span across many orders of magnitude, from 1.3 W^{-1}km^{-1} for a SMF-28 fiber [57], to 1.01 W^{-1}m^{-1} in thick silicon nitride waveguides [58], to 10^4 W^{-1}m^{-1} in graphene-silicon hybrid waveguides [59].

Another nonlinear effect that can occur is four-wave mixing (FWM). Four-wave mixing is the process by which two photons are annihilated and two new photons are created, as illustrated in Figure 1.5. Figure 1.5 (a) shows degenerate FWM, where the two annihilated photons are of identical energy, whereas Figure 1.5 (b) shows non-degenerate FWM with photons of unequal energy. Because FWM is subject to conservation of energy without loss to the material, the energy splitting needs to be symmetric in both cases. The modes will be approximately equally spaced in a resonator with low integrated dispersion, as shown in Figure 1.5 (c). In this case FWM will fill all the cavity modes, creating a frequency comb. The dynamics of comb formation are highly complex, and involve both degenerate and non-degenerate FWM of modes that are not necessarily adjacent [60].
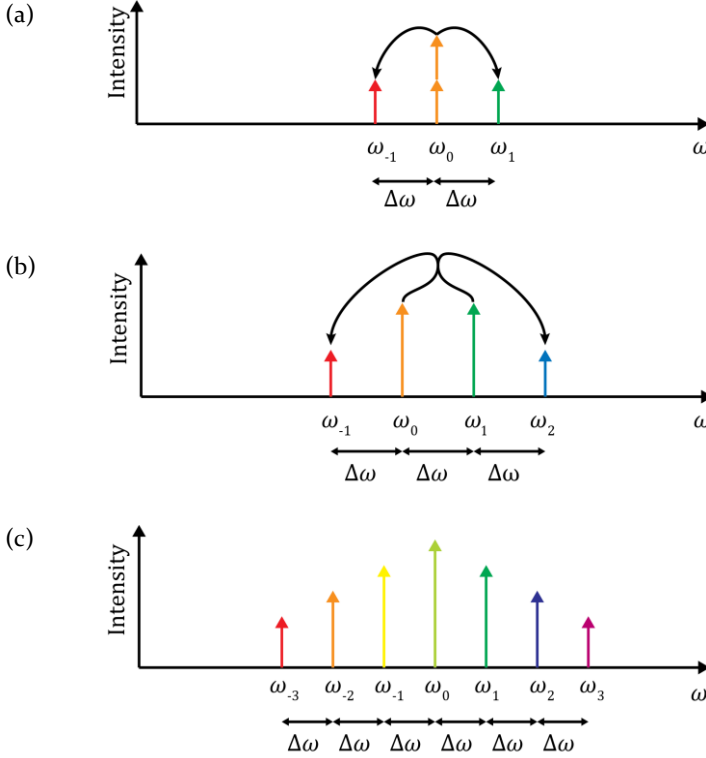
Figure 1.5: Schematic representation of four-wave mixing in the frequency domain, with frequencies $\omega_i = \omega_0 \pm i\Delta\omega$, $i=...$-2, -1, 0, 1, 2, ... Under certain phase matching conditions the processes may be reversed, amplifying the pump and decreasing the sidebands. (a) Degenerate FWM. Two photons of frequency ω_0 are annihilated, and photons of frequency ω_{-1} and ω_1 are created. (b) Non-degenerate FWM. Two photons of frequency ω_0 and ω_1 are annihilated, and photons of frequency ω_{-1} and ω_2 are created. (c) Cascaded FWM in a resonator. Starting with annihilation of ω_0, photons are generated at many cavity modes through a complex combination of degenerate and non-degenerate FWM.

There are many comb patterns that may be excited, including chaotic patterns, rolls, single solitons, soliton molecules and dark solitons [61]. FWM is a highly phase-sensitive process and the type of comb pattern, as well as the minimum threshold power to excite this comb pattern, is dependent on the dispersion of the cavity [36]. In general, anomalous dispersion is desirable as it reduces the necessary power and allows access to solitons and roll patterns. It can be shown that at critical coupling, the minimum power necessary to excite a comb is equal to [36]

$$P_{th} = \frac{\omega n_0^2 A_{\text{eff}} L}{4c n_2 Q^2} \qquad (1.32)$$

Although the minimum power factors depends on n_2, the effective mode area, and the cavity length, it is only linearly proportional to each of them. The Q factor, however, features quadratically in (1.32). Therefore, minimizing losses can be a more fruitful efficient path to low threshold powers than minimizing the resonator size or targeting high n_2 materials [61]. For example, frequency combs with threshold powers of 2 mW have been demonstrated in mm-sized MgF_2 microtoroids with Q factors above 10^9 [62], despite a low n_2 of 7.4×10^{-21} W/m² [63]. Such high Q factors are challenging to achieve in microring resonators. However, waveguides offer a small enough mode volume and resonator size to be practical, with pump powers down to 10 mW [64]. Furthermore, the compact, robust packaging available stands in stark contrast to non-integrated resonators, which typically require tapered fibers or prisms for coupling.

Soliton combs are highly desirable due to their stability and excellent phase coherence, with numerous applications [65]. These include LIDAR [66], calibrating astrophysical spectrometers [67], optical clocks [68], dual comb spectroscopy [69], and massively parallel coherent telecommunications [70]. Soliton excitation is notoriously difficult, however, due to a combination of thermal drift and SPM induced phase shift. The intensity builds up near resonance, which causes heating over a timescale of milliseconds, and a shifting of the resonance due to thermo-optic effects. Simultaneously, SPM causes an instantaneous nonlinear phase shift and a distorted resonance shape. Numerous schemes have been proposed to overcome these issues [71–74].

As n_2 is present in every material [49], many material platforms have been utilized for third order integrated nonlinear optics. These include silicon [41,75,76], silicon nitride [58,77–79], silicon oxynitride [80,81], titanium oxide [82], silicon carbide [83,84], and chalcogenide glasses [85–88]. Materials with higher refractive index [89] and lower bandgaps [90] generally show higher nonlinearities. However, due to the high optical intensities necessary, two-photon absorption is a limiting factor for the operating wavelength, which should be at least a factor 2 longer than the band gap. Silicon, which has a very high nonlinear refractive index, is therefore mostly used with pump wavelengths at 2.2 µm and above [65].

1.2 Potassium yttrium double tungstate (KY(WO$_4$)$_2$)

This section gives an overview of the fundamental properties of potassium yttrium double tungstate (KY(WO$_4$)$_2$) as well as the state of the art in this material.

1.2.1 Material properties

KY(WO$_4$)$_2$ is a monoclinic crystal belonging to the potassium double tungstate family. This family consists of materials with the general chemical formula KT(WO$_4$)$_2$, where T is a trivalent cation. Other prominent members of the family are KYb(WO$_4$)$_2$, KGd(WO$_4$)$_2$ and KLu(WO$_4$)$_2$. These materials have long been used as bulk laser materials [91–96], both based on rare earth ion doping and Raman gain. These crystals may also be alloyed, including several cations, which is useful for lattice matching of epitaxially grown heterolayers [97,98], as per Vegard's law [99,100]. An example of such a layer is KGd$_{0.53}$Yb$_{0.57}$(WO$_4$)$_2$ [98]. This particular example includes a high concentration of the optically active ytterbium ion, which is a common dopant for lasers and amplifiers.

KY(WO$_4$)$_2$ has two main phases, called the α and β phases. The β phase only exists above 1025°C [101]. The α phase belongs to the monoclinic, centrosymmetric $2/m$ point group, Schönflies notation C_{2h}^6, with space groups C2/c or I2/c [102]. The unit cell parameters are given in Table 1.2 [103]. The two space groups describe the same crystal in different coordinate systems, and the choice of either does not indicate a physical difference. The two different coordinate systems are illustrated in Figure 1.6.

Table 1.2: Unit cell parameters for the α phase of $KY(WO_4)_2$. The I2/c parameters are indicated with an asterisk. Parameters taken from [103].

	C2/c	I2/c
$a/a*$	1.064 nm	0.805 nm
$b/b*$	1.035 nm	1.035 nm
$c/c*$	0.754 nm	0.754 nm
$\beta/\beta*$	130.5°	94.0°
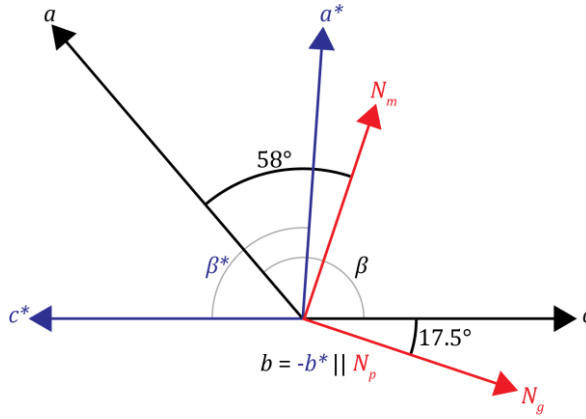
Figure 1.6: Crystallographic axis orientation of $KY(WO_4)_2$ in the C2/c (black) and I2/c (*, blue) space groups. The major semiaxes of the optical indicatrix (red) are also included.

Also included in Figure 1.6 are the major semiaxes of the optical indicatrix (principal axes), N_m, N_g, and N_g. As a monoclinic material, $KY(WO_4)_2$ is uniaxial, with only one optical axis for which the refractive index is independent of polarization. N_p is parallel with the crystallographic b axis [104], while N_g and N_m are at an angle with the a and c axes. By definition, all the semiaxes are perpendicular to each other [33]. The refractive indices of $KY(WO_4)_2$ have been reported in literature [97] using the single-term Sellmeier equation,

$$n^2 = A + (B\lambda^2)/(\lambda^2 - C) \qquad (1.33)$$

The Sellmeier coefficients along N_g, N_m and N_p are given in Table 1.3, and the refractive indices are plotted in Figure 1.7.

Table 1.3: Sellmeier coefficients and of KY(WO$_4$)$_2$ [97] as well as refractive indices at 632 nm and 1550 nm.

	A	B	C [μm^2]	n, 632 nm	n, 1550 nm
N_g	1	3.11897	0.02761	2.086	2.039
N_m	1	2.95349	0.02628	2.040	1.997
N_p	1	2.80731	0.02485	1.999	1.959
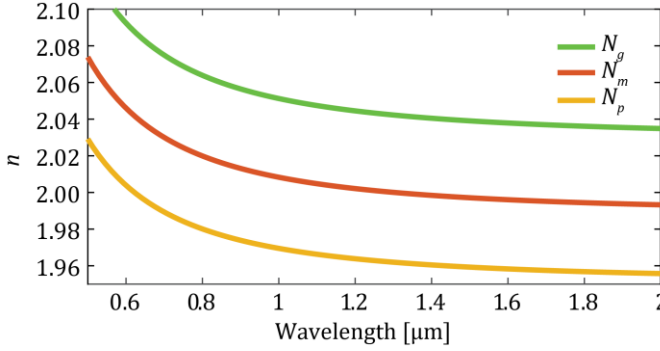
Figure 1.7: Refractive indices of KY(WO$_4$)$_2$ at the semiaxes of the indicatrix [97].

Because the rare-earth ions are substitutionally doped into the Y position of the unit cell, the interionic distance is high. This reduces the amount of interionic quenching, which permits high doping concentrations [98,105]. Furthermore, rare earth ions in KY(WO$_4$)$_2$ have high emission and absorption cross-sections [98,106]. The combination of high absorption and emission cross-sections, with high rare-earth ion concentration and the high intensity achieved in channel waveguide configuration permit achieving very high optical gain, such as amplifiers with net gain of 1000 dB/cm at 981 nm, and 13 dB/cm at 1535 nm [105,107].

The non-linear refractive index, n_2, is relatively high at 2.4×10^{-19} m^{2}W^{-1} at a wavelength of 819 nm [108]. Furthermore, KY(WO$_4$)$_2$ has a high Raman gain value with sharp peaks at 765 cm^{-1} and 905 cm^{-1} [109].

1.2.2 State of the art

KY(WO$_4$)$_2$ and other tungstates have long seen widespread use as a laser material [91–96]. This includes high power lasers [93,110], as well as ultrafast [91,93,94,111–114] and Raman [95,96,115] lasers enabled by the high optical gain that can be achieved in this host material when doping it with rare-earth ions and its high nonlinearity and Raman gain. In epitaxially grown low index

contrast waveguides, results include high gain waveguide amplifiers [105,107] and lasers [97,110,116–121]. There has also been interest in waveguides defined by femtosecond pulse irradiation [122–124], and both lasing [125] and Raman gain [126,127] have been demonstrated.

All of the above examples are realized in low index contrast structures with a relatively large effective area, A_{eff}. Higher index contrast waveguides can have higher confinement, which reduces the pump thresholds and enables bent structures like ring resonators. They can also be dispersion engineered for use in nonlinear optics, which is not achievable in low index contrast structures.

Some work has been done on realizing such high index contrast waveguides in $KY(WO_4)_2$, using two different approaches. One consists of lapping and polishing thin layers bonded on low index substrates like glasses or polymers. Work on this approach has included the development of thin layers [128–130] and the structuring of waveguides by etching or ion milling [131–133] or by optical dicing [134]. This method offers very high index contrasts of up to 0.6 depending on wavelength and substrate, and low losses due to the high optical quality substrates available. However, it is labor intensive and has low yield.

The other approach consists of swift heavy ion irradiation [135,136]. In this method, a $KY(WO_4)_2$ crystal is bombarded with carbon ions. This creates an amorphized region of depressed refractive index at a distance below the surface, the center of which corresponds with the center of the electronic damage region. The depth and thickness of the layer can be selected by the irradiation voltage and fluence. The depressed index region, called the barrier, serves as the low index substrate, and this eliminates the need for polishing. For this reason, irradiation is a low labor cost, high yield method. However, the index contrast is lower than the bonding method, at approximately 0.2, and the intrinsic losses are higher.

Considering the fact that the n_2 of $KY(WO_4)_2$ is lower than that of Si_3N_4 and the currently achieved losses are higher [131,135], $KY(WO_4)_2$ is not a promising material for nonlinear optics. However, its performance as a rare earth doped amplifier, laser and Raman laser material is excellent. Advances in fabrication techniques may improve such devices further, with lower thresholds and higher gain achieved by using ring resonators.

Chapters 2 and 3 introduce reactive ion etching techniques that are applicable to both the bonding method and the irradiation method and permit etching

depths of 6.5 µm to be achieved. In chapter 4, the irradiation method is developed further by introducing a wet etching technique that allows complete removal of the barrier. This allows the index contrast to be enhanced greatly and allows suspended structures.

1.3 Aluminum oxide (Al_2O_3)

This section gives an overview of the aluminum oxide (Al_2O_3) technology. Although Al_2O_3 is most known for its crystalline form sapphire, this work only considers amorphous or polycrystalline Al_2O_3 [137].

1.3.1 Material properties

Al_2O_3 is a dielectric material with a wide transparency window, ranging from 150 nm to 5 µm [138]. In its completely amorphized form, which is most commonly used in integrated optics due to its low propagation loss [139], it has a refractive index of approximately 1.67 at 633 nm [140]. However, the exact refractive index and material dispersion is heavily dependent on the growth conditions. Al_2O_3 may be grown by for example atomic layer deposition (ALD) [141], pulsed laser deposition (PLD) [142] or sputtering either of Al_2O_3 targets [143] with argon or of metallic aluminum targets with a mixture of argon and oxygen, called reactive sputtering [139,140]. Although good layers have been produced, PLD and especially ALD suffer from low growth rates [144,145]. In this work, only RF magnetron sputtering using oxygen and argon on a metallic target is considered.

The refractive index of the grown layer depends first and foremost on the structure of the deposited layer, which depends on the oxidation of the target [140]. At high degrees of oxidation, the refractive index may approximate that of sapphire, which indicates a high degree of poly-crystallinity. Such layers typically show high losses, indicating large grains.

The nonlinear index, n_2, of Al_2O_3 is predicted to be 4.77×10^{-20} m^2W^{-1} at a wavelength of 958 nm [146] based on extrapolations of BGO model [89] predictions of n_2 in aluminosilicate fibers with varying stoichiometries. The BGO model predicts n_2 based on the linear refractive index and dispersion of a material, and has a typical accuracy of ±20% [89]. This value of n_2 is somewhat higher than that of crystalline sapphire, which has been directly measured by z-scan techniques to approximately 3×10^{-20} m^2W^{-1} at the same wavelength [147].

1.3.2 State of the art

Al_2O_3 has been used throughout a wide wavelength range, with demonstrated devices at 371 nm [148], 1020 nm [149], 1532 nm [150], and 2 µm [151]. Losses in sputtered layers down to 0.12 dB/cm at 1550 nm have been reported [152], with losses down to 0.21 dB/cm after shallow etching in a wide waveguide [153]. In fully etched waveguides, losses are higher, typically around 0.6 dB/cm [15].

Al_2O_3 is commonly doped with rare earth ions, and permits high doping concentrations[150]. For this reason, Al_2O_3 has primarily been of interest as a gain medium, with several amplifiers [150,154] and lasers [40,155–157] having been demonstrated. Four-wave mixing has been shown in a high-Q Si_3N_4-Al_2O_3 hybrid microcavity [158], although nonlinear effects have yet to be fully explored. Passive devices have also been explored for biosensing, with high-Q microring resonators showing high sensitivities for detecting cancer biomarkers [15].

Monolithic integration of Al_2O_3 with other materials has been recently demonstrated, through several promising approaches. These include integration with SOI [159] and Si_3N_4 [154,160–163], as well as integration of undoped and doped Al_2O_3 [164] by a photonic damascene process. So far, all these processes have used either Al_2O_3 layers as a cladding or as thin waveguides. Thick waveguides, possibly dispersion engineered, can add more functionality to this emerging material system. For example, the high coupling efficiency of the TriPleX platform [165] efficiently coupled [162] with a high power [163] tunable [166] laser and an undoped [164] ring with anomalous dispersion may provide a compact frequency comb system, only requiring an external diode pump laser. All the required components exist, as well as the integration technology, and such a device may plausibly be developed in the future.

1.4 Silicon Nitride (Si_3N_4)

This section gives an overview of Si_3N_4 technology. Si_3N_4 is an extremely versatile [167,168] material enjoying mainstream popularity in integrated optics, and a complete overview could fill volumes. Therefore, this section will be restricted to its use in integrated nonlinear optics.

1.4.1 Material properties

Like Al_2O_3, Si_3N_4 is a dielectric glass with a relatively wide transparency window, ranging from around 350 nm [169] up to around 5 µm [170]. In practice, Si_3N_4 on SiO_2 waveguides are guiding between 400 nm and 2.3 µm [168]. Longer wavelengths are difficult to reach due to the small waveguide cores commonly used, and due to absorption above 3700 nm in the SiO_2 cladding.

The optical properties of Si_3N_4 are highly sensitive to the method of deposition [170]. Typical layers are deposited via low pressure chemical vapor deposition (LPCVD) [171]. Depending on the relative gas flows, the resulting chemical composition will be on the form Si_xN_y, where $x/y > 0.75$ indicates a silicon-rich nitride (SiRN). Silicon rich nitrides have higher refractive index, nonlinear index n_2 [172], bandgap, and optical losses, and lower layer stress [172] relative to stoichiometric (Si_3N_4) silicon nitride.

Stoichiometric Si_3N_4 has a relatively high refractive index at around 1.98 at 1550 nm, and an n_2 of 2.4×10^{-19} m^2W^{-1} at 1550 nm [173]. This is higher than that of $KY(WO_4)_2$ as it is measured at a longer wavelength.

1.4.2 State of the art

Si_3N_4 is of great interest in nonlinear optics [80] due to its high n_2, low Raman background [174,175], and low propagation losses [167]. In low-confinement Si_3N_4 waveguides, losses as low as 0.001 dB/cm [176] have been reported. These waveguides are however only suitable for linear optics with low integration density and without anomalous dispersion. This is because of their low confinement, due to a thickness of only 80 nm. Achieving anomalous dispersion, however, requires thicknesses above 700 nm [177,178].

LPCVD deposited Si_3N_4 on SiO_2 is a highly stressed material [179], and the layer thickness is effectively limited to 250 nm-400 nm, above which the layers crack. Because thicker layers are necessary to achieve anomalous dispersion [178], many creative techniques have been devised to overcome this limit. The simplest stress-reduction technique consists of using two depositions separated by annealing steps [180]. Stable layers of up to 744 nm thickness have been fabricated using this approach. This has resulted in losses of 0.12 dB/cm in single mode ring resonators, and the generation of octave-spanning frequency combs [77], including a miniaturized battery-powered comb integrated with a III-V chip [181]. This method is still prone to cracking,

although 910 nm thick layers have been achieved by manually pre-structuring the wafer with stress-relieving trenches using a diamond stylus [182].

The photonic damascene process represents a different approach to fabricate thick Si_3N_4 waveguides with the correct aspect ratio to achieve anomalous dispersion [177,183]. Here, the waveguides are defined by etching trenches in the SiO_2 substrate before deposition. The waveguides are then produced by deposition into the trench. Generally, multiple deposition steps are required, with the wafers cooled to room temperature between steps to avoid cracking. The resulting waveguides have thicknesses up to 1.35 µm [177] and losses down to 0.4 dB/cm [183] at 1550 nm. Two-octave spanning supercontinua have been generated using such waveguides [58]. Single soliton frequency combs using pump powers of 455 mW have also been shown [184]. The aspect ratio is limited, however, as keyhole defects [171] may occur and cause losses [183].

Losses of the channel waveguides fabricated by the damascene process can be further reduced by performing a roughness reducing preform reflow of the etched SiO_2. The preform reflow process consists of an 18 hour annealing step slightly above the glass transition temperature of SiO_2, prior to Si_3N_4 LPCVD deposition [185]. Total propagation losses as low as 0.05 dB/cm have been experimentally demonstrated [185]. This tremendous reduction in losses has enabled single-soliton frequency combs with pump powers below 10 mW [64] as well as electrically pumped integrated microcomb systems [186].

Other approaches to thick layers include low temperature liquid source CVD with TEOS as a precursor and a temperature of 150°C, which has given a thickness of 900 nm [187] and losses of 2.9 dB/cm, or PECVD in pulsed LF/HF mode giving 500 nm [188] and losses of 4 dB/cm. The high losses induced by these methods make them non ideal for nonlinear integrated photonics.

While several the techniques mentioned above have proven results over many years, they all include extra processing steps and carry risks of cracking. A process using a single deposition step with low stress without compromising film quality could simplify fabrication drastically.

1.5 Outline of this thesis

The materials discussed above are all capable of offering a wide range of functionalities. However, their full potential has still not been reached due to underdeveloped fabrication technologies. One common aspect of all three is

that high index contrast waveguides with cross-sections around 1 μm × 1 μm are either challenging to make or not available at all.

The benefits of such high index contrast waveguides include the potential for dispersion engineering to create nonlinear optical devices, potentially lower losses due to low sidewall interaction, and lower lasing thresholds due to high confinement and small modes. Compared with the state of the art, the waveguides targeted in this thesis are very small in $KY(WO_4)_2$, but very large in Al_2O_3 and Si_3N_4. Nevertheless, the unifying topic of this thesis is the push towards the realization of these waveguides, overcoming the very different fabrication challenges each of them face.

This thesis presents developments in the fabrication technology for $KY(WO_4)_2$, Al_2O_3, and Si_3N_4 on sapphire, a novel material system with record-low layer stresses. Chapters 2-4 discuss $KY(WO_4)_2$, chapter 5 discusses Al_2O_3 and chapter 6 discusses Si_3N_4.

Chapter 2 shows the development of a dry etching process for $KY(WO_4)_2$. Photoresist, SiO_2 and amorphous carbon are considered for use as masks, and their relative merits are discussed. Carbon is shown to give a selectivity up to 10 during Ar sputter etching, but with the tradeoff of challenging fabrication.

Chapter 3 presents a complete fabrication flow for surface structuring $KY(WO_4)_2$, aimed towards deep etched structures. Key results include a device for reducing edge bead after resist spin coating, a hard mask process for etching several micrometers deep and a wet etch technique for removing redeposition. The results are published in Micromachines, "Redeposition-Free Deep Etching in Small $KY(WO_4)_2$ Samples" [189].

Chapter 4 demonstrates a technique for creating pedestal disks in $KY(WO_4)_2$. The technique is based on a selective wet etch that removes an amorphized subsurface layer of swift heavy ion irradiated $KY(WO_4)_2$. The results are published in Optical Materials Express, "Pedestal disk resonators in potassium yttrium double tungstate" [190].

Chapter 5 presents racetrack resonators in a thick high-index Al_2O_3 material, designed for anomalous dispersion near 1550 nm.

Chapter 6 presents 1400 nm thick Si_3N_4 layers on sapphire substrates. The layer stresses are reduced by 90% relative to those in layers grown directly on silicon. Losses are measured using racetrack resonators. The implemented

waveguides show simulated anomalous dispersion over a wide frequency range.

Bibliography

1. S. E. Miller, "Integrated Optics: An Introduction," Bell Syst. Tech. J. **48**(7), 2059–2069 (1969).
2. E. A. J. Marcatili, "Dielectric rectangular waveguide and directional coupler for integrated optics," Bell Syst. Tech. J. **48**(7), 2071–2102 (1969).
3. E. A. J. Marcatili, "Bends in Optical Dielectric Guides," Bell Syst. Tech. J. **48**(7), 2103–2132 (1969).
4. J. E. Goell, "A circular-harmonic computer analysis of rectangular dielectric waveguides," Bell Syst. Tech. J. **48**(7), 2133–2160 (1969).
5. R. Shubert and J. H. Harris, "Optical Surface Waves on Thin Films and Their Application to Integrated Data Processors," IEEE Trans. Microw. Theory Techn. **16**(12), 1048–1054 (1968).
6. A. Karbowiak, "Optical waveguides," in *Advances in Microwaves: Volume 1* (Academic Press, 1966), p. 75.
7. D. Thomson, A. Zilkie, J. E. Bowers, T. Komljenovic, G. T. Reed, L. Vivien, D. Marris-Morini, E. Cassan, L. Virot, J.-M. Fédéli, J.-M. Hartmann, J. H. Schmid, D.-X. Xu, F. Boeuf, P. O'Brien, G. Z. Mashanovich, and M. Nedeljkovic, "Roadmap on silicon photonics," J. Opt. **18**(7), 073003 (2016).
8. Y. Fan, R. M. Oldenbeuving, C. G. Roeloffzen, M. Hoekman, D. Geskus, R. G. Heideman, and K.-J. Boller, "290 Hz Intrinsic Linewidth from an Integrated Optical Chip-based Widely Tunable InP-Si_3N_4 Hybrid Laser," in *Conference on Lasers and Electro-Optics* (Optical Society of America, 2017), p. JTh5C.9.
9. A. J. Ward, D. J. Robbins, G. Busico, E. Barton, L. Ponnampalam, J. P. Duck, N. D. Whitbread, P. J. Williams, D. C. J. Reid, A. C. Carter, and M. J. Wale, "Widely tunable DS-DBR laser with monolithically integrated SOA: design and performance," IEEE J. Sel. Top. Quantum Electron. **11**(1), 149–156 (2005).
10. X. Zheng, D. Patil, J. Lexau, F. Liu, G. Li, H. Thacker, Y. Luo, I. Shubin, J. Li, J. Yao, P. Dong, D. Feng, M. Asghari, T. Pinguet, A. Mekis, P. Amberg, M. Dayringer, J. Gainsley, H. F. Moghadam, E. Alon, K. Raj, R. Ho, J. E. Cunningham, and A. V. Krishnamoorthy, "Ultra-efficient 10Gb/s hybrid integrated silicon photonic transmitter and receiver," Opt. Express **19**(6), 5172–5186 (2011).
11. M. K. Smit and C. V. Dam, "PHASAR-based WDM-devices: Principles, design and applications," IEEE J. Sel. Top. Quantum Electron. **2**(2), 236–250 (1996).

12. X. Qu, J. Brame, Q. Li, and P. J. J. Alvarez, "Nanotechnology for a Safe and Sustainable Water Supply: Enabling Integrated Water Treatment and Reuse," Acc. Chem. Res. **46**(3), 834–843 (2013).

13. M. J. R. Heck, "Highly integrated optical phased arrays: photonic integrated circuits for optical beam shaping and beam steering," Nanophotonics **6**(1), 93–107 (2017).

14. C. V. Poulton, A. Yaacobi, D. B. Cole, M. J. Byrd, M. Raval, D. Vermeulen, and M. R. Watts, "Coherent solid-state LIDAR with silicon photonic optical phased arrays," Opt. Lett. **42**(20), 4091–4094 (2017).

15. M. de Goede, M. Dijkstra, R. Obregón, J. Ramón-Azcón, E. Martínez, L. Padilla, F. Mitjans, and S. M. Garcia-Blanco, "Al_2O_3 microring resonators for the detection of a cancer biomarker in undiluted urine," Opt. Express **27**(13), 18508–18521 (2019).

16. C. Ciminelli, D. D'Agostino, G. Carnicella, F. Dell'Olio, D. Conteduca, H. P. M. M. Ambrosius, M. K. Smit, and M. N. Armenise, "A High-Q InP Resonant Angular Velocity Sensor for a Monolithically Integrated Optical Gyroscope," IEEE Photon. J. **8**(1), 1–19 (2016).

17. V. Y. Venediktov, Y. V. Filatov, and E. V. Shalymov, "Passive ring resonator micro-optical gyroscopes," Quantum Electron. **46**(5), 437 (2016).

18. C. Minkenberg, N. Farrington, A. Zilkie, D. Nelson, C. P. Lai, D. Brunina, J. Byrd, B. Chowdhuri, N. Kucharewski, K. Muth, A. Nagra, G. Rodriguez, D. Rubi, T. Schrans, P. Srinivasan, Y. Wang, C. Yeh, and A. Rickman, "Reimagining Datacenter Topologies With Integrated Silicon Photonics," J. Opt. Commun. Netw. **10**(7), B126–B139 (2018).

19. N. Li, M. Xin, Z. Su, E. S. Magden, N. Singh, J. Notaros, E. Timurdogan, P. Purnawirman, J. D. B. Bradley, and M. R. Watts, "A Silicon Photonic Data Link with a Monolithic Erbium-Doped Laser," Sci. Rep. **10**(1), 1114 (2020).

20. M. Kues, C. Reimer, P. Roztocki, L. R. Cortés, S. Sciara, B. Wetzel, Y. Zhang, A. Cino, S. T. Chu, B. E. Little, D. J. Moss, L. Caspani, J. Azaña, and R. Morandotti, "On-chip generation of high-dimensional entangled quantum states and their coherent control," Nature **546**(7660), 622–626 (2017).

21. C. Taballione, C. Taballione, T. A. W. Wolterink, J. Lugani, A. Eckstein, B. A. Bell, R. Grootjans, I. Visscher, D. Geskus, C. G. H. Roeloffzen, J. J. Renema, J. J. Renema, J. J. Renema, I. A. Walmsley, P. W. H. Pinkse, and K.-J. Boller, "8×8 reconfigurable quantum photonic processor based on silicon nitride waveguides," Opt. Express **27**(19), 26842–26857 (2019).

22. L. Zhuang, C. G. H. Roeloffzen, M. Hoekman, K.-J. Boller, and A. J. Lowery, "Programmable photonic signal processor chip for radiofrequency applications," Optica **2**(10), 854–859 (2015).

23. K. Yao, R. Unni, and Y. Zheng, "Intelligent nanophotonics: merging photonics and artificial intelligence at the nanoscale," Nanophotonics **8**(3), 339–366 (2019).

24. T. W. Hughes, M. Minkov, Y. Shi, and S. Fan, "Training of photonic neural networks through in situ backpropagation and gradient measurement," Optica **5**(7), 864–871 (2018).

25. M. Glick, "The role of integrated photonics in datacenter networks," in *Next-Generation Optical Networks for Data Centers and Short-Reach Links IV* (International Society for Optics and Photonics, 2017), **10131**, p. 1013104.

26. K. Schmidtke, "Hyperscale data center applications of optoelectronics," in *Metro and Data Center Optical Networks and Short-Reach Links II* (International Society for Optics and Photonics, 2019), **10946**, p. 1094602.

27. J. C. Maxwell, *A Dynamical Theory of the Electromagnetic Field* (Wipf and Stock Publishers, 1996).

28. Z. Zhu and T. G. Brown, "Full-vectorial finite-difference analysis of microstructured optical fibers," Opt. Express **10**(17), 853–864 (2002).

29. G. P. Agrawal, *Nonlinear Fiber Optics* (Academic Press, 2013).

30. R. W. Boyd, *Nonlinear Optics* (Academic Press, 2008).

31. P. Drude, "Zur Elektronentheorie der Metalle," Ann. Phys. (Berl.) **306**(3), 566–613 (1900).

32. W. Sellmeier, "Ueber die durch die Aetherschwingungen erregten Mitschwingungen der Körpertheilchen und deren Rückwirkung auf die ersteren, besonders zur Erklärung der Dispersion und ihrer Anomalien," Ann. Phys. (Berl.) **223**(11), 386–403 (1872).

33. B. E. A. Saleh and M. C. Teich, *Fundamentals of Photonics* (Wiley, 2007).

34. D. A. G. Bruggeman, "Berechnung verschiedener physikalischer Konstanten von heterogenen Substanzen. I. Dielektrizitätskonstanten und Leitfähigkeiten der Mischkörper aus isotropen Substanzen," Ann. Phys. (Berl.) **416**, 636–664 (1935).

35. E. D. Palik, *Handbook of Optical Constants of Solids* (Academic Press, 1998).

36. G. Lin, A. Coillet, and Y. K. Chembo, "Nonlinear photonics with high-Q whispering-gallery-mode resonators," Adv. Opt. Photonics, AOP **9**(4), 828–890 (2017).

37. D. G. Rabus, *Integrated Ring Resonators - The Compendium* (Springer, 2007).

38. D. Marpaung, B. Morrison, R. Pant, C. Roeloffzen, A. Leinse, M. Hoekman, R. Heideman, and B. J. Eggleton, "Si_3N_4 ring resonator-based microwave

photonic notch filter with an ultrahigh peak rejection," Opt. Express **21**(20), 23286–23294 (2013).

39. P. Dong, S. F. Preble, and M. Lipson, "All-optical compact silicon comb switch," Opt. Express **15**(15), 9600–9605 (2007).

40. J. D. B. Bradley and E. S. Hosseini, "Monolithic erbium- and ytterbium-doped microring lasers on silicon chips," Opt. Express **22**(10), 12226–12237 (2014).

41. A. C. Turner, M. A. Foster, A. L. Gaeta, and M. Lipson, "Ultra-low power parametric frequency conversion in a silicon microring resonator," Opt. Express **16**(7), 4881–4887 (2008).

42. A. L. Gaeta, M. Lipson, and T. J. Kippenberg, "Photonic-chip-based frequency combs," Nat. Photonics **13**(3), 158 (2019).

43. W. R. McKinnon, D.-X. Xu, C. Storey, E. Post, A. Densmore, A. Delâge, P. Waldron, J. H. Schmid, and S. Janz, "Extracting coupling and loss coefficients from a ring resonator," Opt. Express **17**(21), 18971–18982 (2009).

44. A. Leinse, "Polymeric microring resonator based on electro-optic modulator," PhD Thesis, University of Twente (2005).

45. P. Del'Haye, T. Herr, E. Gavartin, M. L. Gorodetsky, R. Holzwarth, and T. J. Kippenberg, "Octave Spanning Tunable Frequency Comb from a Microresonator," Phys. Rev. Lett. **107**(6), 063901 (2011).

46. V. Brasch, M. Geiselmann, T. Herr, G. Lihachev, M. H. P. Pfeiffer, M. L. Gorodetsky, and T. J. Kippenberg, "Photonic chip broadband frequency comb for coherent telecommunication," in *2015 International Conference on Photonics in Switching (PS)* (2015), pp. 169–171.

47. T. Herr, "Solitons and dynamics of frequency comb formation in optical microresonators," École Polytechnique Fédérale de Lausanne (2013).

48. S. S. Bulanov, T. Zh. Esirkepov, A. G. R. Thomas, J. K. Koga, and S. V. Bulanov, "Schwinger Limit Attainability with Extreme Power Lasers," Phys. Rev. Lett. **105**(22), 220407 (2010).

49. J. Singh, *Smart Electronic Materials: Fundamentals and Applications* (Cambridge University Press, 2005).

50. R. S. Weis and T. K. Gaylord, "Lithium niobate: Summary of physical properties and crystal structure," Appl. Phys. A **37**(4), 191–203 (1985).

51. R. E. Cohen, "Origin of ferroelectricity in perovskite oxides," Nature **358**(6382), 136–138 (1992).

52. T. A. Driscoll, H. J. Hoffman, R. E. Stone, and P. E. Perkins, "Efficient second-harmonic generation in KTP crystals," J. Opt. Soc. Am. B **3**(5), 683–686 (1986).

53. Y. R. Shen, "Optical Second Harmonic Generation at Interfaces," Annu. Rev. Phys. Chem. **40**(1), 327–350 (1989).

54. L. Alloatti, C. Kieninger, A. Froelich, M. Lauermann, T. Frenzel, K. Köhnle, W. Freude, J. Leuthold, M. Wegener, and C. Koos, "Second-order nonlinear optical metamaterials: ABC-type nanolaminates," Appl. Phys. Lett. **107**(12), 121903 (2015).

55. A. Hermans, C. Kieninger, K. Koskinen, A. Wickberg, E. Solano, J. Dendooven, M. Kauranen, S. Clemmen, M. Wegener, C. Koos, and R. Baets, "On the determination of $\chi^{(2)}$ in thin films: a comparison of one-beam second-harmonic generation measurement methodologies," Sci. Rep. **7**, 44581 (2017).

56. M. Cazzanelli, F. Bianco, E. Borga, G. Pucker, M. Ghulinyan, E. Degoli, E. Luppi, V. Véniard, S. Ossicini, D. Modotto, S. Wabnitz, R. Pierobon, and L. Pavesi, "Second-harmonic generation in silicon waveguides strained by silicon nitride," Nat. Mater. **11**(2), 148–154 (2012).

57. A. Chabchoub, B. Kibler, C. Finot, G. Millot, M. Onorato, J. M. Dudley, and A. V. Babanin, "The nonlinear Schrödinger equation and the propagation of weakly nonlinear waves in optical fibers and on the water surface," Ann. Phys. (N. Y.) **361**, 490–500 (2015).

58. M. A. G. Porcel, F. Schepers, J. P. Epping, T. Hellwig, M. Hoekman, R. G. Heideman, P. J. M. van der Slot, C. J. Lee, R. Schmidt, R. Bratschitsch, C. Fallnich, and K.-J. Boller, "Two-octave spanning supercontinuum generation in stoichiometric silicon nitride waveguides pumped at telecom wavelengths," Opt. Express **25**(2), 1542–1554 (2017).

59. C. Donnelly and D. T. H. Tan, "Ultra-large nonlinear parameter in graphene-silicon waveguide structures," Opt. Express **22**(19), 22820–22830 (2014).

60. T. Herr, K. Hartinger, J. Riemensberger, C. Y. Wang, E. Gavartin, R. Holzwarth, M. L. Gorodetsky, and T. J. Kippenberg, "Universal formation dynamics and noise of Kerr-frequency combs in microresonators," Nat. Photonics **6**(7), 480–487 (2012).

61. Y. K. Chembo, "Kerr optical frequency combs: theory, applications and perspectives," Nanophotonics **5**(2), 214–230 (2016).

62. W. Liang, A. A. Savchenkov, A. B. Matsko, V. S. Ilchenko, D. Seidel, and L. Maleki, "Generation of near-infrared frequency combs from a MgF_2 whispering gallery mode resonator," Opt. Lett. **36**(12), 2290–2292 (2011).

63. R. Adair, L. L. Chase, and S. A. Payne, "Nonlinear refractive index of optical crystals," Phys. Rev. B **39**(5), 3337–3350 (1989).

64. J. Liu, A. S. Raja, M. Karpov, B. Ghadiani, M. H. P. Pfeiffer, B. Du, N. J. Engelsen, H. Guo, M. Zervas, and T. J. Kippenberg, "Ultralow-power chip-based soliton microcombs for photonic integration," Optica **5**(10), 1347–1353 (2018).

65. T. J. Kippenberg, A. L. Gaeta, M. Lipson, and M. L. Gorodetsky, "Dissipative Kerr solitons in optical microresonators," Science **361**(6402), (2018).

66. P. Trocha, M. Karpov, D. Ganin, M. H. P. Pfeiffer, A. Kordts, S. Wolf, J. Krockenberger, P. Marin-Palomo, C. Weimann, S. Randel, W. Freude, T. J. Kippenberg, and C. Koos, "Ultrafast optical ranging using microresonator soliton frequency combs," Science **359**(6378), 887–891 (2018).

67. M.-G. Suh, X. Yi, Y.-H. Lai, S. Leifer, I. S. Grudinin, G. Vasisht, E. C. Martin, M. P. Fitzgerald, G. Doppmann, J. Wang, D. Mawet, S. B. Papp, S. A. Diddams, C. Beichman, and K. Vahala, "Searching for exoplanets using a microresonator astrocomb," Nat. Photonics **13**(1), 25–30 (2019).

68. S. B. Papp, K. Beha, P. Del'Haye, F. Quinlan, H. Lee, K. J. Vahala, and S. A. Diddams, "Microresonator frequency comb optical clock," Optica **1**(1), 10–14 (2014).

69. I. Coddington, N. Newbury, and W. Swann, "Dual-comb spectroscopy," Optica **3**(4), 414 (2016).

70. P. Marin-Palomo, J. N. Kemal, M. Karpov, A. Kordts, J. Pfeifle, M. H. P. Pfeiffer, P. Trocha, S. Wolf, V. Brasch, M. H. Anderson, R. Rosenberger, K. Vijayan, W. Freude, T. J. Kippenberg, and C. Koos, "Microresonator-based solitons for massively parallel coherent optical communications," Nature **546**(7657), 274–279 (2017).

71. S. Zhang, J. M. Silver, L. D. Bino, F. Copie, M. T. M. Woodley, G. N. Ghalanos, A. Ø. Svela, N. Moroney, and P. Del'Haye, "Sub-milliwatt-level microresonator solitons with extended access range using an auxiliary laser," Optica **6**(2), 206–212 (2019).

72. H. Taheri, A. A. Eftekhar, K. Wiesenfeld, and A. Adibi, "Soliton Formation in Whispering-Gallery-Mode Resonators via Input Phase Modulation," IEEE Photon. J. **7**(2), 1–9 (2015).

73. T. Herr, V. Brasch, J. D. Jost, I. Mirgorodskiy, G. Lihachev, M. L. Gorodetsky, and T. J. Kippenberg, "Mode Spectrum and Temporal Soliton Formation in Optical Microresonators," Phys. Rev. Lett. **113**(12), 123901 (2014).

74. S. B. Papp, P. Del'Haye, and S. A. Diddams, "Parametric seeding of a microresonator optical frequency comb," Opt. Express **21**(15), 17615–17624 (2013).

75. M. A. Foster, A. C. Turner, J. E. Sharping, B. S. Schmidt, M. Lipson, and A. L. Gaeta, "Broad-band optical parametric gain on a silicon photonic chip," Nature **441**(7096), 960–963 (2006).

76. Y. Okawachi, M. Yu, V. Venkataraman, P. M. Latawiec, A. G. Griffith, M. Lipson, M. Lončar, and A. L. Gaeta, "Competition between Raman and

Kerr effects in microresonator comb generation," Opt. Lett. **42**(14), 2786–2789 (2017).

77. Y. Okawachi, K. Saha, J. S. Levy, Y. H. Wen, M. Lipson, and A. L. Gaeta, "Octave-spanning frequency comb generation in a silicon nitride chip," Opt. Lett. **36**(17), 3398–3400 (2011).

78. H. Zhao, B. Kuyken, S. Clemmen, F. Leo, A. Subramanian, A. Dhakal, P. Helin, S. Severi, E. Brainis, G. Roelkens, and R. Baets, "Visible-to-near-infrared octave spanning supercontinuum generation in a silicon nitride waveguide," Opt. Lett. **40**(10), 2177–2180 (2015).

79. R. Halir, Y. Okawachi, J. S. Levy, M. A. Foster, M. Lipson, and A. L. Gaeta, "Ultrabroadband supercontinuum generation in a CMOS-compatible platform," Opt. Lett. **37**(10), 1685–1687 (2012).

80. D. J. Moss, R. Morandotti, A. L. Gaeta, and M. Lipson, "New CMOS-compatible platforms based on silicon nitride and Hydex for nonlinear optics," Nat. Photonics **7**(8), 597–607 (2013).

81. C. Reimer, M. Kues, P. Roztocki, B. Wetzel, F. Grazioso, B. E. Little, S. T. Chu, T. Johnston, Y. Bromberg, L. Caspani, D. J. Moss, and R. Morandotti, "Generation of multiphoton entangled quantum states by means of integrated frequency combs," Science **351**(6278), 1176–1180 (2016).

82. X. Guan, H. Hu, L. K. Oxenløwe, and L. H. Frandsen, "Compact titanium dioxide waveguides with high nonlinearity at telecommunication wavelengths," Opt. Express **26**(2), 1055–1063 (2018).

83. X. Lu, J. Y. Lee, S. Rogers, and Q. Lin, "Optical Kerr nonlinearity in a high-Q silicon carbide microresonator," Opt. Express **22**(25), 30826–30832 (2014).

84. P. Xing, D. Ma, K. J. A. Ooi, J. W. Choi, A. M. Agarwal, and D. Tan, "CMOS-Compatible PECVD Silicon Carbide Platform for Linear and Nonlinear Optics," ACS Photonics **6**(5), 1162–1167 (2019).

85. M. R. E. Lamont, B. Luther-Davies, D.-Y. Choi, S. Madden, and B. J. Eggleton, "Supercontinuum generation in dispersion engineered highly nonlinear (γ = 10/W/m) As_2S_3 chalcogenide planar waveguide," Opt. Express **16**(19), 14938–14944 (2008).

86. M. Pagani, K. Vu, D.-Y. Choi, S. J. Madden, B. J. Eggleton, and D. Marpaung, "Instantaneous microwave frequency measurement using four-wave mixing in a chalcogenide chip," Opt. Commun. **373**, 100–104 (2016).

87. K. Tan, D. Marpaung, R. Pant, F. Gao, E. Li, J. Wang, D.-Y. Choi, S. Madden, B. Luther-Davies, J. Sun, and B. J. Eggleton, "Photonic-chip-based all-optical ultra-wideband pulse generation via XPM and birefringence in a chalcogenide waveguide," Opt. Express **21**(2), 2003–2011 (2013).

88. Y. Wang, S. Dai, G. Li, D. Xu, C. You, X. Han, P. Zhang, X. Wang, and P. Xu, "1.4–7.2 µm broadband supercontinuum generation in an As-S chalcogenide tapered fiber pumped in the normal dispersion regime," Opt. Lett. **42**(17), 3458–3461 (2017).

89. N. Boling, A. Glass, and A. Owyoung, "Empirical relationships for predicting nonlinear refractive index changes in optical solids," IEEE J. Quantum Electron. **14**(8), 601–608 (1978).

90. M. Sheik-Bahae, D. J. Hagan, and E. W. Van Stryland, "Dispersion and band-gap scaling of the electronic Kerr effect in solids associated with two-photon absorption," Phys. Rev. Lett. **65**(1), 96–99 (1990).

91. A. A. Kovalyov, V. V. Preobrazhenskii, M. A. Putyato, O. P. Pchelyakov, N. N. Rubtsova, B. R. Semyagin, V. E. Kisel', S. V. Kuril'chik, and N. V. Kuleshov, "115 fs pulses from Yb^{3+}:$KY(WO_4)_2$ laser with low loss nanostructured saturable absorber," Laser Phys. Lett. **8**(6), 431–435 (2011).

92. A. A. Lagatsky, F. Fusari, S. Calvez, J. A. Gupta, V. E. Kisel, N. V. Kuleshov, C. T. A. Brown, M. D. Dawson, and W. Sibbett, "Passive mode locking of a Tm,Ho:$KY(WO_4)_2$ laser around 2 µm," Opt. Lett. **34**(17), 2587–2589 (2009).

93. F. Brunner, G. J. Spühler, J. A. Au, L. Krainer, F. Morier-Genoud, R. Paschotta, N. Lichtenstein, S. Weiss, C. Harder, A. A. Lagatsky, A. Abdolvand, N. V. Kuleshov, and U. Keller, "Diode-pumped femtosecond Yb:$KGd(WO_4)_2$ laser with 1.1-W average power," Opt. Lett. **25**(15), 1119–1121 (2000).

94. U. Griebner, S. Rivier, V. Petrov, M. Zorn, G. Erbert, M. Weyers, X. Mateos, M. Aguiló, J. Massons, and F. Díaz, "Passively mode-locked Yb:$KLu(WO_4)_2$ oscillators," Opt Express **13**(9), 3465–3470 (2005).

95. A. A. Kaminskii, P. V. Klevtsov, L. Li, and A. A. Pavlyuk, "Stimulated emission from $KY(WO_4)_2$: Nd^{3+} crystal laser," Phys Status Solidi A **5**(2), K79–K81 (1971).

96. V. Petrov, M. C. Pujol, X. Mateos, Ò. Silvestre, S. Rivier, M. Aguiló, R. M. Solé, J. Liu, U. Griebner, and F. Díaz, "Growth and properties of $KLu(WO_4)_2$, and novel ytterbium and thulium lasers based on this monoclinic crystalline host," Laser Photonics Rev. **1**(2), 179–212 (2007).

97. S. Aravazhi, D. Geskus, K. van Dalfsen, S. A. Vázquez-Córdova, C. Grivas, U. Griebner, S. M. Garcia-Blanco, and M. Pollnau, "Engineering lattice matching, doping level, and optical properties of $KY(WO_4)_2$:Gd, Lu, Yb layers for a cladding-side-pumped channel waveguide laser," Appl. Phys. B **111**(3), 433–446 (2013).

98. Y.-S. Yong, S. Aravazhi, S. A. Vázquez-Córdova, J. L. Herek, S. M. García-Blanco, and M. Pollnau, "Gain dynamics in a highly ytterbium-doped

potassium double tungstate epitaxial layer," J. Opt. Soc. Am. B **35**(9), 2176–2185 (2018).

99. L. Vegard, "Die Konstitution der Mischkristalle und die Raumfüllung der Atome," Z. Physik **5**(1), 17–26 (1921).

100. A. R. Denton and N. W. Ashcroft, "Vegard's law," Phys. Rev. A **43**(6), 3161–3164 (1991).

101. E. Gallucci, C. Goutaudier, G. Boulon, and M. T. Cohen-Adad, "Growth of $KY(WO_4)_2$ single crystal: investigation of the WO_3 rich region in the K_2O-Y_2O_3-WO_3 ternary system. 2 — The $KY(WO_4)_2$ crystallisation field," Eur. J. Solid State Inorg. Chem. **35**(6), 433–445 (1998).

102. S. V. Borisov and R. F. Klevtsova, "Crystal structure of $KY(WO_4)_2$," Sov. Phys. Crystallogr. **13**(3), (1968).

103. P. V. Klevtsov, L. P. Kozeeva, and R. F. Klevtsova, "Crystallographic study of potassium-yttrium tungstate and molybdate," Izv. Akad. Nauk SSSR, Neorgan. Mater. **4**, 1147 (1968).

104. X. Mateos, R. Solé, Jna. Gavaldà, M. Aguiló, J. Massons, and F. Díaz, "Crystal growth, optical and spectroscopic characterisation of monoclinic $KY(WO_4)_2$ co-doped with Er^{3+} and Yb^{3+}," Opt. Mater. **28**(4), 423–431 (2006).

105. D. Geskus, S. Aravazhi, S. M. Garcia-Blanco, and M. Pollnau, "Giant optical gain in a rare-earth-ion-doped microstructure," Adv. Opt. Mater. **24**(10), OP19-22 (2012).

106. Y.-S. Yong, S. Aravazhi, S. A. Vázquez-Córdova, J. J. Carvajal, F. Díaz, J. L. Herek, S. M. Garcia-Blanco, and M. Pollnau, "Direct confocal lifetime measurements on rare-earth-doped media exhibiting radiation trapping," Opt. Mater. Express **7**(2), 527–532 (2017).

107. S. A. Vázquez-Córdova, S. Aravazhi, C. Grivas, Y.-S. Yong, S. M. Garcia-Blanco, J. L. Herek, and M. Pollnau, "High optical gain in erbium-doped potassium double tungstate channel waveguide amplifiers," Opt. Express **26**(5), 6260–6266 (2018).

108. N. Thilmann, G. Strömqvist, M. C. Pujol, V. Pasiskevicius, V. Petrov, and F. Díaz, "Nonlinear refractive indices in Yb^{3+}-doped and undoped monoclinic double tungstates $KRE(WO_4)_2$ where RE=Gd, Y, Yb, Lu," Appl. Phys. B **96**(2–3), 385–392 (2009).

109. J. A. Piper and H. M. Pask, "Crystalline Raman Lasers," IEEE Journal of Selected Topics in Quantum Electronics **3**(13), 692–704 (2007).

110. K. van Dalfsen, S. Aravazhi, C. Grivas, S. M. Garcia-Blanco, and M. Pollnau, "Thulium channel waveguide laser with 1.6 W of output power and ~80% slope efficiency," Opt. Lett. **39**(15), 4380–4383 (2014).

111. E. Kifle, X. Mateos, J. R. V. de Aldana, A. Ródenas, P. Loiko, S. Y. Choi, F. Rotermund, U. Griebner, V. Petrov, M. Aguiló, and F. Díaz, "Femtosecond-laser-written Tm:KLu(WO$_4$)$_2$ waveguide lasers," Opt. Lett. **42**(6), 1169–1172 (2017).

112. P. Klopp, V. Petrov, U. Griebner, and G. Erbert, "Passively mode-locked Yb:KYW laser pumped by a tapered diode laser," Opt. Express **10**(2), 108–113 (2002).

113. A. A. Lagatsky, S. Calvez, J. A. Gupta, V. E. Kisel, N. V. Kuleshov, C. T. A. Brown, M. D. Dawson, and W. Sibbett, "Broadly tunable femtosecond mode-locking in a Tm:KYW laser near 2 µm," Opt. Express **19**(10), 9995–10000 (2011).

114. S. A. Meyer, J. A. Squier, and S. A. Diddams, "Diode-pumped Yb:KYW femtosecond laser frequency comb with stabilized carrier-envelope offset frequency," Eur. Phys. J. D **48**(1), 19–26 (2008).

115. Z. Cong, Z. Liu, Z. Qin, X. Zhang, H. Zhang, J. Li, H. Yu, and W. Wang, "LD-pumped actively Q-switched Nd:KLu(WO$_4$)$_2$ self-Raman laser at 1185 nm," Opt. Laser Technol. **73**, 50–53 (2015).

116. D. Geskus, S. Aravazhi, K. Wörhoff, and M. Pollnau, "High-power, broadly tunable, and low-quantum-defect KGd$_{1-x}$Lu$_x$(WO$_4$)$_2$:Yb^{3+} channel waveguide lasers," Opt. Express **18**(25), 26107–26112 (2010).

117. D. Geskus, S. Aravazhi, C. Grivas, K. Wörhoff, and M. Pollnau, "Microstructured KY(WO$_4$)$_2$:Gd^{3+}, Lu^{3+}, Yb^{3+} channel waveguide laser," Opt. Express **18**(9), 8853 (2010).

118. D. Geskus, S. Aravazhi, E. Bernhardi, C. Grivas, S. Harkema, K. Hametner, D. Günther, K. Wörhoff, and M. Pollnau, "Low-threshold, highly efficient Gd^{3+}, Lu^{3+} co-doped KY(WO$_4$)$_2$:Yb^{3+} planar waveguide lasers," Laser Physics Letters **6**(11), 800–805 (2009).

119. K. van Dalfsen, S. Aravazhi, D. Geskus, K. Wörhoff, and M. Pollnau, "Efficient KY$_{1-x-y}$Gd$_x$Lu$_y$(WO$_4$)$_2$:Tm^{3+} channel waveguide lasers," Opt. Express **19**(6), 5277–5282 (2011).

120. D. Geskus, E. H. Bernhardi, K. van Dalfsen, S. Aravazhi, and M. Pollnau, "Highly efficient Yb^{3+}-doped channel waveguide laser at 981 nm," Opt. Express **21**(11), 13773–13778 (2013).

121. K. van Dalfsen, S. Aravazhi, C. Grivas, S. M. García-Blanco, and M. Pollnau, "Thulium channel waveguide laser in a monoclinic double tungstate with 70% slope efficiency," Opt. Lett. **37**(5), 887–889 (2012).

122. C. N. Borca, V. Apostolopoulos, F. Gardillou, H. G. Limberger, M. Pollnau, and R.-P. Salathé, "Buried channel waveguides in Yb-doped KY(WO$_4$)$_2$ crystals fabricated by femtosecond laser irradiation," Applied Surface Science **253**(19), 8300–8303 (2007).

123. F. M. Bain, W. F. Silva, A. A. Lagatsky, R. R. Thomson, N. D. Psaila, A. K. Kar, W. Sibbett, D. Jaque, and C. T. A. Brown, "Microspectroscopy of ultrafast laser inscribed channel waveguides in Yb:tungstate crystals," Appl. Phys. Lett. **98**(14), 141108 (2011).

124. X. Liu, S. Qu, Y. Tan, C. Zhang, and F. Chen, "Buried channel waveguides in neodymium-doped $KGd(WO_4)_2$ fabricated by low-repetition-rate femtosecond laser writing," Appl. Phys. B **103**(1), 145–149 (2011).

125. F. M. Bain, A. A. Lagatsky, R. R. Thomson, N. D. Psaila, N. V. Kuleshov, A. K. Kar, W. Sibbett, and C. T. A. Brown, "Ultrafast laser inscribed $Yb:KGd(WO_4)_2$ and $Yb:KY(WO_4)_2$ channel waveguide lasers," Opt. Express **17**(25), 22417–22422 (2009).

126. X. Liu, S. Qu, Y. Tan, and F. Chen, "Preservation of fluorescence and Raman gain in the buried channel waveguides in neodymium-doped $KGd(WO_4)_2(Nd:KGW)$ by femtosecond laser writing," Appl. Opt. **50**(6), 930–934 (2011).

127. S. M. Eaton, C. A. Merchant, R. Iyer, A. J. Zilkie, A. S. Helmy, J. S. Aitchison, P. R. Herman, D. Kraemer, R. J. D. Miller, C. Hnatovsky, and R. S. Taylor, "Raman gain from waveguides inscribed in $KGd(WO_4)_2$ by high repetition rate femtosecond laser," Appl. Phys. Lett. **92**(8), 081105 (2008).

128. C. I. van Emmerik, R. Frentrop, M. Dijkstra, F. Segerink, R. Kooijman, M. Muneeb, G. Roelkens, E. Ghibaudo, J.-E. Broquin, and S. M. Garcia-Blanco, "Heterogeneous integration of $KY(WO_4)_2$-on-glass: a bonding study," OSA Continuum, OSAC **2**(6), 2065–2076 (2019).

129. C. I. van Emmerik, S. M. Martinussen, J. Mu, M. Dijkstra, R. Kooijman, and S. M. Garcia-Blanco, "A novel polishing stop for accurate integration of potassium yttrium double tungstate on a silicon dioxide platform," in Proc. SPIE (2018), **10535**.

130. C. I. van Emmerik, R. Kooijman, M. Dijkstra, and S. M. Garcia-Blanco, "Lapping and Polishing of Crystalline $KY(WO_4)_2$: Toward High Refractive Index Contrast Slab Waveguides," Micromachines **10**(10), 674 (2019).

131. M. A. Sefünç, F. B. Segerink, and S. M. Garcia-Blanco, "High index contrast passive potassium double tungstate waveguides," Opt. Mater. Express **8**(3), 629–638 (2018).

132. M. Sefünç, "New architectures for integrated optics: Low-loss tight bends and on-chip high index contrast potassium double tungstate waveguides," University of Twente (2016).

133. M. Medina Martinéz, "KREW/SiO_2 waveguide platform for optical sensing applications," Universitat Rovira i Virgili (2019).

134. M. Medina, C. E. Rüter, M. C. Pujol, D. Kip, J. Masons, A. Ródenas, M. Aguiló, and F. Díaz, "KLu(WO$_4$)$_2$/SiO$_2$ Tapered Waveguide Platform for Sensing Applications," Micromachines **10**(7), 454 (2019).

135. R. N. Frentrop, V. Tormo-Márquez, J. Olivares, and S. M. García-Blanco, "High-contrast slab waveguide fabrication in KY(WO$_4$)$_2$ by swift heavy ion irradiation," in Proc. SPIE (2018), **10535**.

136. R. Frentrop, R. Frentrop, I. Subbotin, F. Segerink, R. Keim, V. Tormo-Marquez, J. Olivares, J. Olivares, K. Shcherbachev, S. Yakunin, I. Makhotkin, S. M. Garcia-Blanco, and S. M. Garcia-Blanco, "In-depth structural analysis of swift heavy ion irradiation in KY(WO$_4$)$_2$ for the fabrication of planar optical waveguides," Opt. Mater. Express **9**(12), 4796–4810 (2019).

137. W. A. P. M. Hendriks, L. Chang, C. I. van Emmerik, J. Mu, M. de Goede, M. Dijkstra, and S. M. Garcia-Blanco, "Rare-earth ion doped Al$_2$O$_3$ for active integrated photonics," Adv. Phys. X **6**(1), 1833753 (2021).

138. E. R. Dobrovinskaya, L. A. Lytvynov, and V. Pishchik, *Sapphire: Material, Manufacturing, Applications* (Springer US, 2009).

139. K. Worhoff, F. Ay, and M. Pollnau, "Optimization of Low-Loss Al$_2$O$_3$ Waveguide Fabrication for Application in Active Integrated Optical Devices," ECS Trans. **3**(11), 17 (2006).

140. C. I. van Emmerik, W. A. P. M. Hendriks, M. M. Stok, M. de Goede, L. Chang, M. Dijkstra, F. Segerink, D. Post, E. G. Keim, M. J. Dikkers, and S. M. García-Blanco, "Relative oxidation state of the target as guideline for depositing optical quality RF reactive magnetron sputtered Al$_2$O$_3$ layers," Opt. Mater. Express **10**(6), 1451–1462 (2020).

141. M. M. Aslan, N. A. Webster, C. L. Byard, M. B. Pereira, C. M. Hayes, R. S. Wiederkehr, and S. B. Mendes, "Low-loss optical waveguides for the near ultra-violet and visible spectral regions with Al$_2$O$_3$ thin films from atomic layer deposition," Thin Solid Films **518**(17), 4935–4940 (2010).

142. A. Pillonnet, C. Garapon, C. Champeaux, C. Bovier, R. Brenier, H. Jaffrezic, and J. Mugnier, "Influence of oxygen pressure on structural and optical properties of Al$_2$O$_3$ optical waveguides prepared by pulsed laser deposition," Appl. Phys. A **69**(1), S735–S738 (1999).

143. R. S. Nowicki, "Properties of rf-sputtered Al$_2$O$_3$ films deposited by planar magnetron," J. Vac. Sci. Technol. **14**(1), 127–133 (1977).

144. M. Demirtaş, C. Odacı, N. K. Perkgöz, C. Sevik, and F. Ay, "Low Loss Atomic Layer Deposited Al$_2$O$_3$ Waveguides for Applications in On-Chip Optical Amplifiers," IEEE J. Sel. Top. Quantum Electron. **24**(4), 1–8 (2018).

145. A. Suárez-García, J. Gonzalo, and C. N. Afonso, "Low-loss Al$_2$O$_3$ waveguides produced by pulsed laser deposition at room temperature," Appl. Phys. A **77**(6), 779–783 (2003).

146. P. Dragic, M. Cavillon, and J. Ballato, "The linear and nonlinear refractive index of amorphous Al_2O_3 deduced from aluminosilicate optical fibers," International Journal of Applied Glass Science **9**(3), 421–427 (2018).

147. A. Major, F. Yoshino, I. Nikolakakos, J. S. Aitchison, and P. W. E. Smith, "Dispersion of the nonlinear refractive index in sapphire," Opt. Lett. **29**(6), 602–604 (2004).

148. G. N. West, W. Loh, D. Kharas, C. Sorace-Agaskar, K. K. Mehta, J. Sage, J. Chiaverini, and R. J. Ram, "Low-loss integrated photonics for the blue and ultraviolet regime," APL Photonics **4**(2), 026101 (2019).

149. E. H. Bernhardi, M. R. H. Khan, C. G. H. Roeloffzen, H. A. G. M. van Wolferen, K. Wörhoff, R. M. de Ridder, and M. Pollnau, "Photonic generation of stable microwave signals from a dual-wavelength $Al_2O_3{:}Yb^{3+}$ distributed-feedback waveguide laser," Opt. Lett. **37**(2), 181–183 (2012).

150. S. A. Vázquez-Córdova, M. Dijkstra, E. H. Bernhardi, F. Ay, K. Wörhoff, J. L. Herek, S. M. García-Blanco, and M. Pollnau, "Erbium-doped spiral amplifiers with 20 dB of net gain on silicon," Opt. Express **22**(21), 25993–26004 (2014).

151. N. Li, E. S. Magden, Z. Su, N. Singh, A. Ruocco, M. Xin, M. Byrd, P. T. Callahan, J. D. B. Bradley, C. Baiocco, D. Vermeulen, and M. R. Watts, "Broadband 2-µm emission on silicon chips: monolithically integrated Holmium lasers," Opt. Express **26**(3), 2220–2230 (2018).

152. K. Worhoff, J. D. B. Bradley, F. Ay, D. Geskus, T. P. Blauwendraat, and M. Pollnau, "Reliable Low-Cost Fabrication of Low-Loss $Al_2O_3{:}Er^{3+}$ Waveguides With 5.4-dB Optical Gain," IEEE J. Quantum Electron. **45**(5), 454–461 (2009).

153. J. D. B. Bradley, F. Ay, K. Wörhoff, and M. Pollnau, "Fabrication of low-loss channel waveguides in Al_2O_3 and Y_2O_3 layers by inductively coupled plasma reactive ion etching," Appl. Phys. B **89**(2), 311–318 (2007).

154. J. Mu, M. Dijkstra, J. Korterik, H. Offerhaus, and S. M. García-Blanco, "High-gain waveguide amplifiers in Si_3N_4 technology via double-layer monolithic integration," Photon. Res. **8**(10), 1634–1641 (2020).

155. J. D. Bradley, R. Stoffer, L. Agazzi, F. Ay, K. Wörhoff, and M. Pollnau, "Integrated $Al_2O_3{:}Er^{3+}$ ring lasers on silicon with wide wavelength selectivity," Opt. Lett. **35**(1), 73–75 (2010).

156. E. S. Hosseini, Purnawirman, J. D. B. Bradley, J. Sun, G. Leake, T. N. Adam, D. D. Coolbaugh, and M. R. Watts, "CMOS-compatible 75 mW erbium-doped distributed feedback laser," Opt. Lett. **39**(11), 3106–3109 (2014).

157. M. de Goede, L. Chang, J. Mu, M. Dijkstra, R. Obregón, E. Martínez, E. Martínez, E. Martínez, L. Padilla, F. Mitjans, and S. M. Garcia-Blanco,

"Al$_2$O$_3$:Yb^{3+} integrated microdisk laser label-free biosensor," Opt. Express **44**(24), 5937–5940 (2019).

158. H. C. Frankis, Z. Su, Z. Su, N. Li, N. Li, E. S. Magden, M. Ye, M. R. Watts, M. R. Watts, and J. D. B. Bradley, "Four-Wave Mixing in a High-Q Aluminum Oxide Microcavity on Silicon," in *Conference on Lasers and Electro-Optics (2018)* (Optical Society of America, 2018), p. STh3I.3.

159. L. Agazzi, J. D. B. Bradley, M. Dijkstra, F. Ay, G. Roelkens, R. Baets, K. Wörhoff, and M. Pollnau, "Monolithic integration of erbium-doped amplifiers with silicon-on-insulator waveguides," Opt. Express **18**(26), 27703–27711 (2010).

160. Z. Su, N. Li, H. C. Frankis, E. S. Magden, T. N. Adam, G. Leake, D. Coolbaugh, J. D. B. Bradley, and M. R. Watts, "High-Q-factor Al$_2$O$_3$ micro-trench cavities integrated with silicon nitride waveguides on silicon," Opt. Express **26**(9), 11161–11170 (2018).

161. J. Mu, M. Dijkstra, Y.-S. Yong, M. de Goede, L. Chang, and S. M. García-Blanco, "Monolithic Integration of Al$_2$O$_3$ and Si$_3$N$_4$ Toward Double-Layer Active–Passive Platform," IEEE J. Sel. Top. Quantum Electron. **25**(5), 1–11 (2019).

162. J. Mu, M. Dijkstra, and S. M. García-Blanco, "Resonant Coupling for Active–Passive Monolithic Integration of Al$_2$O$_3$ and Si$_3$N$_4$," IEEE Photon. Technol. Lett. **31**(10), 771–774 (2019).

163. N. Li, P. Purnawirman, Z. Su, E. S. Magden, P. T. Callahan, K. Shtyrkova, M. Xin, A. Ruocco, C. Baiocco, E. P. Ippen, F. X. Kärtner, J. D. B. Bradley, D. Vermeulen, and M. R. Watts, "High-power thulium lasers on a silicon photonics platform," Opt. Lett. **42**(6), 1181–1184 (2017).

164. C. I. van Emmerik, M. Dijkstra, M. de Goede, L. Chang, J. Mu, and S. M. Garcia-Blanco, "Single-layer active-passive Al$_2$O$_3$ photonic integration platform," Opt. Mater. Express **8**(10), 3049–3054 (2018).

165. C. G. H. Roeloffzen, M. Hoekman, E. J. Klein, L. S. Wevers, R. B. Timens, D. Marchenko, D. Geskus, R. Dekker, A. Alippi, R. Grootjans, A. van Rees, R. M. Oldenbeuving, J. P. Epping, R. G. Heideman, K. Wörhoff, A. Leinse, D. Geuzebroek, E. Schreuder, P. W. L. van Dijk, I. Visscher, C. Taddei, Y. Fan, C. Taballione, Y. Liu, D. Marpaung, L. Zhuang, M. Benelajla, and K. Boller, "Low-Loss Si$_3$N$_4$ TriPleX Optical Waveguides: Technology and Applications Overview," IEEE J. Sel. Top. Quantum Electron. **24**(4), 1–21 (2018).

166. N. Li, D. Vermeulen, Z. Su, E. S. Magden, M. Xin, N. Singh, A. Ruocco, J. Notaros, C. V. Poulton, E. Timurdogan, C. Baiocco, and M. R. Watts, "Monolithically integrated erbium-doped tunable laser on a CMOS-compatible silicon photonics platform," Opt. Express **26**(13), 16200–16211 (2018).

167. K. Wörhoff, R. G. Heideman, A. Leinse, and M. Hoekman, "TriPleX: a versatile dielectric photonic platform," Adv. Opt. Technol. **4**(2), 189–207 (2015).

168. D. J. Blumenthal, R. Heideman, D. Geuzebroek, A. Leinse, and C. Roeloffzen, "Silicon Nitride in Silicon Photonics," Proceedings of the IEEE **106**(12), 2209–2231 (2018).

169. C. J. Krückel, A. Fülöp, Z. Ye, P. A. Andrekson, and V. Torres-Company, "Optical bandgap engineering in nonlinear silicon nitride waveguides," Opt. Express **25**(13), 15370–15380 (2017).

170. J. Kischkat, S. Peters, B. Gruska, M. Semtsiv, M. Chashnikova, M. Klinkmüller, O. Fedosenko, S. Machulik, A. Aleksandrova, G. Monastyrskyi, Y. Flores, and W. T. Masselink, "Mid-infrared optical properties of thin films of aluminum oxide, titanium dioxide, silicon dioxide, aluminum nitride, and silicon nitride," Appl. Opt. **51**(28), 6789–6798 (2012).

171. M. Quirk and J. Serda, *Semiconductor Manufacturing Technology* (Prentice Hall, 2001).

172. C. J. Krückel, A. Fülöp, T. Klintberg, J. Bengtsson, P. A. Andrekson, and V. Torres-Company, "Linear and nonlinear characterization of low-stress high-confinement silicon-rich nitride waveguides," Opt. Express **23**(20), 25827–25837 (2015).

173. K. Ikeda, R. E. Saperstein, N. Alic, and Y. Fainman, "Thermal and Kerr nonlinear properties of plasma-deposited silicon nitride/silicon dioxide waveguides," Opt. Express **16**(17), 12987–12994 (2008).

174. A. Klenner, A. S. Mayer, A. R. Johnson, K. Luke, M. R. E. Lamont, Y. Okawachi, M. Lipson, A. L. Gaeta, and U. Keller, "Gigahertz frequency comb offset stabilization based on supercontinuum generation in silicon nitride waveguides," Opt. Express **24**(10), 11043–11053 (2016).

175. M. Karpov, H. Guo, A. Kordts, V. Brasch, M. H. P. Pfeiffer, M. Zervas, M. Geiselmann, and T. J. Kippenberg, "Raman Self-Frequency Shift of Dissipative Kerr Solitons in an Optical Microresonator," Phys. Rev. Lett. **116**(10), 103902 (2016).

176. J. F. Bauters, M. J. R. Heck, D. John, D. Dai, M.-C. Tien, J. S. Barton, A. Leinse, R. G. Heideman, D. J. Blumenthal, and J. E. Bowers, "Ultra-low-loss high-aspect-ratio Si_3N_4 waveguides," Opt. Express **19**(4), 3163–3174 (2011).

177. M. H. P. Pfeiffer, A. Kordts, V. Brasch, M. Zervas, M. Geiselmann, J. D. Jost, and T. J. Kippenberg, "Photonic Damascene process for integrated high-Q microresonator based nonlinear photonics," Optica **3**(1), 20–25 (2016).

178. Epping, J.P., Boller, K.-J., Fallnich, C., Laser Physics & Nonlinear Optics, and Faculty of Science and Technology, "Dispersion engineering silicon nitride waveguides for broadband nonlinear frequency conversion," PhD Thesis, University of Twente (2015).

179. N. Daldosso, M. Melchiorri, F. Riboli, M. Girardini, G. Pucker, M. Crivellari, P. Bellutti, A. Lui, and L. Pavesi, "Comparison among various Si_3N_4 waveguide geometries grown within a CMOS fabrication pilot line," J. Light. Technol. **22**(7), 1734–1740 (2004).

180. A. Gondarenko, J. S. Levy, and M. Lipson, "High confinement micron-scale silicon nitride high Q ring resonator," Opt. Express **17**(14), 11366–11370 (2009).

181. B. Stern, X. Ji, Y. Okawachi, A. L. Gaeta, and M. Lipson, "Battery-operated integrated frequency comb generator," Nature **562**(7727), 401–405 (2018).

182. K. Luke, A. Dutt, C. B. Poitras, and M. Lipson, "Overcoming Si_3N_4 film stress limitations for high quality factor ring resonators," Opt. Express **21**(19), 22829–22833 (2013).

183. J. P. Epping, M. Hoekman, R. Mateman, A. Leinse, R. G. Heideman, A. van Rees, P. J. M. van der Slot, C. J. Lee, and K.-J. Boller, "High confinement, high yield Si_3N_4 waveguides for nonlinear optical applications," Opt. Express **23**(2), 642–648 (2015).

184. M. H. P. Pfeiffer, C. Herkommer, J. Liu, H. Guo, M. Karpov, E. Lucas, M. Zervas, and T. J. Kippenberg, "Octave-spanning dissipative Kerr soliton frequency combs in Si_3N_4 microresonators," Optica **4**(7), 684–691 (2017).

185. M. H. P. Pfeiffer, J. Liu, A. S. Raja, T. Morais, B. Ghadiani, and T. J. Kippenberg, "Ultra-smooth silicon nitride waveguides based on the Damascene reflow process: fabrication and loss origins," Optica **5**(7), 884–892 (2018).

186. A. S. Raja, A. S. Voloshin, H. Guo, S. E. Agafonova, J. Liu, A. S. Gorodnitskiy, M. Karpov, N. G. Pavlov, E. Lucas, R. R. Galiev, A. E. Shitikov, J. D. Jost, M. L. Gorodetsky, and T. J. Kippenberg, "Electrically pumped photonic integrated soliton microcomb," Nature Communications **10**(1), 680 (2019).

187. X. Cheng, J. Hong, A. M. Spring, and S. Yokoyama, "Fabrication of a high-Q factor ring resonator using LSCVD deposited Si_3N_4 film," Opt. Mater. Express **7**(7), 2182–2187 (2017).

188. K. Ikeda, R. E. Saperstein, N. Alic, and Y. Fainman, "Thermal and Kerr nonlinear properties of plasma-deposited silicon nitride/silicon dioxide waveguides," Opt. Express **16**(17), 12987–12994 (2008).

189. S. M. Martinussen, R. N. Frentrop, M. Dijkstra, and S. M. Garcia-Blanco, "Redeposition-Free Deep Etching in Small KY(WO$_4$)$_2$ Samples," Micromachines **11**(12), 1033 (2020).

190. S. M. Martinussen, R. N. Frentrop, M. Dijkstra, F. Segerink, V. Tormo-Márquez, J. Olivares, and S. M. Garcia-Blanco, "Pedestal microdisks in potassium yttrium double tungstate," Opt. Mater. Express **9**(8), 3371–3378 (2019).

CHAPTER 2

KY(WO$_4$)$_2$ etching using ICP-RIE

This chapter investigates in detail the etching process of KY(WO$_4$)$_2$ microstructures. Inductively coupled plasma reactive ion etching (ICP-RIE) is used to achieve a high etching rate with a high selectivity towards the etching mask. The optimized process etches KY(WO$_4$)$_2$ at a rate of 125 nm/minute and exhibits high resilience to fluctuations in gas flow and pressure. A selectivity of 2.6 for photoresist and 1.2 for SiO$_2$ was obtained. Amorphous carbon has higher selectivity as mask material, up to 10, which can lead to higher resolution patterning. However, fabrication is found to be too challenging to warrant further use.

2.1 Introduction

Potassium double tungstates like $KY(WO_4)_2$, $KLu(WO_4)_2$ and $KGd(WO_4)_2$ have been in use as laser crystals for decades. They are versatile materials that exhibit excellent optical properties such as a high Raman gain [1] and high emission and absorption cross-sections when doped with rare earth ions [2]. Laser sources developed in these materials include bulk ultrafast [3–6], high power [4,7] and Raman [8–10] lasers and high gain waveguide amplifiers [11,12] and lasers [7,13–19] in low index contrast waveguides. However, higher refractive index contrast integrated waveguides are desirable because of their high field confinement, which leads to low laser threshold power, higher laser efficiency and permits the realization of structures requiring tight bends, such as ring resonator lasers.

In order to reliably fabricate high refractive index contrast waveguides in $KY(WO_4)_2$, it is crucial to have an etching process that permits deep etching without introducing sidewall roughness, is stable and has a wide process latitude, i.e. robustness to fluctuations in process parameters.

High selectivity is essential to maximizing resolution and etch depth. Selectivity is defined as the ratio of the etch rate of $KY(WO_4)_2$ to the etch rate of the mask material, with a ratio higher than 1 indicating more rapid etching of the $KY(WO_4)_2$ than of the mask.

High etching rate is also desirable. Low-power ion beam etching (IBE) of $KY(WO_4)_2$ exhibits etch rates of 2.79 nm/min [20], which leads to very long etching times when deep etching is required (e.g., etching 1 μm at this etch rate takes ~6 hours). Optical grade dicing of $KY(WO_4)_2$ [21] provides a very high throughput. In this method, waveguides are defined by cutting the sidewalls with a dicing blade, without lithography and etching steps. Although very fast, the minimum achievable waveguide width is around 20 μm, bends are not manufacturable, and control of the width of the patterned structures is poor.

In inductively coupled plasma reactive ion etching (ICP-RIE), process fluctuations can include gas flow and chamber pressure. The process performance in terms of mask selectivity and etch rate may also fluctuate. Flow and pressure normally fluctuate little in the short term. However, long term drift of the lowest achievable pressure is possible. The performance of a vacuum system will change over its lifetime, although adequate maintenance

and statistical process control can help obtaining reproducible results. This should be considered and anticipated when operating close to the pump capacity.

The selectivity and etch rate may drift due to changes in the chamber condition. Etching may cause particulate residues [22] or chemically alter the chamber walls [23], depending on the gases that are used and the materials that are etched. Ideally, standard cleaning procedures are able to completely restore the chamber condition. However, ICP-RIE etchers are complex systems with numerous possible points of failure. Major maintenance procedures such as wet cleaning are occasionally necessary due to cumulative wear over a timescale of hundreds or thousands of processing runs [24].

The etch rate may also be non-uniform [25]. The location of a feature on a wafer-scale mask or a displacement of the sample in the chamber can lead to differences in the etched depth. Effects such as micro-loading also occur in chemical etch processes, where open areas are etched more slowly than closed areas, due to a depletion of reactants [26].

While long-term drift is handled by consistent monitoring and maintenance, non-uniformity should be considered from the start of the developments. This is handled by optimizing the etching process, as the plasma density distribution can be influenced by the pressure, ICP power and CCP power [27,28].

The objective of this chapter is to study the most appropriate mask material as well as dry etch process to achieve deep, high-resolution, uniform and stable etching of $KY(WO_4)_2$.

2.2 Theory of inductively coupled plasma reactive ion etching (ICP-RIE)

The etcher used in this work (Oxford Instruments PlasmaPro 100 Cobra) is illustrated schematically in Figure 2.1. The gas is injected from the top, where it is ionized by a powerful AC magnetic field generated by the ICP coils. The coils are water-cooled, and are separated from the vacuum chamber by an alumina tube. Most of the chamber is filled with a glowing plasma. The plasma is generated by ions and electrons that are dissociated by the field and spontaneously recombine, emitting photons. In this work, ions are assumed to be positive unless otherwise mentioned.
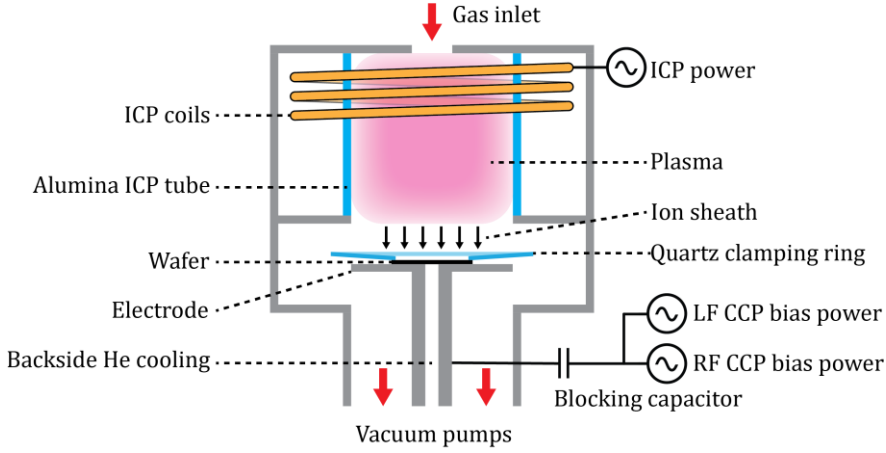
Figure 2.1: Schematic of the ICP-RIE etcher used in this work. The self-generated bias voltage is measured by time-averaging the voltage between the electrode and chamber wall.

At the bottom of the chamber, the wafer is placed on a temperature controlled electrode and held in place with an insulating alumina plate. The electrode is connected to a capacitively coupled plasma (CCP) generator, also called the RF bias generator, which generates an electric field pointing towards the plasma. Because the plasma electrons have a very low mass, they are easily attracted to the electrode at every half cycle, whereas the heavier ions oscillate nearly in place. The electrons add a negative charge to the electrode, which generates a (quasi) DC bias V_{bias} between the electrode and the plasma [25]. A blocking capacitor between the electrode and the CCP generator allows this bias to build up. Both the ICP and CCP generators contain impedance matching networks that eliminate reactive power loss.

The region where this DC bias exists is called the ion sheath or the dark sheath, because there is no glow discharge inside it. The thickness oscillates at the frequency of the CCP bias [29], with a peak thickness, t_s, given by [30]

$$t_s = \frac{j}{q2\pi\nu_{\text{CCP}}[e]} \propto \frac{j}{q2\pi\nu_{\text{CCP}}P_{\text{ICP}}}.$$ (2.1)

Here j is the ion current density [A/m^2], q is the ion charge [C], ν_{CCP} is the CCP frequency [Hz], and $[e]$ is the electron density [m^{-3}], which is assumed to be proportional to the ICP power P_{ICP} [W] [30]. The sheath thickness is not necessarily easy to determine accurately, but it is usually less than 1 mm in a high plasma density ($\geq 10^{11}$ cm^{-3}) system such as an ICP reactor [30].

In the ion sheath, the electric potential is equal to the DC bias plus the AC bias from the CCP generator, and oscillates over time. It is never positive, as any positive potential is instantaneously canceled out as it generates an electron current to the electrode. However, it is near zero for a significant amount of time, during the positive period of the CCP generator [29].

Every positive ion that enters the ion sheath will be swept through it rapidly. In high plasma density systems this occurs over less than one RF period even for 13.56 MHz frequencies [31]. The ion current, or the number of ions that enter the sheath, is primarily dependent on the plasma density, as it is a diffusive process. The ions accumulate an energy equal to their initial thermal energy plus the bias, which goes through a partial oscillation during the transit time.

Because of the oscillation and the brief period of time spent in the sheath, ions will accumulate different amounts of kinetic energy, forming an ion energy distribution (IED). The ions that enter during the negative half period tend to form a high energy peak in the IED. Ions that enter during the positive half period, however, are dominated by their thermal drift velocity plus a modest constant bias, and form a corresponding low energy peak. The IED is then two-peaked, with most energies near zero and the remainder near a maximum.

This is in contrast with low plasma density systems like parallel plate etchers, which do not have an ICP coil and correspondingly have a lower plasma density (10^9-10^{10} cm^{-3}) [30]. In such systems, the ion sheath is too thick for ions to traverse in one high period above a certain frequency, and the ions effectively respond to a time averaged field, not an instantaneous high voltage peak [31]. However, at sufficiently high frequencies the ion transit time is longer than the CCP period even at high plasma density. The time averaged field will then create an IED with a single peak. The single or double-peaked behavior can be predicted using a scaling factor S [30]:

$$S = \frac{\tau_t}{\tau_{CCP}} = \left(\frac{2Mt_s^2}{qV} \right)^{1/2} \nu_{CCP} \qquad (2.2)$$

Here τ_t is the ion transit time [s], τ_{CCP} is the CCP period [s], M is the ion mass [kg], V is the CCP voltage amplitude [V], and ν_{CCP} is the CCP frequency [Hz]. Generally, if $S \gg 1$ the IED is single peaked, whereas if $S \ll 1$ it is double peaked [30]. The double peak distribution generally has much higher peak

energies than single peaks [29], and low frequency CCP biasing can therefore be used to preferentially sputter, rather than etch chemically [32].

As the ions traverse the ion sheath, they may or may not collide with other ions or with radicals [33]. Such collisions transfer momentum between ions and cause changes in both direction and energy. This means that the energy and angle distributions are flattened. The number of high energy impacts on the wafer goes down drastically, with lower energy collisions being favored [33]. A thick ion sheath increases the risk of collisions, as does a high pressure.

The mean free path of ions, which should be much longer than the ion sheath thickness to guarantee a collision-free plasma, is not straightforward to calculate. This is because many collision cross-sections as well as other plasma parameters must be taken into account. However, in an argon plasma the mean free path may be approximated by [34]

$$l_i \approx \frac{1}{330\,P}\,\text{cm}\ (P\ \text{in torr}). \tag{2.3}$$

However, this approximation assumes a plasma with low electron temperature, which is not always the case [28]. Therefore, the actual mean free path may be lower in our system.

Upon impact with the sample, an ion may dislodge one or more atoms. The number of atoms dislodged per incident ion is termed the sputtering yield, and is highly dependent on the ion energy [35]. Near a certain threshold energy, E_{th}, in the low energy regime there is a sharp drop of the sputter yield towards zero. The value of E_{th} is material dependent, and represents the energy needed to remove a single atom from the bulk material. For monoatomic targets, this energy is typically in the low 10's of eV [36]. In ion beam etching (IBE), every ion has the same energy, determined by the acceleration voltage. It is then in principle possible to achieve high selectivities by operating near or below the threshold energy of the mask [37], although this would require very low etch rates. In ICP-RIE, however, this is more challenging because of the flatter ion energy distribution (IED).

2.2.1 ICP-RIE process parameters

In summary, the main parameters for ICP-RIE are the ICP and CCP powers, the CCP frequency, the chamber pressure, and the gas composition and flow. ICP power is the main plasma generating variable, and is proportional to the

plasma density [30]. Because the ion current is dominated by the diffusion of ions into the sheath, a high plasma density increases the ion current, which increases the thickness of the sheath. However, as the sheath thickness is inversely proportional to the plasma density, the overall effect of an increased ICP power is a thinner sheath. Because the CCP power is fixed, a higher ion current must be accompanied by lower sheath voltage and a lower maximum ion energy [29].

The CCP power and frequency, however, are the main variables shaping the IED. Higher CCP powers produce higher RF bias and DC bias voltages, which increases the overall ion energy [29]. The amplitude of the RF bias is in turn linked with a higher ion current and thicker ion sheath. Thick sheaths are associated with a single peaked IED because ions cannot cross in a single RF cycle, or a flattened IED if the sheath is thick enough to be collisional. However, the corresponding shorter transit time at high bias voltage often allows two peaks [30].

The frequency has a large influence on the ion sheath thickness, as seen in Equation (2.1). This determines the ion transit time across the sheath, which together with the sheath thickness determines whether the ions see a time averaged field or an instantaneous high voltage peak. In high plasma density systems, high frequencies are associated with sharper ion energy distribution peaks at an intermediate energy [29]. Lower frequencies give a two-peaked distribution, with the majority of ions having a low energy and a minority having a much higher energy.

Low frequency (LF) CCP in ICP-RIE is uncommon, but has seen some use in certain silicon [38,39] and Al_2O_3 [32] etching processes. In the case of Al_2O_3 it was associated with an increased etch rate, which was ascribed to more sputtering from the heavy fluorocarbon ions. This may be an important effect as Al_2O_3 is relatively chemically inert [40].

The chamber pressure affects the etch differently in two regimes: The collision-free regime at low pressure, and the collisional regime at higher pressures.

In general, increasing the gas pressure causes an increase in plasma density [41] and flattening of the IED [33], even for small pressure variations. However, the plasma density increase is relatively minor, which leads to only minor changes in the ion current. Changing the pressure in the collision-free

regime is, therefore, a way to modulate the peak ion energy with minimal changes to the ion current, unlike tuning the CCP power, which will change both the energy and current.

Above a transition pressure, the ions will start to collide mid-flight within the sheath region. This may cause them to bombard the sample from several angles, which may make the etch more isotropic, and it will severely flatten the IED [33,42,43].

The gas composition is another crucial variable in ICP-RIE. The selection of available reactive species determines the etch chemistry [23,25,44], which is largely beyond the scope of this work. It is notable that the introduction of even small amounts of SF_6 has been found to cause a tremendous drop in the electron density [45] and electron energy [46] in Ar plasma. This drop occurs because the SF_n radicals are strongly electronegative and absorb the electrons present in the plasma to form negative ions. Such a decrease in electron density can drastically increase the thickness of the ion sheath, possibly increasing the chance of ion-ion or ion-radical collisions [30].

The gas flow is not expected to have a major impact on the etch performance in Ar etching. The automated turbopump valve will compensate by opening more to evacuate the chamber faster, in order to keep the pressure constant. Furthermore, due to the purely physical nature of the etch, the etching gas will not be depleted from loading effects such as those seen in silicon etching [44]. However, the wafer is cooled from the back with helium. This cooling system has a leakage rate of approximately 5 sccm, which will slightly dilute the etchant. At higher argon flows, the leaked helium will constitute a smaller portion of the total gas flow.

The shape of the IED therefore depends on a complex interplay between the plasma density, ion mass, CCP frequency, CCP power, and even the size of the blocking capacitor [47].

2.3 Equipment

The etching was performed on an Oxford Instruments PlasmaPro 100 Cobra ICP-RIE. In addition to standard processing capabilities, the Cobra comes equipped with two capacitively coupled plasma (CCP) generators, one operating at high frequency, 13.56 MHz (HF) and one operating at low frequency, 350 kHz (LF). The chamber volume is 15.3 L and the electrode has a diameter of 205 mm. The initial etching recipe [20] used in this work, given

in Table 2.1, was developed on an older Oxford Instruments PlasmaPro 100 that has since been replaced by the current model.

Table 2.1: Original standard recipe for etching $KY(WO_4)_2$.

ICP power	1875 W
HF CCP power	300 W
Ar flow	30 sccm
Pressure	3 mTorr
Electrode temperature	10°C

Layer thickness measurements were performed on two instruments: A J.A. Woollam M-2000 ellipsometer with both a quartz tungsten halogen lamp and a deuterium lamp, and a Filmetrics F50 white light reflectometer with a tungsten halogen lamp. The ellipsometer measures reflectance and polarization rotation at several angles, at wavelengths between 400 nm and 1600 nm. The reflectometer measures reflectance at a normal angle of incidence, at wavelengths between 400 nm and 1000 nm. This makes the ellipsometer superior for challenging applications like very thin films, opaque materials, and complex layer stacks. The reflectometer, however, offers faster measurements of standard materials, preferably at thicknesses where interference fringes are visible. Both instruments calculate the layer thickness by calculating reflection spectra from an appropriate stack of layers and fitting the layer parameters to the measurements.

Weighing was performed on a Sartorius ME35S-0CE scale with an accuracy of 1 µg, as a proxy for thickness measurement by taking density into consideration.

Rough thickness measurements of thick samples were performed on a HEIDENHAIN MT 60M length gauge with an accuracy of 0.5 µm.

2.4 Uniformity verification

The process parameters ICP and CCP power generate the plasma and are responsible for its uniformity on a scale of several centimeters. Non-uniformity leads to an etch rate that is not constant over the entire wafer, with subsequent reduction of process control and yield. To investigate the uniformity of the etch rate, the ICP power was held constant as in Table 2.1, and the CCP HF power was varied from 50 W to 300 W at steps of 50 W.

Six 100 mm Si wafers were overgrown with 2 μm thick thermal oxide. Each of these wafers were etched for 10 minutes using variations of the standard recipe (Table 2.1) and no mask. Before and after etching, the uniformity of the thermal oxide layer was examined by wafer-scale ellipsometric measurements. The measurements were made in a cross pattern, at the points indicated in Figure 2.2.
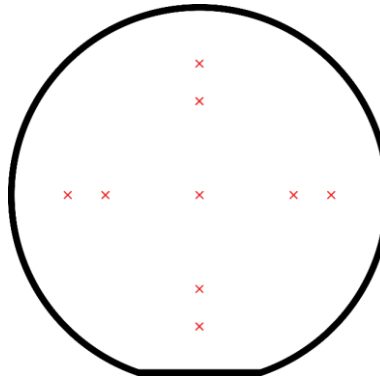

Figure 2.2: Schematic of a 100 mm silicon wafer with the measurement points for ellipsometry marked in red. The points are located immediately at the center, and at 25 and 35 mm away from it.

A summary of the etch rates is given in Table 2.2. In these processes, the rest of the parameters are as indicated in Table 2.1. The etch rate is observed to increase with increasing HF power, as expected. However, there is a significant increase in non-uniformity at lower powers, especially 100 W and below. The interplay between ICP and CCP power is known to affect the plasma uniformity and energy distribution [27,28]. The wafer etched at 200 W likely constitutes an outlier, as a linear slope across the wafer was observed in this measurement, and the bias voltage was significantly lower than expected. A slight slope is also observed at 250 W. As expected, the bias voltage increases with CCP power, except at 200 W.

In Figure 2.3, the etch uniformity for 100 W, 150 W and 300 W are plotted together. The uniformity at a point is calculated as its etch rate divided by the center etch rate. The figures are normalized and shifted so that the center of the wafer is defined as 100%, and each grid marking above or below represents a difference of 1%. Only the points forming a line from left to right are shown.

From Figure 2.3, it is evident that the 300 W etch is very uniform over a large section of the wafer, with some divergence near the edges. In contrast, the

100 W and 150 W recipes exhibit a dip near the center, much more pronounced at 50 W and 100 W. The uniformity for 300 W visible in the figure is better than that seen in Table 2.2. This is because the table includes measurements done in both directions.

Table 2.2: Summary of etch rate, bias voltage and uniformity of silicon oxide as a function of HF CCP power. Datapoints from the outermost 15 mm of the wafer are excluded from the analysis. The range in nm/minute is defined as the difference between the maximum and minimum etch rate, and the range in % is defined as this difference divided by the mean rate.

HF W	Center rate nm/min	Range nm/min	Range %	V_{bias} V
50	38	4.5	11.4	34
100	72	3.5	4.7	55
150	95	2.4	2.5	105
200	110	5.8	5.2	66
250	123	1.5	1.2	183
300	130	2.2	1.7	252
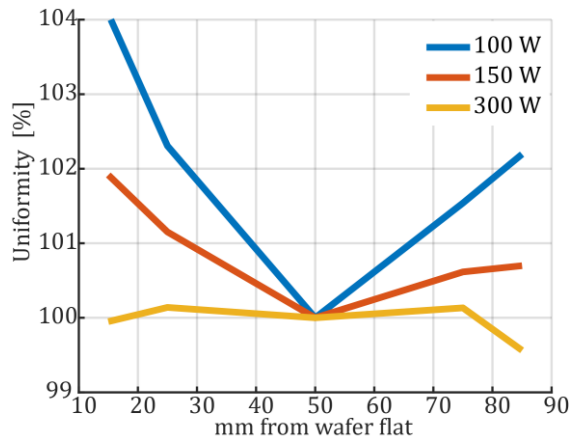
Figure 2.3: Etch uniformity across a 100 mm Si wafer for CCP HF powers of 100 W, 150 W and 300 W. y-axis ticks correspond to a change of 1%. Each plot is normalized so that the center is 100%. The 300 W power yields the highest uniformity. The second outermost datapoint remains included to illustrate the limits of uniformity.

2.5 Selectivity testing

In order to optimize the etching recipe for selectivity, a number of etch recipes were evaluated (Table 2.3). The effect of HF and LF powers, etching chemistry

(addition of fluorine versus chlorine), operating pressure, and gas flow on the selectivity of the etch versus mask materials are investigated.

Recipes 1-6 investigate the effect of the HF CCP power on the selectivity. The HF power varied from 300 W (standard recipe) to 150 W in steps of 50 W. Recipes 7-10 turn off the HF power and replace it with LF. The maximum available LF power is 120 W, which is lower than half of the maximum HF power, because of a smaller power supply.

Recipes 11-14 investigate the effect of fluorine chemistry in the form of SF_6 (recipes 11-12), or a chlorine chemistry with Cl_2 (recipes 13-14). HBr and BCl_3 are also available on the system, however these gases have previously been found to be ineffective [20]. Fluorine based $KY(WO_4)_2$ etching has previously been used by other researchers [20,48], however chlorine etching has never been reported before. In these recipes, the argon flow is reduced correspondingly to set the reactive gas contribution to 10% (recipes 11, 13) and 20% (recipes 12, 14) of the total flow.

Recipes 15-17 have an increased chamber pressure for a purely physical process with an HF power of 150 W and Ar flow of 30 sccm. In addition to seeing the stability of the process with regards to pressure fluctuations, it is interesting to know what the transition pressure is and what effects occur above it.

The mean free path, given by (2.3), is calculated to be 10 mm, 3.4 mm, 2 mm and 0.6 mm at pressures of 3 mTorr, 9 mTorr, 15 mTorr and 50 mTorr respectively. It is assumed that the ion sheath is less than 1 mm thick and that (2.3) somewhat overestimates the mean free path. It is therefore likely that the maximum pressure of 50 mTorr will see at least some degree of collisions.

Recipes 18 and 19 increase the argon flow.

The recipes were tested using two undoped, approximately 10 mm × 10 mm × 1 mm $KY(WO_4)_2$ samples diced along the a^*, b^* and c^* crystal axes with the a^*-c^* plane facing up, one silicon sample coated with ~3500 nm Olin OiR 908-35 photoresist (resist mask), one silicon sample coated with ~2100 nm PECVD SiO_2 (hard mask) and one silicon sample coated with ~175 nm sputtered amorphous carbon (thin hard mask). The silicon samples all came from 100 mm wafers that were diced into 10 mm × 10 mm pieces after coating.

The samples were fixed to a silicon carrier wafer using a minimal layer of Fomblin oil for thermal contact and adhesion. Each etching procedure was performed for two rounds of 5 minutes, so that the samples could be visually inspected halfway in case of over-etching. In case of rapid etching, the carbon samples were removed, as the layers were comparatively thin. This was the case for the etch recipes with a carbon etch rate over 18 nm/minute.

The $KY(WO_4)_2$ etch rate was measured by precision weighing. This method was chosen because it is highly time and cost-effective, and allows re-use of the samples. To calibrate the thickness to weight ratio, the sample thicknesses were initially measured with the HEIDENHAIN gauge and compared with the weight. The change of thickness of each sample was calculated using its own weight to thickness ratio, with the average being 1.65 μg/nm. As the accuracy of the scale is 1 μg, weighing can measure thickness changes of 0.6 nm. Prior to weighting the samples, the residual Fomblin oil was removed by rinsing the samples with acetone followed by a 5 minute dip in 99% HNO_3. They were then rinsed in deionized water, spin dried and dehydration baked on a clean carrier wafer before weighing.

For the silicon samples, the thicknesses of the different layers deposited on the silicon were measured before and after etching. The SiO_2 and photoresist layers were measured by the reflectometer, while the carbon layers were measured by ellipsometer. The silicon samples were not re-used.

Table 2.3: Enumerated list of the etch recipes evaluated in this work. The variable of particular interest for each etch recipe is highlighted. The relevant parameters are HF power, LF power, gas flow of argon, SF_6 and Cl_2, and chamber pressure.

	ICP	HF	LF	Ar	SF_6	Cl_2	P
	W	W	W	sccm	sccm	sccm	mTorr
1	1875	50	0	30	0	0	3
2	1875	100	0	30	0	0	3
3	1875	150	0	30	0	0	3
4	1875	200	0	30	0	0	3
5	1875	250	0	30	0	0	3
6	1875	300	0	30	0	0	3
7	1875	0	30	30	0	0	3
8	1875	0	60	30	0	0	3
9	1875	0	90	30	0	0	3
10	1875	0	120	30	0	0	3
11	1875	150	0	27	3	0	3
12	1875	150	0	24	6	0	3
13	1875	150	0	27	0	3	3
14	1875	150	0	24	0	6	3
15	1875	150	0	30	0	0	9
16	1875	150	0	30	0	0	15
17	1875	150	0	30	0	0	50
18	1875	150	0	15	0	0	3
19	1875	150	0	70	0	0	3

The results of the etching tests are given in Table 2.4 to 2.6.

Table 2.4 shows the effect of CCP power and frequency (i.e., HF and LF). With HF, the etch rate is high and directly proportional to the power. The selectivity of every mask is above 1 except at 50 W where SiO_2 has a selectivity of 0.6. Carbon in particular offers a very high selectivity, while SiO_2 offers the lowest. With LF, $KY(WO_4)_2$ etches at a near-zero rate, while the mask materials etch rapidly, yielding very low selectivities. Etching with 30 W LF power is sufficiently slow that the measured etch rate is below zero, which is an unphysical result.

Table 2.4: Results for etch tests involving CCP power and frequency. Etch rates are given in nm/minute.

No.	Parameter	KY(WO$_4$)$_2$ Rate nm/min	Resist Rate nm/min	Sel.	SiO$_2$ Rate nm/min	Sel.	Carbon Rate nm/min	Sel.	V_{bias} V
1	HF 50 W	30	12	2.6	49	0.6	3	10.4	85
2	HF 100 W	83	27	3.1	81	1.0	9	8.9	155
3	HF 150 W	124	47	2.6	107	1.2	15	8.2	203
4	HF 200 W	153	68	2.3	123	1.2	18	8.5	255
5	HF 250 W	190	76	2.5	135	1.4	22	8.8	294
6	HF 300 W	221	97	2.3	146	1.5	31	7.1	340
7	LF 30 W	-4	8	-0.5	32	-0.1	2	-0.6	58
8	LF 60 W	7	20	0.4	57	0.1	7	1.1	133
9	LF 90 W	4	49	0.1	91	0.0	16	0.2	206
10	LF 120 W	10	72	0.1	101	0.1	19	0.5	255

For HF in KY(WO$_4$)$_2$, a linear fit yields the expression $r = 0.746\,P + 3$ for the etch rate, r, in nm/minute as a function of the power, P, in W, with $R^2 = 0.99$. This indicates that the etch rate is directly proportional to the power and only becomes zero at zero power, or at a point far lower than the powers explored here. There is a slight tendency towards higher selectivity for SiO$_2$ masks at higher power, and lower selectivity for carbon as the power increases. No systematic trend is visible for resist masks. We hypothesize that this is due to different sputtering threshold energies. If KY(WO$_4$)$_2$ has an E_{th} higher than SiO$_2$, similar to OiR resist and lower than carbon, this will explain the trends. However, extremely low CCP powers would be needed to fully exploit this. Furthermore, the low etch rates of carbon mean that its measurements are prone to error, and the trend may be an artifact.

As expected, the bias voltage increases with higher powers. However, it is noted that the bias voltage is different from that shown in Table 2.2. This may

be explained by the use of a conductive silicon carrier wafer rather than one with an insulating SiO_2 coating. In Figure 2.1, the blocking capacitor separates the ICP generator from the rest of the system, consisting of an electrode, wafer and plasma. In an equivalent circuit, inserting an insulating rather than conductive wafer means placing a second capacitor in series with the blocking capacitor. This will cause a different measured V_{bias}, although the specific effects cannot be stated without intimate knowledge of the matching network, ICP generator, and plasma dynamics.

In contrast, LF biasing has little to no effect on the $KY(WO_4)_2$, even at the highest power setting. At 30 W a negative etch rate was measured, which is ascribed to plasma hardened Fomblin oil, which can be hard to remove completely. Hardened oil will therefore be added to the measured $KY(WO_4)_2$ weight, introducing a source of uncertainty. Another possibility is that the before measurement was more than 1 µg off due to an undetected dust particle, and that no etching occurred. All the mask materials, however, etch as fast as with HF at similar bias voltage, which severely reduces the selectivity.

The drop in the $KY(WO_4)_2$ etch rate with LF is remarkable, especially considering that the other materials did not see such a drop. We hypothesize that the origin lies in the two-peaked IED at LF, where the majority of ions have a low energy. If it is the case that the low energy ions are able to etch the mask materials due to a lower E_{th}, but the E_{th} of $KY(WO_4)_2$ is too high, a smaller proportion of the ion current contributes to the sputtering.

We note that the ion sheath thickness is inversely proportional to the CCP frequency. Therefore, a 350 kHz CCP frequency will cause the sheath to be 38 times thicker than a 13.56 MHz frequency, all other things assumed equal. Such an increase in the thickness may increase the risk of collisions and reduce the peak ion energy. However, neither of these effects adequately explain the extremely low etch rates for $KY(WO_4)_2$ and high etch rates for the mask materials. The above results indicate that HF etching is superior to LF for the etching of $KY(WO_4)_2$, with the ideal power possibly being dependent on the mask material.

Table 2.5 shows the effect of chemical composition of the plasma. In contrast with previous research [48], introducing SF_6 reduces the etch rate of $KY(WO_4)_2$. As expected, SF_6 increases the etch rate of every mask, as they are made from chemically susceptible materials that easily react with F^-. This reduces the selectivities dramatically.

Similarly, Cl_2 slows down $KY(WO_4)_2$ etching and increases the mask etching rate, although the effect is not as severe. A slight increase in bias voltage is observed with SF_6, but not with Cl_2. In conclusion, addition of SF_6 or Cl_2 is not beneficial in $KY(WO_4)_2$ etching using these mask materials.

Table 2.5: Results for etch tests involving gas composition. Etch rates are given in nm/minute.

		$KY(WO_4)_2$	Resist		SiO_2		Carbon		
No.	Parameter	Rate nm/min	Rate nm/min	Sel.	Rate nm/min	Sel.	Rate nm/min	Sel.	V_{bias} V
1	Ar 100%	153	47	2,6	107	1,2	15	8,2	203
11	SF_6 10%	94	216	0,3	98	0,7	37	1,9	224
12	SF_6 20%	62	551	0,1	163	0,4	<37	<0,3	227
13	CL_2 10%	61	123	0,5	49	1,2	15	4,0	202
14	CL_2 20%	46	166	0,3	41	1,1	53	0,9	214

Table 2.6 shows the effect of chamber pressure. Up to and including 15 mTorr, the only systematic difference appears to be an increase in carbon etch rate and a corresponding drop in selectivity with respect to a carbon mask. At 50 mTorr, likely outside the collision-free regime, the $KY(WO_4)_2$ etch rate is reduced by 60%. We ascribe this reduction of etch rate to lower ion energies due to collisions. The selectivity with respect to all the mask materials is also reduced for a pressure of 50 mTorr. In one trial, the photoresist was even reticulated [49] and the experiment had to be performed again. The reticulation and selectivity reduction for the polymer resist may be linked to more efficient heat transport from the plasma to the sample.

While the exact limit of the collision free regime is not found, it is concluded that it is far away from the standard process pressure of 3 mTorr. The bias voltage is slightly reduced at 15 mTorr, but slightly higher at 50 mTorr. This is in line with other research that has seen decreased ion energies even at moderate changes in pressure [33].

Table 2.6: Results for etch tests involving chamber pressure. Etch rates are given in nm/minute.

No.	Parameter	KY(WO$_4$)$_2$ Rate nm/min	Resist Rate nm/min	Sel.	SiO$_2$ Rate nm/min	Sel.	Carbon Rate nm/min	Sel.	V_{bias} V
1	3 mTorr	124	47	2.6	107	1.2	15	8.2	203
15	9 mTorr	124	51	2.4	105	1.2	17	7.3	198
16	15 mTorr	128	35	3.7	114	1.1	23	5.6	193
17	50 mTorr	49	35	1.4	59	0.8	14	3.4	210

Table 2.7 shows the effect of argon gas flow. The masks are etched at the same rate both at a lower and higher flow, while KY(WO$_4$)$_2$ is etched faster at higher flows. The only change to etching parameters at different gas flows is the contribution of the helium that leaks from the backside wafer cooling. At an argon flow of 15 sccm the helium will constitute 25% of the atoms in the chamber if the leakage rate is 5 sccm. At higher argon flows, the relative dilution is reduced correspondingly.

If helium, a much lighter atom, etches KY(WO$_4$)$_2$ slowly, but is able to etch the mask materials, this will explain the change in selectivity. However, further experiments are necessary to confirm this hypothesis. In conclusion, a higher gas flow is desirable as it will reduce the influence of helium leakage, which may vary by a few sccm from run to run.

Table 2.7: Results for etch tests involving total gas flow. Etch rates are given in nm/minute.

		KY(WO$_4$)$_2$	Resist		SiO$_2$		Carbon		
No.	Parameter	Rate nm/min	Rate nm/min	Sel.	Rate nm/min	Sel.	Rate nm/min	Sel.	V_{bias} V
18	15 sccm	118	48	2.5	112	1.1	13	9.2	202
3	30 sccm	124	47	2.6	107	1.2	15	8.2	203
19	70 sccm	144	47	3.1	106	1.4	14	10.3	202

Based on these results, we arrive at an optimized etching recipe, given in Table 2.8. The CCP power is set to 150 W HF, as lower sidewall roughness has been observed with this power than with higher power. The gas flow has been set to 70 sccm. A selectivity of ~3 with respect to resist was experimentally demonstrated.

Table 2.8: Optimized etching recipe for etching KY(WO$_4$)$_2$.

ICP power	1875 W
HF CCP power	150 W
Ar flow	70 sccm
Pressure	3.5 mTorr
Table temperature	10°C

Figure 2.4 shows an example of structures etched using the optimized recipe and a 5 μm thick SiO$_2$ hard mask. The structures are etched 3 μm deep and show a significant of redeposition on the sidewalls, which is an issue that has not been addressed in this chapter.
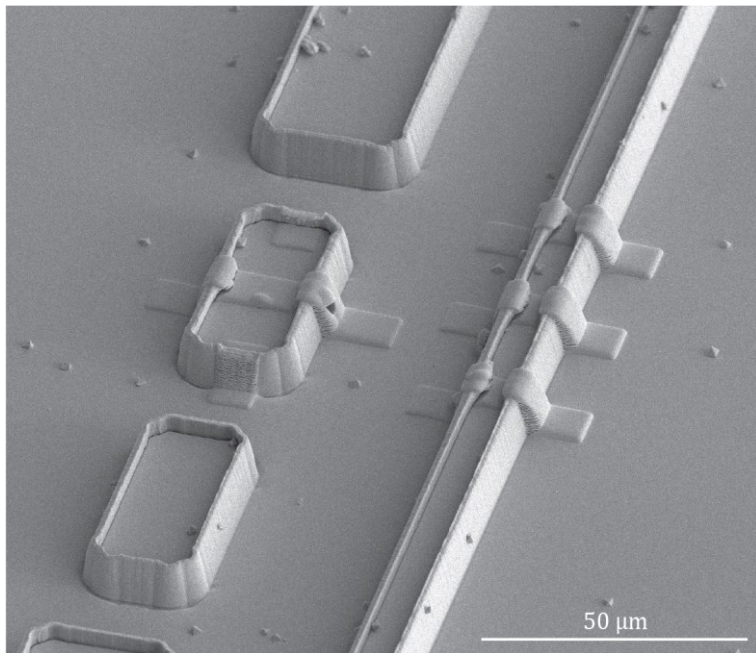
Figure 2.4: 3 μm deep etched structures in KY(WO$_4$)$_2$ made using the optimized recipe and a 5 μm thick SiO$_2$ hard mask. Pt has been deposited in patches for analysis using focused ion beam milling, which is not shown here.

2.6 Amorphous carbon as a hard mask

The results of the etching tests have shown that carbon offers extremely high selectivity as an etching mask. However it is a challenging material to work with, which has prevented it from being adopted after this study: Sputtered amorphous carbon is highly fragile and adheres poorly to KY(WO$_4$)$_2$. The adhesion problems may be solved by depositing a 20 nm PECVD SiO$_2$ layer on the KY(WO$_4$)$_2$ sample before carbon sputtering. Following this step, the carbon layer is deposited by sputter deposition. A deposition rate of 1 nm/minute was achieved on the custom built sputter coater used in the MESA+ cleanroom, as a low etching rate in a sputter etching system also implies that the growth rate in a sputter coater will be low.

After the carbon thin film deposition, a 100 nm PECVD SiO$_2$ capping layer needs to be deposited for protection. Without this layer, the film will delaminate easily during the wet processing steps necessary for photoresist coating. However, delamination can occur even with the adhesion and capping layers. An example of this is shown in Figure 2.5.
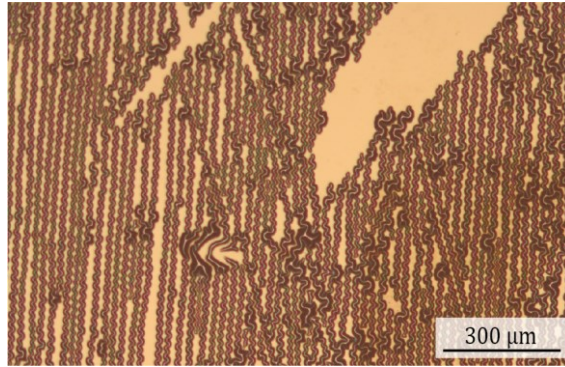
Figure 2.5: Optical microscope image of an SiO$_2$ capped carbon thin film delaminating from a silicon wafer following a quick dump rinsing process.

After the capping layer is deposited, photolithography may be performed on the sample. The SiO$_2$ layer may be then opened by ICP-RIE and the carbon hard mask may be opened by oxygen ICP-RIE etching. The oxygen etching step, unlike SiO$_2$ etching, is not a standard process in most cleanrooms and must be developed and optimized for smooth sidewalls.

However, it is desirable to remove the residual photoresist mask after lithography, in order to use only the very thin carbon hard mask. If this is not done, the redeposition will extend vertically to the height of the photoresist, which is much thicker than the carbon.

In this case, a fourth layer must be deposited. We have opted for a 30 nm sputtered silicon layer, as it can be opened quickly with standard ICP-RIE processing and offers excellent selectivity during the SiO$_2$ etching step.

Summarizing these steps, the carbon hard mask consists of a 20 nm SiO$_2$ adhesion layer, ~175 nm carbon, 100 nm SiO$_2$, 30 nm Si and a photoresist layer of arbitrary thickness. The mask is opened by Si dry etching, photoresist removal, SiO$_2$ dry etching, and oxygen based carbon dry etching. The KY(WO$_4$)$_2$ sample can be etched by Ar ICP-RIE following this procedure, without removing the initial SiO$_2$ adhesion layer. The complete flow is illustrated in Figure 2.6, starting after the deposition of the complete mask layer stack.
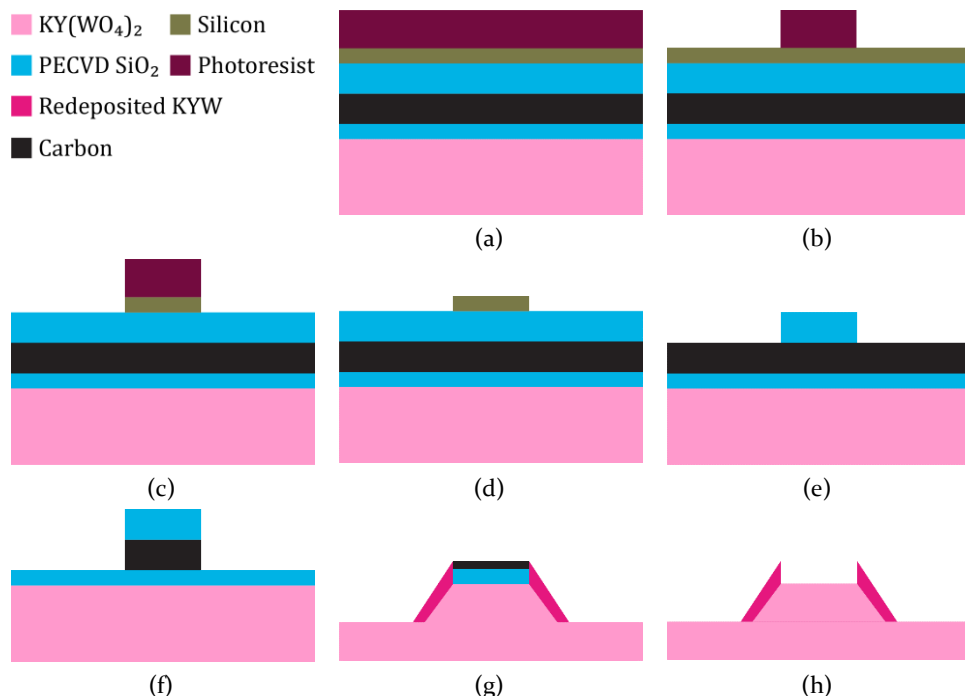
Figure 2.6: Proposed process flow for carbon as a hard mask. (a) Full layer stack consisting of KY(WO$_4$)$_2$, SiO$_2$, carbon, SiO$_2$, silicon and photoresist. (b) Photolithography. (c) ICP-RIE etch to open silicon. (d) Removal of photoresist by HNO$_3$ or oxygen plasma. (e) ICP-RIE etch to open SiO$_2$, likely consuming silicon. (f) ICP-RIE etch to open carbon without consuming SiO$_2$. (g) ICP-RIE etch through KY(WO$_4$)$_2$, producing redeposition as high as the remaining mask. (h) Stripping of carbon and SiO$_2$ by HNO$_3$ and HF.

This is a very long and elaborate process, with many steps that can go wrong and cause the carbon layer to delaminate. For this reason, carbon masking has been deemed undesirable for further processing.

2.7 Conclusion

The etching uniformity of an argon based ICP-RIE process for KY(WO$_4$)$_2$ has been investigated, and the process parameters have been tuned for optimal selectivity. The starting recipe has been confirmed to be close to optimal, however a decreased HF CCP power and increased gas flow have improved the performance. A completely inert atmosphere is ideal for optimizing selectivity and etch rate. Carbon offers a selectivity of 8-10, however processing it is very challenging and time consuming. Olin OiR 908 photoresist offers a selectivity of 3.1, and SiO$_2$ offers a selectivity of 1.4. Based on these results, etching using photoresist or SiO$_2$ is recommended.

Bibliography

1. J. A. Piper and H. M. Pask, "Crystalline Raman Lasers," IEEE J. Sel. Top. Quantum Electron. **13**(3), 692–704 (2007).
2. Y.-S. Yong, S. Aravazhi, S. A. Vázquez-Córdova, J. J. Carvajal, F. Díaz, J. L. Herek, S. M. Garcia-Blanco, and M. Pollnau, "Direct confocal lifetime measurements on rare-earth-doped media exhibiting radiation trapping," Opt. Mater. Express **7**(2), 527–532 (2017).
3. A. A. Kovalyov, V. V. Preobrazhenskii, M. A. Putyato, O. P. Pchelyakov, N. N. Rubtsova, B. R. Semyagin, V. E. Kisel', S. V. Kuril'chik, and N. V. Kuleshov, "115 fs pulses from $Yb^{3+}:KY(WO_4)_2$ laser with low loss nanostructured saturable absorber," Laser Phys. Lett. **8**(6), 431–435 (2011).
4. F. Brunner, G. J. Spühler, J. A. Au, L. Krainer, F. Morier-Genoud, R. Paschotta, N. Lichtenstein, S. Weiss, C. Harder, A. A. Lagatsky, A. Abdolvand, N. V. Kuleshov, and U. Keller, "Diode-pumped femtosecond $Yb:KGd(WO_4)_2$ laser with 1.1-W average power," Opt. Lett. **25**(15), 1119–1121 (2000).
5. U. Griebner, S. Rivier, V. Petrov, M. Zorn, G. Erbert, M. Weyers, X. Mateos, M. Aguiló, J. Massons, and F. Díaz, "Passively mode-locked $Yb:KLu(WO_4)_2$ oscillators," Opt. Express **13**(9), 3465–3470 (2005).
6. E. Kifle, X. Mateos, J. R. V. de Aldana, A. Ródenas, P. Loiko, S. Y. Choi, F. Rotermund, U. Griebner, V. Petrov, M. Aguiló, and F. Díaz, "Femtosecond-laser-written $Tm:KLu(WO_4)_2$ waveguide lasers," Opt. Lett. **42**(6), 1169–1172 (2017).
7. K. van Dalfsen, S. Aravazhi, C. Grivas, S. M. Garcia-Blanco, and M. Pollnau, "Thulium channel waveguide laser with 1.6 W of output power and ~80% slope efficiency," Opt. Lett. **39**(15), 4380–4383 (2014).
8. A. A. Kaminskii, P. V. Klevtsov, L. Li, and A. A. Pavlyuk, "Stimulated emission from $KY(WO_4)_2: Nd^{3+}$ crystal laser," Phys. Status Solidi A **5**(2), K79–K81 (1971).
9. Z. Cong, Z. Liu, Z. Qin, X. Zhang, H. Zhang, J. Li, H. Yu, and W. Wang, "LD-pumped actively Q-switched $Nd:KLu(WO_4)_2$ self-Raman laser at 1185 nm," Opt. Laser Technol. **73**, 50–53 (2015).
10. V. Petrov, M. C. Pujol, X. Mateos, Ò. Silvestre, S. Rivier, M. Aguiló, R. M. Solé, J. Liu, U. Griebner, and F. Díaz, "Growth and properties of $KLu(WO_4)_2$, and novel ytterbium and thulium lasers based on this monoclinic crystalline host," Laser Photonics Rev. **1**(2), 179–212 (2007).
11. D. Geskus, S. Aravazhi, S. M. Garcia-Blanco, and M. Pollnau, "Giant optical gain in a rare-earth-ion-doped microstructure," Adv. Opt. Mater. **24**(10), OP19-22 (2012).

12. S. A. Vázquez-Córdova, S. Aravazhi, C. Grivas, Y.-S. Yong, S. M. Garcia-Blanco, J. L. Herek, and M. Pollnau, "High optical gain in erbium-doped potassium double tungstate channel waveguide amplifiers," Opt. Express **26**(5), 6260–6266 (2018).

13. D. Geskus, S. Aravazhi, K. Wörhoff, and M. Pollnau, "High-power, broadly tunable, and low-quantum-defect $KGd_{1-x}Lu_x(WO_4)_2{:}Yb^{3+}$ channel waveguide lasers," Opt. Express **18**(25), 26107–26112 (2010).

14. S. Aravazhi, D. Geskus, K. van Dalfsen, S. A. Vázquez-Córdova, C. Grivas, U. Griebner, S. M. Garcia-Blanco, and M. Pollnau, "Engineering lattice matching, doping level, and optical properties of $KY(WO_4)_2{:}Gd$, Lu, Yb layers for a cladding-side-pumped channel waveguide laser," Appl. Phys. B **111**(3), 433–446 (2013).

15. D. Geskus, S. Aravazhi, C. Grivas, K. Wörhoff, and M. Pollnau, "Microstructured $KY(WO_4)_2{:}Gd^{3+}$, Lu^{3+}, Yb^{3+} channel waveguide laser," Opt. Express **18**(9), 8853 (2010).

16. D. Geskus, S. Aravazhi, E. Bernhardi, C. Grivas, S. Harkema, K. Hametner, D. Günther, K. Wörhoff, and M. Pollnau, "Low-threshold, highly efficient Gd^{3+}, Lu^{3+} co-doped $KY(WO_4)_2{:}Yb^{3+}$ planar waveguide lasers," Laser Phys. Lett. **6**(11), 800–805 (2009).

17. K. van Dalfsen, S. Aravazhi, D. Geskus, K. Wörhoff, and M. Pollnau, "Efficient $KY_{1-x-y}Gd_xLu_y(WO_4)_2{:}Tm^{3+}$ channel waveguide lasers," Opt. Express **19**(6), 5277–5282 (2011).

18. D. Geskus, E. H. Bernhardi, K. van Dalfsen, S. Aravazhi, and M. Pollnau, "Highly efficient Yb^{3+}-doped channel waveguide laser at 981 nm," Opt. Express **21**(11), 13773–13778 (2013).

19. K. van Dalfsen, S. Aravazhi, C. Grivas, S. M. García-Blanco, and M. Pollnau, "Thulium channel waveguide laser in a monoclinic double tungstate with 70% slope efficiency," Opt. Lett. **37**(5), 887–889 (2012).

20. D. Geskus, "Channel waveguide lasers and amplifiers in single-crystalline Ytterbium-doped potassium double tungstates," University of Twente (2011).

21. M. Medina, C. E. Rüter, M. C. Pujol, D. Kip, J. Masons, A. Ródenas, M. Aguiló, and F. Díaz, "$KLu(WO_4)_2/SiO_2$ Tapered Waveguide Platform for Sensing Applications," Micromachines **10**(7), 454 (2019).

22. Y. Ye, D. X. Ma, G. Z. Yin, K. Prasad, M. Siegel, S. S. Y. Mak, P. Martinez, J. S. Papanu, and D. C. Lu, "Method and apparatus for cleaning by-products from plasma chamber surfaces," United States patent US5756400A (May 26, 1998).

23. F. Karouta, Y. C. Zhu, E. J. Geluk, J. J. G. M. van der Tol, J. J. M. Binsma, and M. K. Smit, "ICP etching of InP and its applications in photonic

circuits," in *Photonics: Design, Technology, and Packaging* (International Society for Optics and Photonics, 2004), **5277**, pp. 22–28.

24. Y. Nishi and R. Doering, *Handbook of Semiconductor Manufacturing Technology*, 2nd ed. (CRC Press, 2007).

25. M. Quirk and J. Serda, *Semiconductor Manufacturing Technology* (Prentice Hall, 2001).

26. R. A. Gottscho, C. W. Jurgensen, and D. J. Vitkavage, "Microscopic uniformity in plasma etching," J. Vac. Sci. Technol. B Microelectron. Nanometer Struct. Process. Meas. Phenom. **10**(5), 2133–2147 (1992).

27. H.-C. Lee, J.-Y. Bang, and C.-W. Chung, "Effects of RF bias power on electron energy distribution function and plasma uniformity in inductively coupled argon plasma," Thin Solid Films **519**(20), 7009–7013 (2011).

28. H.-C. Lee, M.-H. Lee, and C.-W. Chung, "Effects of rf-bias power on plasma parameters in a low gas pressure inductively coupled plasma," Appl. Phys. Lett. **96**(7), 071501 (2010).

29. E. A. Edelberg and E. S. Aydil, "Modeling of the sheath and the energy distribution of ions bombarding rf-biased substrates in high density plasma reactors and comparison to experimental measurements," J. Appl. Phys. **86**(9), 4799–4812 (1999).

30. R. J. Hoekstra and M. J. Kushner, "Predictions of ion energy distributions and radical fluxes in radio frequency biased inductively coupled plasma etching reactors," J. Appl. Phys. **79**(5), 2275–2286 (1996).

31. V. M. Donnelly, D. L. Flamm, and R. H. Bruce, "Effects of frequency on optical emission, electrical, ion, and etching characteristics of a radio frequency chlorine plasma," J. Appl. Phys. **58**(6), 2135–2144 (1985).

32. J. Dekker, K. Kolari, and R. L. Puurunen, "Inductively coupled plasma etching of amorphous Al_2O_3 and TiO_2 mask layers grown by atomic layer deposition," J. Vac. Sci. Technol. B **24**(5), 2350–2355 (2006).

33. T. Yagisawa and T. Makabe, "Temporal velocity distribution of positive and negative ions incident on a wafer in a pulsed two-frequency capacitively coupled plasma in CF_4/Ar for SiO_2 etching," IEEE Trans. Plasma Sci. **31**(4), 521–527 (2003).

34. M. A. Lieberman and A. J. Lichtenberg, *Principles of Plasma Discharges and Materials Processing* (John Wiley & Sons, 2005).

35. J. Bohdansky, "A universal relation for the sputtering yield of monatomic solids at normal ion incidence," Nucl. Instrum. Methods Phys. Res. Sect. B **2**(1), 587–591 (1984).

36. J. M. E. Harper, J. J. Cuomo, and H. R. Kaufman, "Technology and applications of broad-beam ion sources used in sputtering. Part II. Applications," J. Vac. Sci. Technol. **21**(3), 737–756 (1982).

37. J. M. E. Harper, J. J. Cuomo, P. A. Leary, G. M. Summa, H. R. Kaufman, and F. J. Bresnock, "Low Energy Ion Beam Etching," J. Electrochem. Soc. **128**(5), 1077 (1981).

38. C. S. Gormley, "Method for etching a tapered bore in a silicon substrate, and a semiconductor wafer comprising the substrate," United States patent US6818564B1 (November 16, 2004).

39. L. V. Jenni, L. Kumar, and C. Hierold, "Hybrid lithography based fabrication of 3D patterns by deep reactive ion etching," Microelectron. Eng. **209**, 10–15 (2019).

40. S.-H. Park, H. Jeon, Y.-J. Sung, and G.-Y. Yeom, "Refractive sapphire microlenses fabricated by chlorine-based inductively coupled plasma etching," Appl. Opt. **40**(22), 3698–3702 (2001).

41. S. Yun, K. Taylor, and G. R. Tynan, "Measurement of radial neutral pressure and plasma density profiles in various plasma conditions in large-area high-density plasma sources," Phys. Plasmas **7**(8), 3448–3456 (2000).

42. S. G. Ingram and N. S. J. Braithwaite, "Ion and electron energy analysis at a surface in an RF discharge," J. Phys. Appl. Phys. **21**(10), 1496–1503 (1988).

43. J. R. Woodworth, M. E. Riley, D. C. Meister, B. P. Aragon, M. S. Le, and H. H. Sawin, "Ion energy and angular distributions in inductively coupled radio frequency discharges in argon," J. Appl. Phys. **80**(3), 1304–1311 (1996).

44. R. Legtenberg, H. Jansen, M. de Boer, and M. Elwenspoek, "Anisotropic Reactive Ion Etching of Silicon Using $SF_6/O_2/CHF_3$ Gas Mixtures," J. Electrochem. Soc. **142**(6), 2020–2028 (1995).

45. L. Lallement, A. Rhallabi, C. Cardinaud, M. C. Peignon-Fernandez, and L. L. Alves, "Global model and diagnostic of a low-pressure SF_6/Ar inductively coupled plasma," Plasma Sources Sci. Technol. **18**(2), 025001 (2009).

46. S.-J. Oh, H.-C. Lee, and C.-W. Chung, "A study on plasma parameters in Ar/SF_6 inductively coupled plasma," Phys. Plasmas **24**(1), 013512 (2017).

47. S.-H. Song and M. J. Kushner, "Role of the blocking capacitor in control of ion energy distributions in pulsed capacitively coupled plasmas sustained in $Ar/CF_4/O_2$," J. Vac. Sci. Technol. A **32**(2), 021306 (2014).

48. M. Medina Martinéz, "$KREW/SiO_2$ waveguide platform for optical sensing applications," Universitat Rovira i Virgili (2019).

49. A. R. Pal, R. L. Bruce, F. Weilnboeck, S. Engelmann, T. Lin, M.-S. Kuo, R. Phaneuf, and G. S. Oehrlein, "Real-time studies of surface roughness development and reticulation mechanism of advanced photoresist materials during plasma processing," J. Appl. Phys. **105**(1), 013311 (2009).

CHAPTER 3

Redeposition-free deep etching in small KY(WO$_4$)$_2$ samples

KY(WO$_4$)$_2$ is a promising material for on-chip laser sources. Deep etching of small KY(WO$_4$)$_2$ samples in combination with various thin film deposition techniques is desirable for the manufacturing of such devices. There are, however, several difficulties that need to be overcome before deep etching of KY(WO$_4$)$_2$ can be realized in small samples in a reproducible manner. In this paper we address the problems of (i) edge bead formation when using thick resist on small samples, (ii) sample damage during lithography mask touchdown, (iii) resist reticulation during prolonged argon based ICP-RIE etching and (iv) redeposited material on the feature sidewalls. We demonstrate the etching of 6.5 µm deep features and the removal of redeposited material using a wet etch procedure. This process will enable the realization of waveguides both in ion irradiated KY(WO$_4$)$_2$ as well as thin KY(WO$_4$)$_2$ membranes transferred onto glass substrate by bonding and subsequent polishing.

3.1 Introduction

Potassium double tungstates like $KY(WO_4)_2$, $KLu(WO_4)_2$ and $KGd(WO_4)_2$ have been in use as laser crystals for decades. They are versatile materials that exhibit excellent optical properties such as a high Raman gain [1] and high emission and absorption cross-sections when doped with rare earth ions [2]. Laser sources developed in these materials include bulk ultrafast [3–6], high power [4,7] and Raman [8–10] lasers and high gain waveguide amplifiers [11,12] and lasers [7,13–19] in low index contrast waveguides However, higher refractive index contrast integrated waveguides are desirable because of their high field confinement, which leads to low laser threshold power, higher laser efficiency and permits the realization of structures requiring tight bends, such as ring resonator lasers.

High refractive index contrast waveguides have recently been proposed based on a combination of dry and wet etch processes on swift heavy ion irradiated $KY(WO_4)_2$ slabs [20,21]. These slabs have a buried region where the refractive index is ~1.85 at 1550 nm, corresponding to amorphous $KY(WO_4)_2$, whereas the top crystalline layer has a refractive index around 2 at 1550 nm. The buried layer can be wet etched using HCl and TMAH [20], which enables the formation of suspended structures. Pedestal microdisks have been demonstrated using this process [20]. However, the dry etched trench should penetrate the barrier completely in order for the HCl solution to reach it. This requires achieving an etch depth of more than 5 μm [21] to produce the suspended structures.

Deep etching capabilities are also necessary for the fabrication of high refractive index contrast waveguides on $KY(WO_4)_2$ membranes obtained by bonding followed by mechanical lapping and polishing [22–24]. Lapping and polishing very thin layers carries great risk of sample damage, while thicker layers are less fragile. Deep etch processing on layers several μm thick may be a viable high yield approach to device fabrication in $KY(WO_4)_2$.

Major problems encountered in the deep etching of $KY(WO_4)_2$ include the presence of a large edge bead, damage to the brittle $KY(WO_4)_2$ sample during the lithography process, resist reticulation and redeposition of sputtered $KY(WO_4)_2$ material, which affects the quality of the waveguide sidewalls. The formation of an edge bead is a well-known problem in all photolithography processing [25]. However, edge bead formation is exacerbated by the viscous resist needed to achieve deep etching in combination with the typically small

size of KY(WO$_4$)$_2$ substrates. Furthermore, most photolithography equipment available in multiuser cleanrooms is optimized for 4-inch wafers, and mask angle alignment procedures (i.e., wedge compensation) are not guaranteed to work in small brittle samples. This may cause unnecessary damage both to the sample and to the chromium layer of the photomask. For these reasons, it is desirable to design special tools and adapters for small samples.

Deep sputter etching using a photoresist mask also carries the risk of extreme mask reticulation [26], which leads to a rapid increase of the roughness, delamination and bubble formation in the resist layer. Photolithographically defined features are in this way destroyed before the desired etch depth has been reached. While most photoresists are susceptible to reticulation, this phenomenon can be overcome through hard mask processing.

Finally, sputter etching in KY(WO$_4$)$_2$ causes redeposition. Many techniques including rounded masks, thin hard masks, chemical etching, and angled etching can be used to avoid or minimize redeposition [27]. However, these techniques often come at the cost of reduced resolution and increased roughness. One method that has not been shown in KY(WO$_4$)$_2$ before is to remove the redeposition after dry etching of the waveguides, using a wet etch process step. In this paper, we report the development of sample handling tools to eliminate both the edge bead during spinning and the damage to the samples during UV contact lithography. We also describe in detail the implementation of a hard mask process for deep reactive ion etching and a method to strip redeposition. The combination of these developments facilitates the fabrication of high refractive index contrast waveguides in KY(WO$_4$)$_2$ while increasing the yield of the process.

3.2   Overview of complete process flow

The complete process flow proposed in this work for the fabrication of high refractive index contrast waveguides in KY(WO$_4$)$_2$ is shown in Figure 3.1. The main innovations introduced by this work are shown in steps c-g and in j. Steps c-f show our approach to the spin coating process using thick photoresist on small samples, in this case 1 cm^2, with minimal edge bead. Step g shows a tool used during the exposure step to reduce risk of sample cracking during UV contact lithography. Furthermore, redeposited material from the ICP-RIE process is removed from the sidewalls of the feature using a selective wet etch (j). The KY(WO$_4$)$_2$ samples used in this work are purchased from Altechna. They have a size of 10 mm × 10 mm × 1 mm and are cut in the *a-c* plane. In

the following sections, the different steps of the described process flow are detailed.
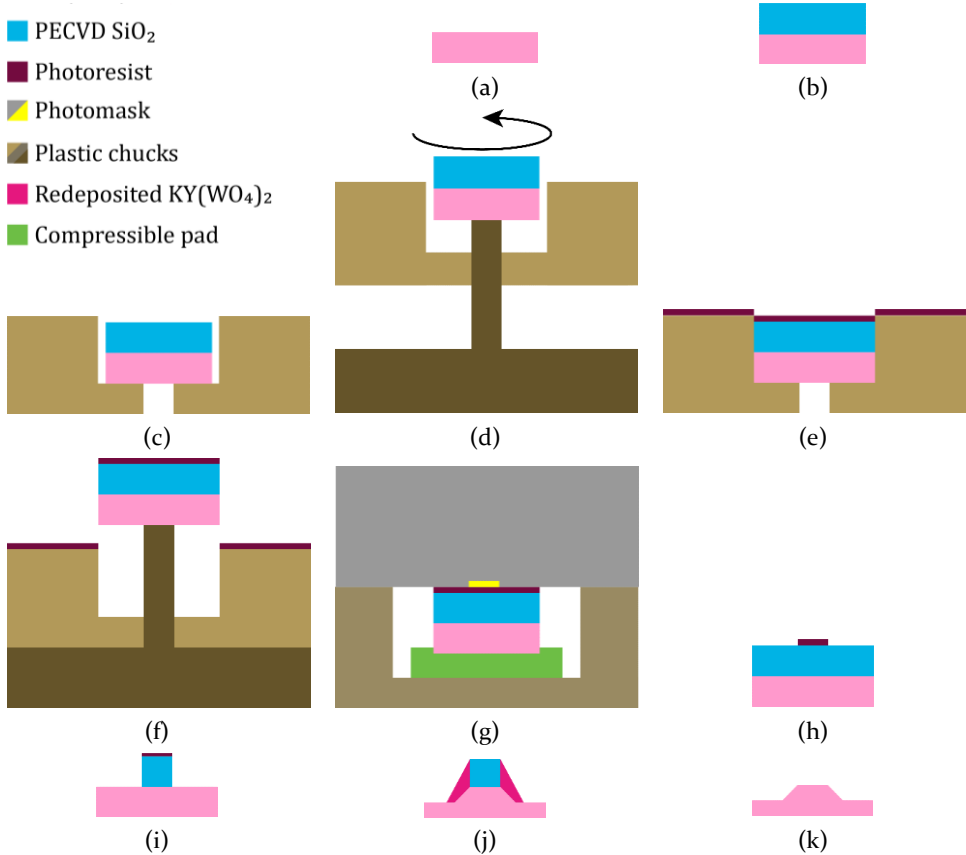
Figure 3.1: Complete process flow for sample fabrication. (a) Initial KY(WO$_4$)$_2$ sample. (b) PECVD deposition of SiO$_2$ hard mask layer. (c) Mounting of sample in spin coating chuck. (d) The base tool is used to lift the sample and rotate it into corner contact with the chuck edges. (e) Edge bead-reduced spin coating of photoresist. (f) Retrieval of sample from the spin coating chuck using the base tool. (g) Photolithography exposure using custom mount. (h) Development of photoresist. (i) ICP-RIE etch to open SiO$_2$ hard mask. (j) Ar-based ICP-RIE etch to pattern KY(WO$_4$)$_2$. (k) Redeposition stripping using 20% HCl at 80°C and mask removal in HF.

3.3 Edge bead removal

Resist edge bead is a well-known problem in spin coating. During spinning, resist forms a thicker ridge on the edge of the wafer [25] called edge bead. The presence of the edge bead can cause flaking, poor photomask contact, photomask contamination in case of insufficient drying, and a reduction of useful processing area in the sample. Edge bead issues are worse when using

viscous, thick resists, which is necessary for deep etching. Furthermore, the problem is further enhanced when using small samples, as a large proportion of the sample is close to the edge.

In the processing of full wafers, edge bead removal is typically performed using spray nozzles dispensing solvents on the backside or edge of the wafer. On small, square samples such a procedure is not an option. While it is possible to remove the edge bead manually using a swab dipped in a solvent, this processing step is not reproducible and introduces additional solvents and potential contamination to the surface of the sample.

In this work, a special spin-coating chuck was designed, shown in Figure 3.2. The chuck consists of a circular disk 6 cm in diameter, Figure 3.2 (a-b, d-e), which matches an existing chuck that is firmly mounted on the spin coater utilized in this work (i.e., custom-made spin coater in the MESA+ Nanolab). The custom chuck can be placed and removed from the existing chuck in the same way as a regular wafer and is held in place by vacuum. A square blind hole of size 11 mm × 11 mm and 1.1 mm in depth has been milled in the center of the custom chuck, designed to fit the 10 mm × 10 mm × 1 mm $KY(WO_4)_2$ sample. The blind corners have a radius of 400 μm due to the round milling tool. A circular hole of diameter 6 mm was milled in the center of the blind. This hole provides contact with the vacuum lines, which protects the $KY(WO_4)_2$ sample from being disturbed by centrifugal forces.
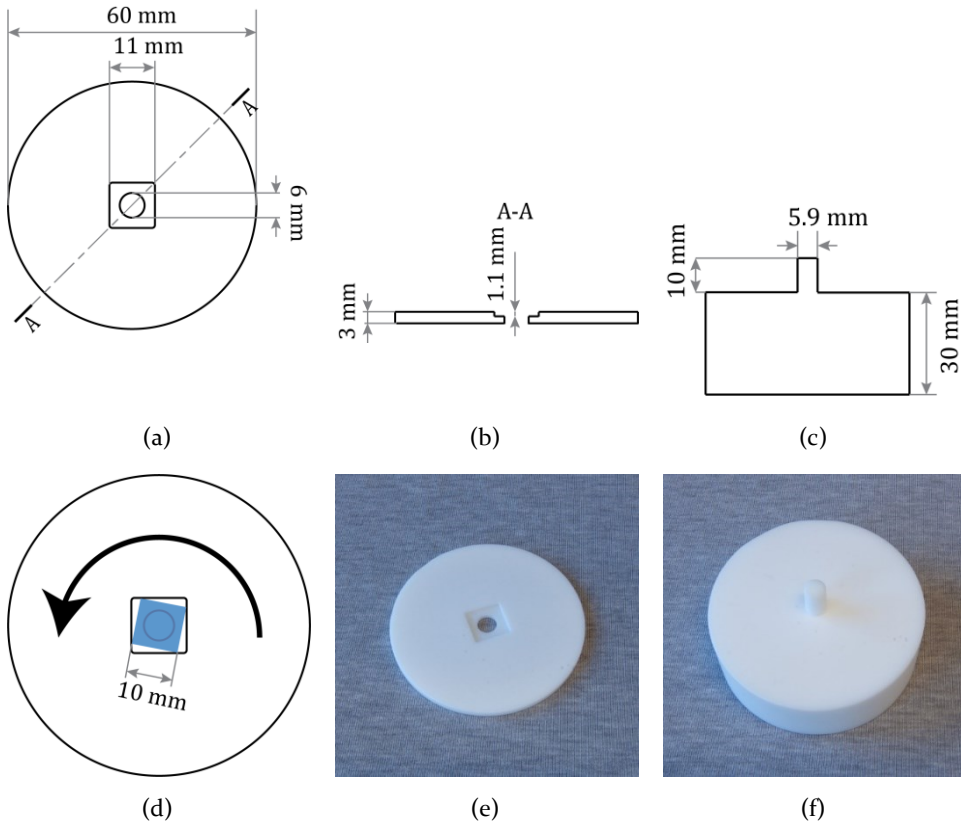
Figure 3.2: Technical drawing of the chuck used for edge bead-reduced spin coating. (a) Top view of the chuck. (b) Cross-section through line A-A in (a), showing the thickness of the chuck and depth of the recess. (c) Cross-section of the base plate. (d) Schematic of the chuck with the sample mounted, with the direction of rotation indicated. (e-f) Photographs of the spin coating chuck (e) and sample removal tool (f).

A base tool was also designed, which consists of a thick base with a 10 mm long protruding pillar with a diameter of 5.9 mm (c, f). This tool is used during the mounting and dismounting of the sample.

The sample is mounted in the chuck in a 3-step process, shown in Figure 3.1 (c-d): First the sample is placed in the center of the blind with tweezers (Figure 3.1 (c)). Second the chuck is lowered slightly onto the base plate, such that the sample is raised without leaving the blind (Figure 3.1 (d)). The chuck is then rotated counterclockwise, which brings the corners of the sample into contact with the edges of the blind, shown in Figure 3.2 (d). It is very important to ensure a good contact of the sample with the spinning chuck so that the photoresist, forced to the corners by centrifugal forces, gets

transferred from the sample to the chuck thereby minimizing edge bead formation. After spinning, the chuck is lowered onto the base plate (Figure 3.1 (f)) in order to raise the sample, which can then easily be picked up from the tool.

3.3.1 Characterization of the performance

Four $KY(WO_4)_2$ samples were spin coated with Olin OiR 908-35 photoresist at a spin speed of 2000 rpm for 60 s, for a thickness of 5 µm. Before resist spinning, the samples were cleaned for 10 minutes in 99% HNO_3, dehydration baked at 120°C for 5 minutes and spin coated with HMDS at 4000 rpm. First, a regular spin coating chuck (chuck 1) with a small vacuum hole was used. Afterward, the procedure was repeated using the custom spin coating chuck described in this paper (chuck 2).

After spin coating, the samples were soft baked at a temperature of 90 °C for 2 minutes. Comparison of the samples was performed using optical microscopy. Images were taken of all 4 corners of the samples, and the length of the edge bead along the edges and corners was measured. Profilometry to measure the height was considered, but not performed due to the risk of equipment damage near the sample edges, as well as high risk of contaminating the probe with insufficiently dried photoresist.

3.3.2 Results of edge bead removal

The results are summarized in Table 3.1. It was found that chuck 1 produced samples with an edge bead with a width of 396 µm ± 42 µm, and corner width of 1181 µm ± 40 µm. 72% of the corners overhang outside the sample edge, and the smallest corner was 988 µm wide.

In contrast, chuck 2 produced statistically significantly smaller amounts of edge bead in the corners, at a significance level $p = 0.05$. The width of the corner bead showed a very large uncertainly of 269 µm. This is the result of a bimodal distribution of corner widths, where 47% of the corners are larger than 1000 µm, and the remainder are smaller than 700 µm. This is mostly caused by the samples not being diced perfectly square and, therefore, not having all the corners in contact with the chuck. Only the corners that were in contact with the chuck exhibited the desired reduction in edge bead. These problems may be ameliorated by a chuck design with one or more movable edges. The resist along the edges was not significantly reduced.

The full potential of the technique is shown in the row "Chuck 2 filtered" of Table 3.1, where only the corners that were in contact with the chuck were considered for the analysis. These data points show a 22% smaller width of the edge bead than obtained when using chuck 1 and 57% narrower corners, not accounting for uncertainty. It can also be clearly observed in Figure 3.1 that the overhang visible when using the original chuck disappears with the improved chuck.

Further improvements to the chuck are possible: Resist stains on the bottom of the sample were observed, resulting from an imperfect vacuum seal. The addition of gutters to guide the leftover resist to the disk edge will reduce backside contamination and decrease the edge bead further.

Table 3.1. Summary of the edge bead measurements, showing the edge bead width, corner bead width, percentage of corner beads overhanging the chip corner and percentage of corner beads larger than 1 mm. Edge and corner lengths are given as the average and 95% error bound calculated using a Student's T distribution. Four samples were used to test each of the chucks.

	Edge [μm]	Corner [μm]	Overhang [%]	>1 mm [%]
Chuck 1	396 ± 42	1181 ± 40	72	95
Chuck 2	339 ± 30	925 ± 269	18	47
Chuck 2 filtered	310 ± 34	508 ± 82	14	0

(a)   (b)
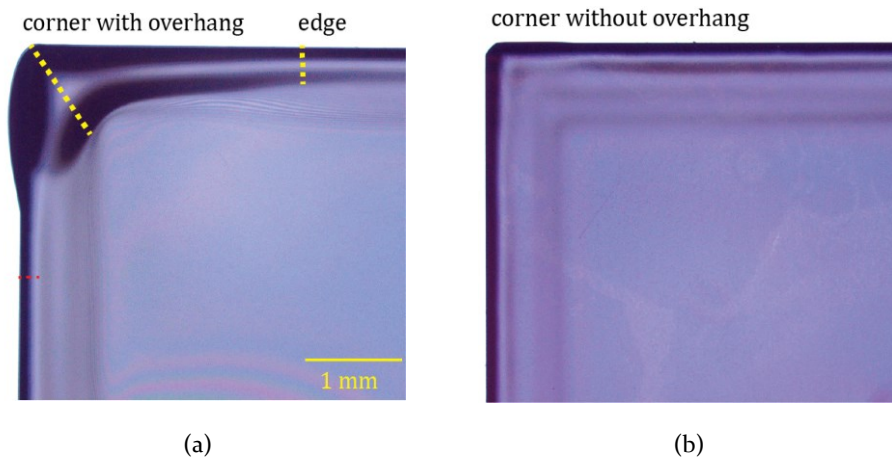
Figure 3.3: Samples spin coated with OiR 908-35 resist at 2000 rpm for a target thickness of 5 μm. (a) Using a conventional chuck. A thick edge bead region is clearly visible. The measurements have been made along the red dashed lines. (b) Using the custom chuck. The edge bead is visibly reduced. The corner shown was in contact with the spinning chuck.

3.4 Photolithography of small samples

The EV620 contact mask aligner used in this work is designed to work with 4-inch wafers. The mask alignment process is therefore not optimal for small samples. The mask contact step (i.e., wedge correction) carries the risk of crushing the sample. In this step, the mask may be brought down at an angle relative to the $KY(WO_4)_2$ surface, which concentrates the force on an edge or corner of the brittle $KY(WO_4)_2$ sample and may cause damage to both the sample and the mask. In the past, this was palliated by using cleanroom tissue as a compressive base together with surrounding the sample with glass pieces of matched thickness [28].

In this work, a sample mount is designed and manufactured, as shown schematically in Figure 3.4 (a-b) and photographed in (c). The mount consists of a 3 mm thick square of width and length 50 mm × 50 mm, with a 1.9 mm deep blind hole of 30 mm × 30 mm in the middle. The mount is made from PEEK plastic due to its good properties for high-precision machining.

A pad of compressible material is placed inside the blind. In this work, 3 pieces of cleanroom tissue have been used. The $KY(WO_4)_2$ sample is placed on top of the pad and the complete assembly is aligned to the mask by eye before mask contact is made. During contact, the $KY(WO_4)_2$ sample is gently pressed into the cleanroom tissue until flush with the top of the holder. The mask then rests on the large PEEK mount, which helps provide uniform pressure over the small $KY(WO_4)_2$ piece, especially when exposing dice far from the mask center. Although a quantitative analysis is challenging, we report that sample chipping has no longer been observed after this technique was implemented.
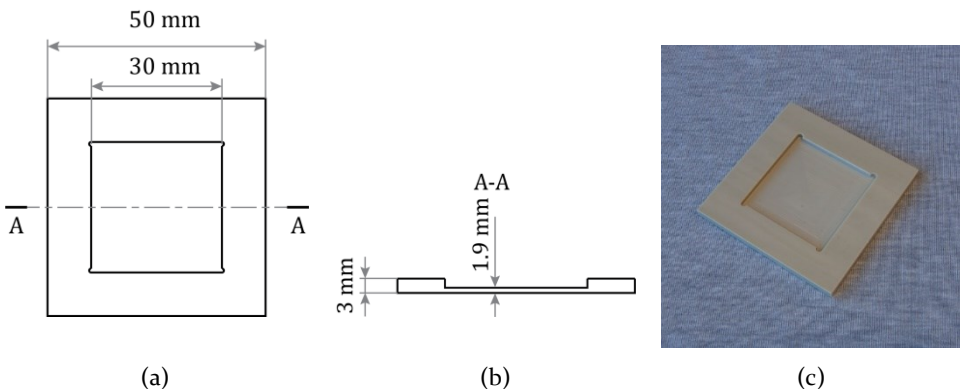
Figure 3.4: Technical drawing of the lithography sample mount. (a) Top-down view. (b) Cross-section through line A-A in (a), showing the geometry of the center of the mount.

3.5 Deep reactive ion etching

In inductively coupled plasma reactive ion etching (ICP-RIE), the general scheme is to ionize a gas and let reactive species chemically etch the sample in combination with physical sputtering. For materials like silicon and silicon oxide, ICP-RIE permits complex physical/chemical schemes with a wide parameter space to be used to tune the properties of the etched features [25,29–31]. However, as $KY(WO_4)_2$ is highly inert, this is not a viable option. The only volatile compound that is formed when using chlorine or fluorine chemistries is WF_6, with an atmospheric pressure boiling point of 17.1°C [32]. While an Ar/SF_6 gas mixture has been reported for sample thinning [33], we have found that the inclusion of SF_6 at concentrations of ~10% reduces the selectivity with respect to photoresist from 2.6 to 0.3. For this reason, we have opted to use in this work a purely argon based etch, based entirely on sputtering and without chemical etch mechanisms.

One challenge of deep Ar etching is reticulation of the thick photoresist layer [26]. It is commonly observed that when the resist is etched for a long time using argon, surface cracking, bubbling and chemical hardening can occur. Such defects cause severe roughness, as well as craters in the sample where the resist has cracked, and they make resist removal challenging. An example is shown in Figure 3.5, where a disk of 120 µm in diameter in 3.5 µm thick Olin OiR 908-35 photoresist was subjected to 30 minutes of argon plasma etching. Furthermore, the hardened resist may be challenging to remove using oxygen ashing or stripping in HNO_3. While it may be assumed that hard baking or UV curing, which are known to increase the chemical resistance of photoresist [34] would diminish the risk of reticulation, we have observed the opposite effect in our experiments. Therefore, such hardening processes are not recommended for Ar etching.
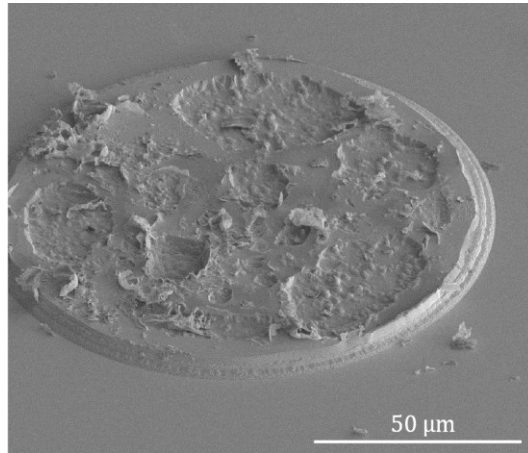
Figure 3.5: Severe reticulation of 3.5 μm thick Olin OiR 908-35 photoresist used to pattern a 120 μm large disk.

To circumvent the issue of resist reticulation, hard masks such as SiO_2, other oxides, or metals can be used, sometimes in combination with reactive species [27]. Some of the materials known to sputter slowly in Ar include photoresists, SiO_2, amorphous carbon and Al_2O_3 [35,36], which makes them candidates for use as hard masks. Chromium has also been used as a hard mask for $KY(WO_4)_2$ in a process incorporating SF_6 [37], although this carries the risk of high optical losses due to metal contamination.

Some processes from this group and others using various mask materials are listed in Table 3.2. Further processes with SU-8 resists and SiO_2 from the same experimenters have been reported. However, they are not documented here due to missing information on selectivity and performance. Geskus [38] and Sefünç [39] both reported high sidewall roughness in their respective processes, especially for deep etching, while Medina [37] did not comment on it.

Amorphous carbon offers extremely high selectivity, however it is very fragile and requires PECVD SiO_2 adhesion and capping layers for protection. To avoid damaging the carbon layer during wet cleaning, it must be patterned using the SiO_2 as a hard mask, which itself must be patterned using a second hard mask. This leads to a total of four depositions and four dry etching steps, with each carrying a risk of roughness transfer or damage.

Table 3.2: Overview of ICP-RIE etching processes used here and in previous works, using OiR series photoresists and various hard mask materials. ICP and RF power are given in in W, pressure in mTorr and etch rate in nm/minute.

	Martinussen et al			Sefünç [39]	Geskus [38]	Medina [37]
Machine	Oxford PlasmaPro 100 Cobra			Adixen AMS 100 DE	Oxford Plasmalab 100	Oxford PlasmaPro NGP80
Mask	OiR	SiO_2	C [40]	OiR	Al_2O_3	Cr
ICP power	1875	1875	1875	1500	1500	350
RF power	150	150	150	150	150	210
Ar %	100%	100%	100%	100%	100%	50%
SF6 %	-	-	-	-	-	50%
Pressure	3	3	3	3.75	19	12
Etch rate	100	100	100	65	84	73
Selectivity	2.6	1.2	8.2	1.2	2.7	5

3.5.1 Etching procedure

A hard mask consisting of 5 μm thick SiO_2 deposited by plasma enhanced chemical vapor deposition (PECVD) was utilized in this work. The SiO_2 was patterned using Olin OiR 907-17 photoresist. The resist was spin coated at 4000 rpm, for a thickness of 1.7 μm. After contact photolithography using an EV620 mask aligner with a broadband source and the lithography tools described previously, the SiO_2 hard mask layer was etched in an Adixen AMS 100 DE ICP-RIE. The etching parameters are ICP power 2800 W, CCP RF power 350 W, C_4F_8 flow 20 sccm, CH_4 flow 15 sccm, He flow 150 sccm, chamber pressure 6.4 mTorr, and table temperature -10 °C. This process has a selectivity of 5, which allows for a thinner photoresist layer than those mentioned previously in this work.

The $KY(WO_4)_2$ etching was performed in an Oxford PlasmaPro 100 Cobra. The etching parameters are ICP power 1875 W, RF CCP power 150 W, pressure 3 mTorr, Ar flow 90 sccm, and table temperature 10 °C. Using this recipe, a

selectivity of 2.6 for $KY(WO_4)_2$ with respect to photoresist and 1.2 for $KY(WO_4)_2$ with respect to SiO_2 was obtained. The $KY(WO_4)_2$ etch rate is 100 nm/minute.

The etching was performed for 32 minutes. After etching, any residual photoresist was removed using a TePla 300 O_2 microwave asher. The structures were imaged using an FEI Nova FIB/SEM.

3.5.2 Results of etching

The resulting structure using a SiO_2 hard mask and the etching recipe discussed above is shown in Figure 3.6 (a-b). The etch depth is 3.1 µm. The sidewall angle is 78°, while the measured angle of the structure within the redeposition is 61°.

Figure 3.6 (c) shows a focused ion beam (FIB) cross-section of a larger structure etched almost to the point of completely removing the mask. The total etch depth is now 6.5 µm. The observed pentagonal structure results from SiO_2 mask retraction because the mask etches more rapidly near the corners. At a given point during prolonged etching, the SiO_2 mask is completely etched through at the edges of the patterns. Further etching at this point is possible, although a second slope appears as a result of transfer of the mask profile at the surface of the feature.

Furthermore, the reduced steepness of the sidewall decreases the amount of residual redeposition because of the higher received ion flux by the sidewall at that angle. The outer sidewall angle is now 67°, and the surface top has a 21° angle.

3.6 Redeposition-free structures in $KY(WO_4)_2$

Redeposition is easily avoided when etching materials such as Si and SiO_2 by using ICP-RIE with fluorinated compounds like CHF_3 and SF_6, as the reactive F^- species form volatile compounds that are pumped away in gas phase [29]. When using only inert argon gas in ICP-RIE, however, the etching mechanism is purely physical and redeposition becomes a problem.

The three main strategies for masking prior to reactive ion etching are (i) conventional rectangular masks, (ii) rounded masks and (iii) very thin hard masks [27]. However, all three approaches have advantages and disadvantages. A standard rectangular mask increases the amount of redeposition because the tall mask presents a large area for sputtered atoms to hit. This is clearly

visible in Figure 3.6 (a). Also, the ion flux (i.e., the number of ions incident on the sidewalls) is low because the sidewall angle is steep, preventing efficient etching of the redeposition, which can build up over time. In ion beam etching (IBE), the standard solution is tilting and rotating the sample, which provides a more uniform ion flux. This is however not possible in ICP-RIE systems.

The second approach, the use of rounded masks, helps reducing the redeposition by presenting an angled sidewall. The ion flux at the slanted sidewall is higher because it is no longer parallel to the ion direction. The redeposition on the slanted sidewalls is therefore etched more rapidly, ideally to the point of total removal. A rounded mask is typically prepared by heating the resist to a temperature close to but below its melting point, so that it reflows. However, broadening of the resist patterns due to the reflow process causes a tradeoff in resolution. In addition, since the resist mask is thinner close to the edge, a deep etch will induce significant mask erosion leading to rough, severely sloped sidewalls [39].

The third option is a thin hard mask. A thin mask does not provide a large wall for the redeposition to stick to preventing the formation of the structures shown in Figure 3.6 (a). The material utilized as hard mask should exhibit a significantly lower etch rate than the sample to be etched. Alternatively, the etch rate of the mask material should be considerably reduced by the addition of a chemical component into the gas mixture [27]. Past experiments have identified amorphous carbon as a candidate as thin hard mask material [40]. However, amorphous carbon is a very challenging material to work with due to fragility, low growth rate and poor adhesion. Furthermore, simulations in Synopsys OptoDesigner Process Flow have shown that although redeposition does not protrude vertically above the mask, the sidewalls remain sloped.

In this work we present a novel fourth approach, which consists of a chemical cleaning step following the ICP-RIE dry etch with a square mask. Even though $KY(WO_4)_2$ is a chemically inert material, there are references to chemical reactions occurring at elevated temperatures [41]:

$$KY(WO_4)_2 + 4\,HCl \xrightarrow{100\,°C} KCl + YCl_3 + 2WO_3 + 2\,H_2O \qquad (3.1)$$
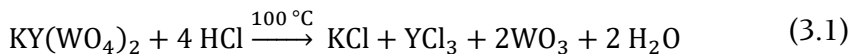
In previous work, this reaction has been used to selectively underetch amorphized $KY(WO_4)_2$ [20], followed by a TMAH etch to remove the insoluble by-product WO_3. Here, the procedure is performed using a concentration of 20% HCl and a temperature of 80°C for 15 minutes to remove the redeposition attached to the sidewalls of the deeply etched $KY(WO_4)_2$ structures. The concentration and temperature were designed to minimize the risk of harmful HCl fumes while maximizing effectiveness.

To evaluate the etch rate of crystalline $KY(WO_4)_2$ in a 20% HCl solution at 80°C, a $KY(WO_4)_2$ sample with a patterned PECVD SiO_2 mask was immersed in the acid solution for 2 hours. The resulting step height after wet etching was measured to be 120 nm ± 5 nm, yielding an etch rate of 1 nm/minute. This rate is low enough that the acid can safely be used on $KY(WO_4)_2$ structures. However, the roughness of the surface of the $KY(WO_4)_2$ increases from < 1 nm to ±5 nm. To prevent this increase in roughness, the SiO_2 mask should not be removed prior to redeposition stripping.

3.6.1 Results of redeposition removal

Figure 3.6 (a) and (b) show a 3.1 μm deep etched structure immediately after dry etching (a) and after the stripping of the redeposition by the proposed wet etching step (b). The redeposition produced by dry etching is significant, extending upward as high as the residual hard mask and up to 1 μm laterally. The lateral growth of the redeposition increases the effective width of the mask during the etching process, decreasing the angle of the $KY(WO_4)_2$ sidewall to ~61°. In contrast, the sidewall of the redeposition is more vertical at 78°. In (b), the redeposition has been removed using the proposed wet etching step, with the structure showing a distinctly pyramidal shape, with smooth sidewalls.
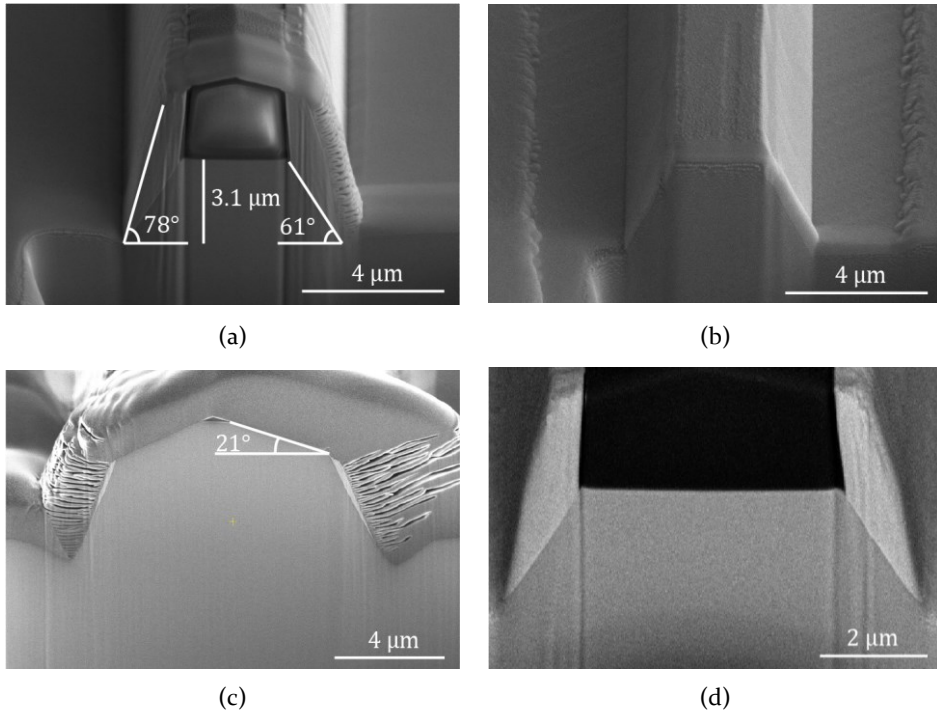
Figure 3.6: FIB cross-sections of etched structures at various points during the processing. (a) A KY(WO$_4$)$_2$ immediately after dry etching. Significant redeposited ears extend above the structure, to the total height of the remaining SiO$_2$ mask. The horizontal width of the redeposited material is 1 μm. A FIB deposited Pt layer covers the cross-section to reduce geometric SEM artifacts and rounding during cross-sectioning. A sidewall angle of ~61° was measured for the KY(WO$_4$)$_2$ sidewall while the outer redeposition exhibits an angle of 78°. (b) A similar structure from the same batch after HCl etching and HF SiO$_2$ hard mask stripping (c) SEM image of a similar structure, etched to a depth of 6.5 μm. The SiO$_2$ hard mask was completely consumed, which led to the second angle (21°) on the upper part of the sidewall. A thicker Pt layer has been used during the cross-sectioning. (d) FIB cross-section of a structure with significant redeposition imaged only using backscattered electrons. The redeposited material appears bright, indicating a higher concentration of heavy ions. In contrast, the SiO$_2$ mask, which is composed of light atoms, appears very dark.

Figure 3.6 (d) shows a similar structure, imaged with an Everhart-Thornley detector with a negative bias voltage. This configuration repels secondary electrons and detects only backscattered electrons. The backscattered electron yield is strongly dependent on elemental composition, with heavier atoms having a higher yield and appearing brighter [42,43]. The redeposition is much brighter than the crystalline KY(WO$_4$)$_2$. This indicates that it is not

simply an amorphous phase of $KY(WO_4)_2$, but rather a stoichiometrically different compound.

It is also known that heavier atoms sputter omnidirectionally, while lighter elements to a greater extent sputter normal to the surface of the sample [44]. Oxygen, potassium, yttrium and tungsten have atomic numbers 8, 19, 39 and 74. It is therefore likely that the redeposition is rich in metals, especially tungsten, as these would have been sputtered onto the features of the sidewalls and appear brighter.

The exact composition of the redeposited material is not known. Techniques like EDX and XPS may be used, however the redeposited structures are very small. It is therefore challenging to get high quantitative accuracy without measuring the substrate. The etching mechanism is also not known. The etching of $KY(WO_4)_2$ relies on dissolving the salt into its constituent complex ions, and this is not transferable to HCl reacting with a partially oxidized alloy.

Figure 3.7 shows redeposition peeling away after ultrasound cleaning (a) and after a 5 minute long etch step (b), which is insufficient time for complete removal. This poses the question of whether the removal mechanism is etching or peeling away from the $KY(WO_4)_2$ sidewalls following intrusion by the etchant. Such intrusion may happen from the bottom, where argon ion bombardment may have amorphized a thin $KY(WO_4)_2$ layer and made it susceptible to etching.

However, Figure 3.7 (c) shows the cross-section of a structure with significant redeposition, covered with a thick layer of FIB-deposited platinum. Figure 3.7 (d) shows the same cross-section after the same incomplete etching step that produced the structure in (b). The redeposition is clearly reduced, with complete removal on the right and only a thin sliver remaining on the left. This demonstrates that redeposited material is eroded by the etch, and does not simply delaminate and float away in one piece. The stripping mechanism is therefore likely a combination of delamination and etching.
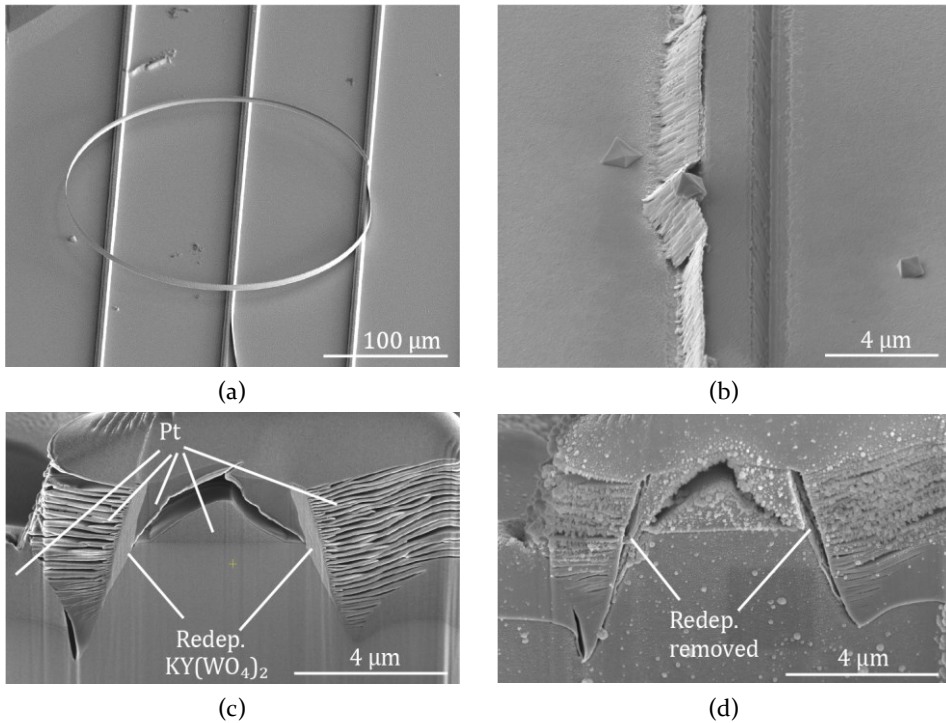
Figure 3.7: (a) A strip of sidewall redeposition that has delaminated during ultrasound cleaning and curled up due to internal shear stresses. (b) Sidewall redeposition that has been partially removed during an insufficiently long HCl etching step. (c) Cross-section of a structure with significant redeposition, covered with a thick layer of platinum. (d) The same cross-section after a 5 minute HCl etching step. Most of the redeposited material is removed.

Figure 3.8 shows an example of the highest achieved resolution deep etched structure with smooth sidewalls. The width at the top is 1.4 μm and the depth is 3.1 μm, with an angle of 67°. As has been shown previously, deeper structures are achievable. However, the risk of sidewall roughness due to cumulative micromasking increases over time. Narrower structures may also be made, however the main contribution to feature size is the sidewall slope.

<table>
<tr><td>(a)</td><td>(b)</td></tr>
</table>
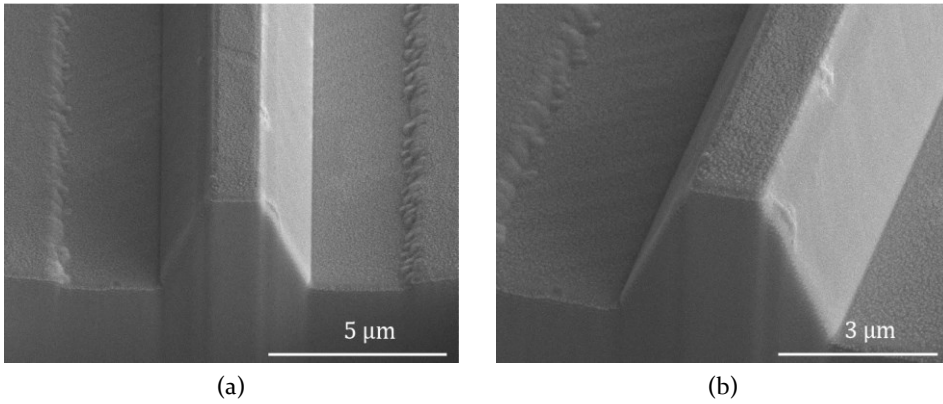
Figure 3.8: Ridge structures after redeposition stripping. The feature width at the top is 1.4 μm, the etch depth is 3.1 μm, the width at the bottom is 4.2 μm and the sidewall angle is 67°. (a) Normal view. (b) 15° rotated view of the same structure, showing low sidewall roughness.

3.7 Conclusion

Several techniques have been introduced that minimize or eliminate common challenges in $KY(WO_4)_2$ fabrication for high aspect ratio structures. Together, these techniques improve the performance and yield of the $KY(WO_4)_2$ lithography and etching process. The useful processing area of small samples has been increased through edge bead reduction. The yield of the UV contact lithography process step has been increased to 100%. A deep etching procedure has been developed, which in combination with a technique for removing redeposition has been demonstrated to produce deep (3.1 μm) $KY(WO_4)_2$ structures with clean smooth sidewalls with an angle of 67°. Very deep (6.5 μm) features with a pentagonal structure due to full consumption of the SiO_2 hard mask have also been demonstrated. The microfabrication processes described here are directly applicable to existing $KY(WO_4)_2$ processes such as thin layer lapping and polishing or ion irradiation to fabricate high refractive index contrast waveguides and other devices. The techniques may also be applicable to other hard-to-process materials.

Bibliography

1. J. A. Piper and H. M. Pask, "Crystalline Raman Lasers," IEEE J. Sel. Top. Quantum Electron. **13**(3), 692–704 (2007).
2. Y.-S. Yong, S. Aravazhi, S. A. Vázquez-Córdova, J. J. Carvajal, F. Díaz, J. L. Herek, S. M. Garcia-Blanco, and M. Pollnau, "Direct confocal lifetime measurements on rare-earth-doped media exhibiting radiation trapping," Opt. Mater. Express **7**(2), 527–532 (2017).
3. A. A. Kovalyov, V. V. Preobrazhenskii, M. A. Putyato, O. P. Pchelyakov, N. N. Rubtsova, B. R. Semyagin, V. E. Kisel', S. V. Kuril'chik, and N. V. Kuleshov, "115 fs pulses from Yb^{3+}:$KY(WO_4)_2$ laser with low loss nanostructured saturable absorber," Laser Phys. Lett. **8**(6), 431–435 (2011).
4. F. Brunner, G. J. Spühler, J. A. Au, L. Krainer, F. Morier-Genoud, R. Paschotta, N. Lichtenstein, S. Weiss, C. Harder, A. A. Lagatsky, A. Abdolvand, N. V. Kuleshov, and U. Keller, "Diode-pumped femtosecond Yb:$KGd(WO_4)_2$ laser with 1.1-W average power," Opt. Lett. **25**(15), 1119–1121 (2000).
5. U. Griebner, S. Rivier, V. Petrov, M. Zorn, G. Erbert, M. Weyers, X. Mateos, M. Aguiló, J. Massons, and F. Díaz, "Passively mode-locked Yb:$KLu(WO_4)_2$ oscillators," Opt. Express **13**(9), 3465–3470 (2005).
6. E. Kifle, X. Mateos, J. R. V. de Aldana, A. Ródenas, P. Loiko, S. Y. Choi, F. Rotermund, U. Griebner, V. Petrov, M. Aguiló, and F. Díaz, "Femtosecond-laser-written Tm:$KLu(WO_4)_2$ waveguide lasers," Opt. Lett. **42**(6), 1169–1172 (2017).
7. K. van Dalfsen, S. Aravazhi, C. Grivas, S. M. Garcia-Blanco, and M. Pollnau, "Thulium channel waveguide laser with 1.6 W of output power and ~80% slope efficiency," Opt. Lett. **39**(15), 4380–4383 (2014).
8. A. A. Kaminskii, P. V. Klevtsov, L. Li, and A. A. Pavlyuk, "Stimulated emission from $KY(WO_4)_2$: Nd^{3+} crystal laser," Phys. Status Solidi A **5**(2), K79–K81 (1971).
9. Z. Cong, Z. Liu, Z. Qin, X. Zhang, H. Zhang, J. Li, H. Yu, and W. Wang, "LD-pumped actively Q-switched Nd:$KLu(WO_4)_2$ self-Raman laser at 1185 nm," Opt. Laser Technol. **73**, 50–53 (2015).
10. V. Petrov, M. C. Pujol, X. Mateos, Ò. Silvestre, S. Rivier, M. Aguiló, R. M. Solé, J. Liu, U. Griebner, and F. Díaz, "Growth and properties of $KLu(WO_4)_2$, and novel ytterbium and thulium lasers based on this monoclinic crystalline host," Laser Photonics Rev. **1**(2), 179–212 (2007).
11. D. Geskus, S. Aravazhi, S. M. Garcia-Blanco, and M. Pollnau, "Giant optical gain in a rare-earth-ion-doped microstructure," Adv. Opt. Mater. **24**(10), OP19-22 (2012).

12. S. A. Vázquez-Córdova, S. Aravazhi, C. Grivas, Y.-S. Yong, S. M. Garcia-Blanco, J. L. Herek, and M. Pollnau, "High optical gain in erbium-doped potassium double tungstate channel waveguide amplifiers," Opt. Express **26**(5), 6260–6266 (2018).

13. D. Geskus, S. Aravazhi, K. Wörhoff, and M. Pollnau, "High-power, broadly tunable, and low-quantum-defect $KGd_{1-x}Lu_x(WO_4)_2:Yb^{3+}$ channel waveguide lasers," Opt. Express **18**(25), 26107–26112 (2010).

14. S. Aravazhi, D. Geskus, K. van Dalfsen, S. A. Vázquez-Córdova, C. Grivas, U. Griebner, S. M. Garcia-Blanco, and M. Pollnau, "Engineering lattice matching, doping level, and optical properties of $KY(WO_4)_2$:Gd, Lu, Yb layers for a cladding-side-pumped channel waveguide laser," Appl. Phys. B **111**(3), 433–446 (2013).

15. D. Geskus, S. Aravazhi, C. Grivas, K. Wörhoff, and M. Pollnau, "Microstructured $KY(WO_4)_2:Gd^{3+}$, Lu^{3+}, Yb^{3+} channel waveguide laser," Opt. Express **18**(9), 8853 (2010).

16. D. Geskus, S. Aravazhi, E. Bernhardi, C. Grivas, S. Harkema, K. Hametner, D. Günther, K. Wörhoff, and M. Pollnau, "Low-threshold, highly efficient Gd^{3+}, Lu^{3+} co-doped $KY(WO_4)_2:Yb^{3+}$ planar waveguide lasers," Laser Phys. Lett. **6**(11), 800–805 (2009).

17. K. van Dalfsen, S. Aravazhi, D. Geskus, K. Wörhoff, and M. Pollnau, "Efficient $KY_{1-x-y}Gd_xLu_y(WO_4)_2:Tm^{3+}$ channel waveguide lasers," Opt. Express **19**(6), 5277–5282 (2011).

18. D. Geskus, E. H. Bernhardi, K. van Dalfsen, S. Aravazhi, and M. Pollnau, "Highly efficient Yb^{3+}-doped channel waveguide laser at 981 nm," Opt. Express **21**(11), 13773–13778 (2013).

19. K. van Dalfsen, S. Aravazhi, C. Grivas, S. M. García-Blanco, and M. Pollnau, "Thulium channel waveguide laser in a monoclinic double tungstate with 70% slope efficiency," Opt. Lett. **37**(5), 887–889 (2012).

20. S. M. Martinussen, R. N. Frentrop, M. Dijkstra, F. Segerink, V. Tormo-Márquez, J. Olivares, and S. M. Garcia-Blanco, "Pedestal microdisks in potassium yttrium double tungstate," Opt. Mater. Express **9**(8), 3371–3378 (2019).

21. R. Frentrop, R. Frentrop, I. Subbotin, F. Segerink, R. Keim, V. Tormo-Marquez, J. Olivares, J. Olivares, K. Shcherbachev, S. Yakunin, I. Makhotkin, S. M. Garcia-Blanco, and S. M. Garcia-Blanco, "In-depth structural analysis of swift heavy ion irradiation in $KY(WO_4)_2$ for the fabrication of planar optical waveguides," Opt. Mater. Express **9**(12), 4796–4810 (2019).

22. C. I. van Emmerik, R. Kooijman, M. Dijkstra, and S. M. Garcia-Blanco, "Lapping and Polishing of Crystalline $KY(WO_4)_2$: Toward High Refractive Index Contrast Slab Waveguides," Micromachines **10**(10), 674 (2019).

23. C. I. van Emmerik, R. Frentrop, M. Dijkstra, F. Segerink, R. Kooijman, M. Muneeb, G. Roelkens, E. Ghibaudo, J.-E. Broquin, and S. M. Garcia-Blanco, "Heterogeneous integration of $KY(WO_4)_2$-on-glass: a bonding study," OSA Contin. **2**(6), 2065–2076 (2019).

24. M. A. Sefünç, F. B. Segerink, and S. M. Garcia-Blanco, "High index contrast passive potassium double tungstate waveguides," Opt. Mater. Express **8**(3), 629–638 (2018).

25. M. Quirk and J. Serda, *Semiconductor Manufacturing Technology* (Prentice Hall, 2001).

26. A. R. Pal, R. L. Bruce, F. Weilnboeck, S. Engelmann, T. Lin, M.-S. Kuo, R. Phaneuf, and G. S. Oehrlein, "Real-time studies of surface roughness development and reticulation mechanism of advanced photoresist materials during plasma processing," J. Appl. Phys. **105**(1), 013311 (2009).

27. R. E. Lee, "Microfabrication by ion-beam etching," J. Vac. Sci. Technol. **16**(2), 164–170 (1979).

28. K. van Dalfsen, "High-power, highly-efficient thulium-doped potassium double tungstate channel waveguide lasers," Thesis, University of Twente (2017).

29. R. Legtenberg, H. Jansen, M. de Boer, and M. Elwenspoek, "Anisotropic Reactive Ion Etching of Silicon Using $SF_6/O_2/CHF_3$ Gas Mixtures," J. Electrochem. Soc. **142**(6), 2020–2028 (1995).

30. H. Jansen, M. de Boer, R. Legtenberg, and M. Elwenspoek, "The black silicon method: a universal method for determining the parameter setting of a fluorine-based reactive ion etcher in deep silicon trench etching with profile control," J. Micromechanics Microengineering **5**(2), 115–120 (1995).

31. F. Marty, L. Rousseau, B. Saadany, B. Mercier, O. Français, Y. Mita, and T. Bourouina, "Advanced etching of silicon based on deep reactive ion etching for silicon high aspect ratio microstructures and three-dimensional micro- and nanostructures," Microelectron. J. **36**(7), 673–677 (2005).

32. D. R. Lide, *CRC Handbook of Chemistry and Physics: A Ready-Reference Book of Chemical and Physical Data* (CRC-Press, 1995).

33. M. Medina, C. E. Rüter, M. C. Pujol, D. Kip, J. Masons, A. Ródenas, M. Aguiló, and F. Díaz, "$KLu(WO_4)_2/SiO_2$ Tapered Waveguide Platform for Sensing Applications," Micromachines **10**(7), 454 (2019).

34. G. Sengo, H. A. G. M. van Wolferen, and A. Driessen, "Optimized Deep UV Curing Process for Metal-Free Dry-Etching of Critical Integrated Optical Devices," J. Electrochem. Soc. **158**(10), H1084–H1089 (2011).

35. N. Veisfeld and J. D. Geller, "Ion sputtering yield measurements for submicrometer thin films," J. Vac. Sci. Technol. A **6**(3), 2077–2081 (1988).

36. K. Wasa, I. Kanno, and H. Kotera, *Handbook of Sputtering Technology* (Elsevier, 2012).
37. M. Medina Martinéz, "KREW/SiO$_2$ waveguide platform for optical sensing applications," Universitat Rovira i Virgili (2019).
38. D. Geskus, "Channel waveguide lasers and amplifiers in single-crystalline Ytterbium-doped potassium double tungstates," University of Twente (2011).
39. M. A. Sefünç, T. Alexoudi, Jinfeng Mu, M. Dijkstra, and S. M. García-Blanco, "Fabrication of high-contrast waveguide amplifiers in erbium doped potassium double tungstates," in *2016 18th International Conference on Transparent Optical Networks (ICTON)* (2016), pp. 1–4.
40. S. M. Martinussen, M. Dijkstra, S. M. Garcia-Blanco, and Optical Sciences, "Reducing redeposition on KYW waveguides through hard mask engineering," in *22nd Annual Symposium of the IEEE Photonics Benelux Chapter* (2017).
41. Y. Romanyuk, "Liquid-phase epitaxy of doped KY(WO$_4$)$_2$ layers for waveguide lasers," PhD Thesis, École Polytechnique Fédérale de Lausanne (2005).
42. W. Zhou, R. Apkarian, Z. L. Wang, and D. Joy, "Fundamentals of Scanning Electron Microscopy (SEM)," in *Scanning Microscopy for Nanotechnology: Techniques and Applications*, W. Zhou and Z. L. Wang, eds. (Springer, 2007), pp. 1–40.
43. V. N. E. Robinson, "Imaging with backscattered electrons in a scanning electron microscope," Scanning **3**(1), 15–26 (1980).
44. R. R. Olson, M. E. King, and G. K. Wehner, "Mass effects on angular distribution of sputtered atoms," J. Appl. Phys. **50**(5), 3677–3683 (1979).

CHAPTER 4

Pedestal microdisks in potassium yttrium double tungstate

$KY(WO_4)_2$ is an attractive material for integrated photonics due to its high refractive index and excellent non-linear and gain characteristics. High refractive index contrast structures increase light-matter interaction, reducing the threshold for lasing and non-linear effects. Furthermore, high refractive index contrast permits dispersion engineering for non-linear optics. In this work, we present a novel fabrication method to realize pedestal microdisk resonators in crystalline $KY(WO_4)_2$ material. The fabrication process includes swift heavy ion irradiation of the $KY(WO_4)_2$ with 9 MeV carbon ions and sufficient fluence ($>2.7 \cdot 10^{14}$ ion/cm^2) to create a buried amorphous layer. After annealing at 350° C, microdisks are defined by means of focused ion beam milling. A wet etching step in hydrochloric acid selectively etches the amorphized barrier producing a pedestal structure. The roughness of the bottom surface of the disk is characterized by atomic force microscopy.

4.1 Introduction

Potassium yttrium double tungstate (KY(WO$_4$)$_2$) is a member of the potassium double tungstate family of materials. These include, among others, KY(WO$_4$)$_2$, KYb(WO$_4$)$_2$, KGd(WO$_4$)$_2$ and KLu(WO$_4$)$_2$, which have long been used as bulk laser materials [1–6]. They have several properties that make them very attractive for integrated optics. The refractive index of undoped KY(WO$_4$)$_2$ ranges between 1.96-2.09 for wavelengths extending from 400 nm to 1550 nm [7]. Such high refractive index enables a high index contrast against common materials such as SiO$_2$, water and air. Correspondingly, the non-linear refractive index, n_2, is relatively high at 2.4×10^{-19} m^{2}W^{-1} at a wavelength of 819 nm [8], which is comparable to the non-linear refractive index of Si$_3$N$_4$ at 1550 nm [9] and lower than that of silicon-rich nitride [10]. Furthermore, KY(WO$_4$)$_2$ has a high Raman gain value with sharp peaks at 765 cm^{-1} and 905 cm^{-1} [11], which has been exploited for the realization of Raman lasers [12].

KY(WO$_4$)$_2$, when doped with rare-earth ions, exhibits excellent gain characteristics. Rare earth ions doped into the crystal have high transition cross-sections [13]. Since they are substitutionally placed in a large unit cell, a minimum interionic distance between rare-earth ions of >0.4 nm is guaranteed. This reduces quenching compared with amorphous host materials, permitting heavy doping of the material before detrimental quenching effects appear. High dopant concentration has led to the experimental demonstration of ~800 dB/cm gain in an Yb^{3+} doped layer [13] and ~12 dB/cm in an Er^{3+}-doped waveguide amplifier [14]. Several waveguide lasers operating at different wavelength ranges have been demonstrated in this low refractive index contrast waveguide configuration [15,16].

However, a low refractive index contrast structure does not permit achieving anomalous dispersion over a wide range of wavelengths in the near infrared. High refractive index contrast waveguides do permit dispersion engineering and exhibit high field confinement, which enhances light-matter interaction and therefore reduces the threshold for nonlinear effects. High refractive index contrast also permits the realization of tight bends and ring resonator structures. This further enhances nonlinear effects, reducing the threshold for the generation of frequency combs and cascaded Raman lasers [17–19].

Recently, two techniques have been proposed for creating a thin KY(WO$_4$)$_2$ layer with high refractive index contrast with respect to the substrate. In the

first approach, a $KY(WO_4)_2$ crystal is bonded to a glass carrier, before being lapped and polished to a thickness of <2 μm [20,21]. A refractive index contrast of ~0.5 is achieved using this technique. In the second approach, the crystal is irradiated with carbon ions at an energy of 9 MeV [22]. Due to electronic interactions of the carbon ions with the crystalline material, a layer extending ~1.5-3 μm below the surface is fully amorphized for fluences above $2.7 \cdot 10^{14}$ ion/cm^2. The refractive index of the amorphous layer is ~0.3 lower than the refractive index of the crystalline surface layer core.

The amorphized layer induced by ion irradiation has been reported to exhibit a preferential etching in common wet etching solutions with respect to the undamaged material. Such amorphization-enhanced wet etching has been observed in other material systems after both ion irradiation and pulsed laser modification. It has been reported before in several crystalline materials, including $LiNbO_3$ [23], sapphire [24,25] and silicon [26], as well as amorphous materials such as fused silica [27] and Foturan glass [28]. Irradiation followed by selective etching has been used to create structures such as underetched sheets [24], ridge waveguides [29] and microfluidic channels [27].

In this work, we exploit the selective etching of the irradiation-induced amorphous layer relative to the undamaged crystalline structure of undoped $KY(WO_4)_2$ to further increase the contrast of the $KY(WO_4)_2$ waveguides by producing a pedestal geometry, in which the mode lies inside a thin $KY(WO_4)_2$ layer surrounded by air. A refractive index contrast of Δn~1 between disk and air is achieved using this method.

4.2 Fabrication process of pedestal microdisks in $KY(WO_4)_2$

The fabrication process flow for the proposed pedestal microdisks can be seen in Figure 4.1. A $KY(WO_4)_2$ slab of dimensions 10×10×1 mm^3 was purchased from Altechna. One of the 10×10 mm^2 facets of the sample was polished by the manufacturer to an RMS roughness of 1.5 nm. The sample was irradiated with carbon ions accelerated to an energy of 9 MeV in a tandem accelerator, at a total fluence of $3 \cdot 10^{14}$ cm^{-2}.
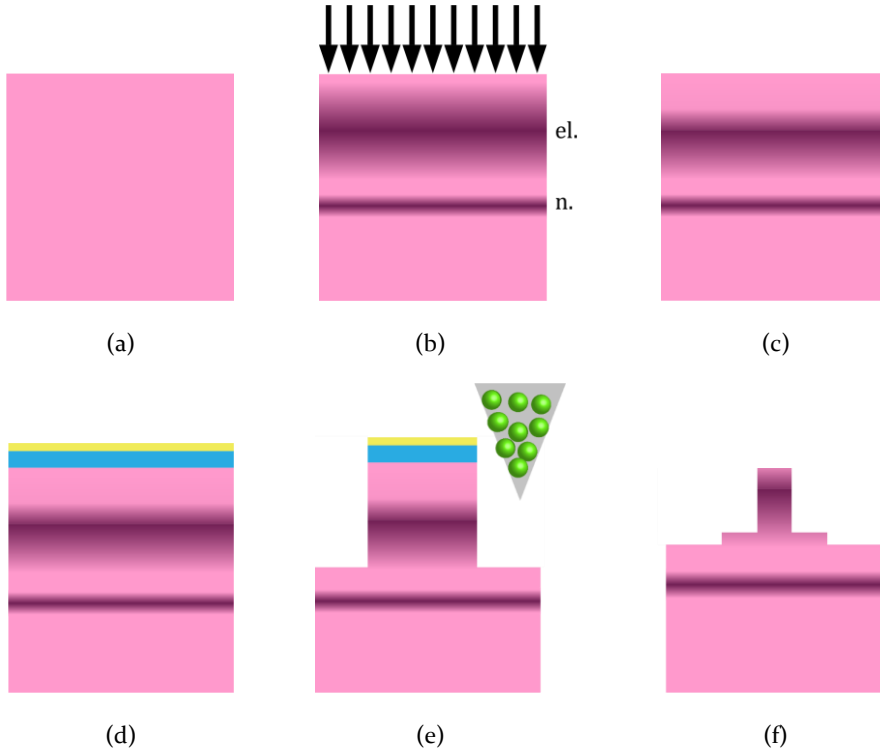
Figure 4.1: Complete process flow. (a) Virgin $KY(WO_4)_2$ substrate. (b) Ion irradiation creates a refractive index gradient. The electronic barrier is marked by "el." and the nuclear barrier is marked by "n.". (c) Thermal annealing removes point defects and repairs the $KY(WO_4)_2$ that is only partially amorphized, which makes the refractive index profile more step-like. (d) Overgrowth with protective PECVD SiO_2 (in blue) and AuPd SEM coating (in yellow). (e) FIB milling with 30 keV Ga+ ions and a current of 21 nA. (f) Wet etching with HCl and TMAH followed by SiO_2 removal with HF. The top of the sample contains an unetched disk. Beneath it is an underetched region.

During irradiation, the samples were attached to the sample holder with copper tape to avoid charging of the non-conductive $KY(WO_4)_2$ substrate. Irradiation was performed at an angle of 5° to avoid channeling. An ion beam area of 3×3 cm² was utilized to ensure uniform irradiation of the 1 cm² sample. The ion current was kept below 1 μA to prevent heating of the sample. Because the applied fluence is above the amorphization threshold, an amorphized barrier region appears in the substrate at around 1.5-3 μm below the surface, centered around the peak of the electronic stopping power. Another damage region is generated by the nuclear stopping power. The nuclear barrier is much thinner and occurs around 5 μm into the substrate [22]. This work is only concerned with the amorphized electronic barrier. The sample was then

annealed at 350°C for 3 hours in order to repair point defects, reduce propagation losses and sharpen the refractive index boundary by repairing partially amorphized $KY(WO_4)_2$ [22]. In future devices, this annealing will be performed after milling to repair any potential damage caused by the Ga^+ ions [30].

An FEI Nova 600 NanoLab DualBeam focused ion beam (FIB) system with Ga^+ ions at an acceleration voltage of 30 kV and a current of 21 nA was used to pattern disks, with a milling depth of 5 μm or more (Figure 4.2). Sufficient milling depth is necessary for exposing the amorphized barrier and giving access to the etching solution. The milling direction was towards the disk, in order to avoid re-deposition on the sidewalls of the milled structure. A 300 nm PECVD SiO_2 layer was grown on the sample to protect the top surface from the etchant, and a 5 nm AuPd layer was sputtered before milling to avoid charging.

(a)   (b)
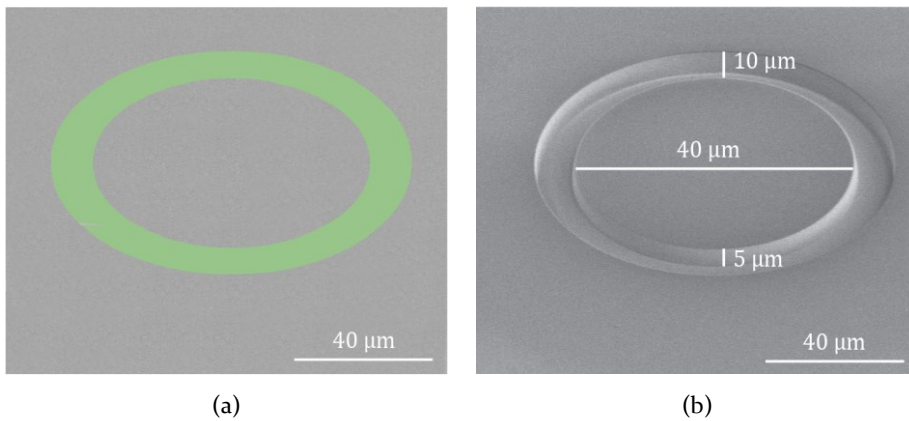
Figure 4.2: (a) Overlay of SEM image and FIB pattern. The green ring represents the material to be milled. (b) Resulting FIB milled microdisk in $KY(WO_4)_2$.

Preferential wet etching was then performed using a 20% HCl solution at room temperature. Although crystalline $KY(WO_4)_2$ is a chemically inert material, there are references to ion exchange reactions at elevated temperatures [31]:

$$KY(WO_4)_2 + 4\,HCl \xrightarrow{100\,°C} KCl + YCl_3 + 2\,WO_3 + 2\,H_2O \tag{3.1}$$
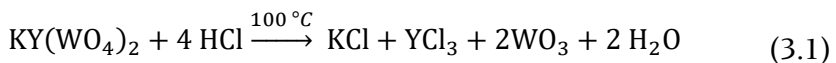
While this reaction only occurs near the boiling point of HCl in crystalline KY(WO$_4$)$_2$, we demonstrate in this work that 20% HCl is effective at room temperature to etch the amorphized region. Looking at (3.1), a potential issue is the reaction product WO$_3$, which is insoluble in water.

The resulting structure after 6 hours of etching was imaged using FIB cross-sectioning and SEM (Figure 4.3). A significant amount of underetching was observed. However, residues after the etching step can be seen (Figure 4.3 (a)). The residues produced clogging of the opening and prevented further access to the HCl etching solution. It is hypothesized that the residues are WO$_3$ produced during the etching of amorphous KY(WO$_4$)$_2$ in HCl, as predicted by (3.1).

The residues were investigated using microRaman spectroscopy. The measured spectrum (Figure 4.4) showed peaks at 261 cm^{-1}, 708 cm^{-1}, and 804 cm^{-1}, which are within the range of peaks associated to WO$_3$ nanocrystals between 4 nm and 35 nm [32]. Since WO$_3$ is soluble in alkaline solutions [33], an etching step in 25% TMAH at room temperature was implemented. The sample was again imaged after etching for 1 hour in TMAH in order to verify the effectiveness in the removal of the WO$_3$ residues. Figure 4.3 (b) shows the cross-section of the disk after the TMAH etching step. TMAH successfully removed the residues, both the clog as well as the thin WO$_3$ layer on the bottom side of the KY(WO$_4$)$_2$ suspended core.

(a)   (b)
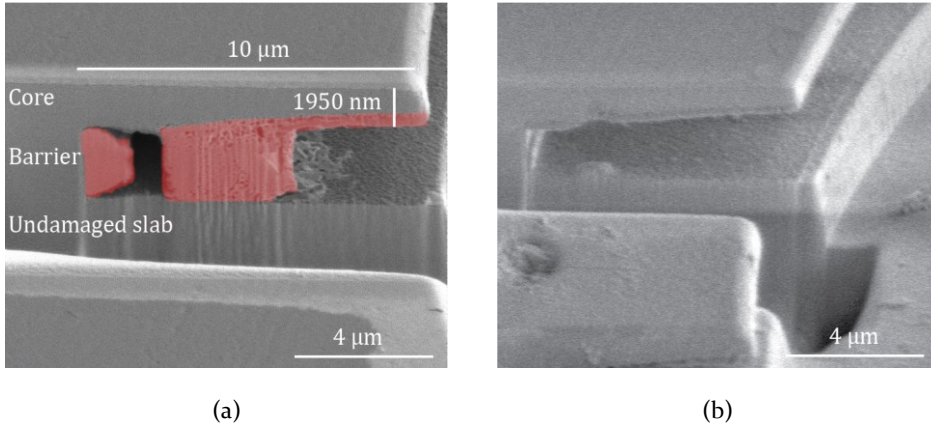
Figure 4.3: (a) FIB cross-section of a $KY(WO_4)_2$ disk etched in 20% HCl for 6 hours. The wet etching process is effective at reaching deep into the material. The etching is faster at the interfaces of the barrier, as indicated on the left edge of the cavity. A large amount of unetched material remains and has been artificially colored. (b) The same sample after 1 hour of etching in 25% TMAH. The residues have been completely removed, including the coating on the bottom side of the core as well as the wedge shape on the left.

An optimized etching process was implemented. The HCl concentration was increased to 32% and the HCl and TMAH steps were performed twice. The sample was etched in 32% HCl for 2 hours, followed by a cleaning step of 1 hour in TMAH. This process was repeated twice (i.e., 2 hours in HCl, 1 hour in TMAH, 2 hours in HCl and 1 hour in TMAH) to achieve a total underetch of 29 µm. After wet etching, the sample was dried using the cyclohexane freeze-drying technique [34]. In this method, the etchant is gradually and sequentially diluted and replaced with water, acetone and finally cyclohexane, which is sublimated at -5° C. Whereas evaporation of water can cause free-standing structures to crack because of capillary forces, freeze-drying with cyclohexane avoids this issue. The pedestal disks were imaged with the SEM in the DualBeam FIB using 2 kV acceleration voltage (Figure 4.5).
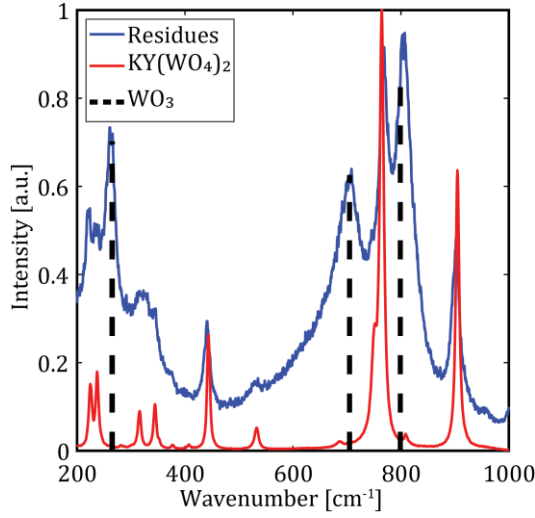
Figure 4.4: Raman spectrum of residues compared with crystalline KY(WO$_4$)$_2$ from the same sample with laser polarization $E||c$, differentiated by the depth of the focus. The Raman peaks associated with 16 nm WO$_3$ nanocrystals are indicated with dashed lines at 265 cm^{-1}, 705 cm^{-1}, and 799 cm^{-1} [32].

4.3 Characterization of the pedestal microdisks

A cross-section of the structure after FIB milling and two cycles of 2 hours etching in 32% HCl at room temperature followed by 1 hour of 25% TMAH is shown in Figure 4.5 (b). An underetch of 29 µm was measured, which corresponds to an etch rate of ~120 nm/min. However, the cross-section is divided into two segments of different thicknesses. The outer segment exhibits a uniform thickness of ~1 µm. The layer gradually tapers, starting at 10 µm from the edge, indicating incomplete removal of the amorphized region. The outer thickness corresponds to the undamaged (crystalline) region predicted by SRIM simulations [22]. The high selectivity between the undamaged core area and the amorphized barrier leads to a self-stopped wet etch. The subsequent TMAH cleaning further removes the WO$_3$ residues from the bottom side of the core. An etch rate of 158 nm/min can be calculated for this region.

Throughout the 10 µm closest to the centre, the thickness is uniformly 2 µm. This second region is attributed to the second HCl etching step, which proceeded at a lower etching rate due to restricted diffusion, even though the etchant solutions were identical. The higher thickness of this segment suggests that the etching step was not self-terminated, and amorphous material is still present. However, calculations show that any underetch

deeper than 4 µm is more than sufficient to have a highly confined mode in the outer rim of the microdisk at an operation wavelength of 1550 nm [35].

(a)

(b)
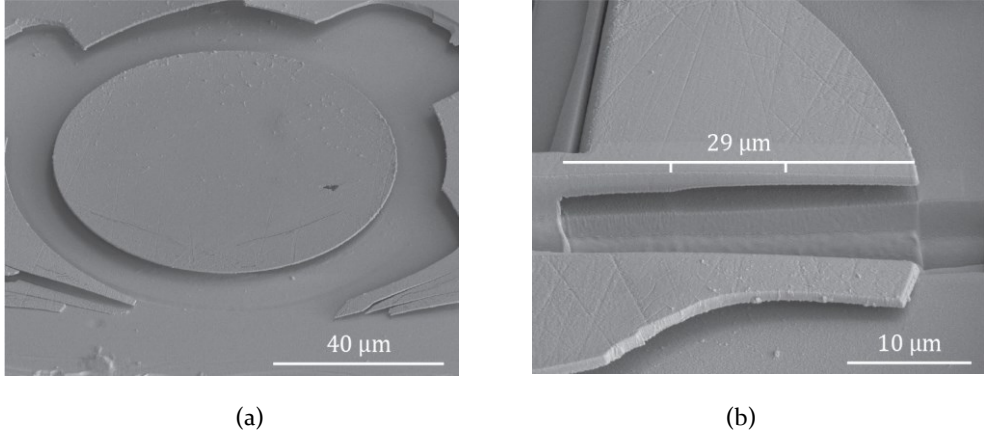
Figure 4.5: (a) SEM image of an 80 µm diameter pedestal disk in $KY(WO_4)_2$ after two rounds of 32% HCl for two hours, each of them followed by a 25% TMAH etching step for one hour. (b) Cross-section of a $KY(WO_4)_2$ sample that has been etched for two rounds of two hours in 32% HCl and 1 hour in 25% TMAH. The horizontal depth of the underetch is 29 µm, the vertical depth is 3 µm and the disk is 1 µm thick throughout the outer 10 µm of the disk. The approximate boundaries between the initial etch, the transition region and the final etch are indicated by notches.

In order to investigate the roughness of the bottom of the disks, a destructive tape peeling technique was used in combination with AFM. RevAlpha 3195 tape was pressed onto the sample and peeled off in order to release the disks and expose the bottom surface, shown in Figure 4.6. A Bruker Dimension ICON AFM was used to inspect the sample using a triangular ScanAsyst-Air probe with a tip radius of 4 nm in PeakForce Tapping mode. The resulting AFM image is shown in Figure 4.7. The root mean square (RMS) roughness is 23.4 nm, measured in three locations of the sample, each 1.5x1.5 µm², and the bottom to peak height difference is 165.6 nm. Such a high roughness will induce high propagation losses, and should be reduced.
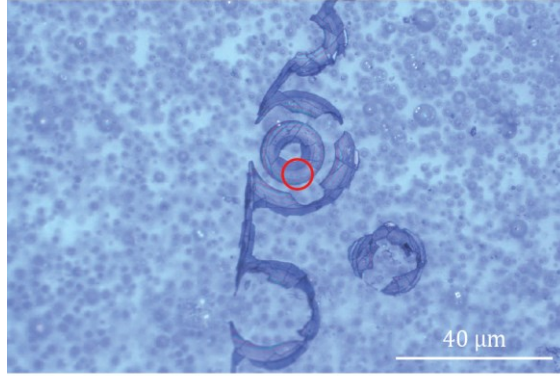
Figure 4.6: Optical microscope image of the remaining KY(WO$_4$)$_2$ structures after transfer to adhesive tape. The center of the disk has not been transferred because it is firmly attached to the pedestal. The underetched area surrounding the disk, also visible in Figure 4.5 (a), has also been transferred. The area of main interest is indicated by the red circle, selected for its lack of cracks.
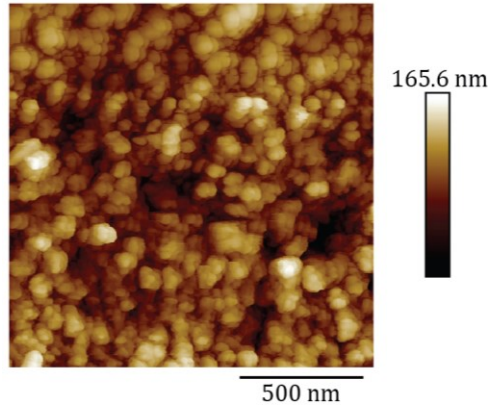

Figure 4.7: AFM image of a 1.5 μm by 1.5 μm section of the underside of the disk in Figure 2. The image was made close to the edge of the disk.

4.4   Summary

In this work, we report the first realization of pedestal structures in crystalline KY(WO$_4$)$_2$. The process is based on the selectivity of an HCl wet etching step between the crystalline and amorphized KY(WO$_4$)$_2$ after swift carbon ion irrdiation with an energy of 9 MeV and a fluence (3·10^{14} ion/cm^2) above the amorphization threshold. WO$_3$ residues were produced during the etching step that limited the depth of the under-etch. A cleaning step in TMAH cleaned the structure from WO$_3$ residues and permitted to extend the etching further. The proposed technology paves the road towards the fabrication of

high-refractive index constrast pedestal structures for highly efficient non-linear devices once the roughness on the inner surface of the pedestal is drastically reduced.

4.5 Acknowledgements

Bibliography

1. A. A. Kovalyov, V. V. Preobrazhenskii, M. A. Putyato, O. P. Pchelyakov, N. N. Rubtsova, B. R. Semyagin, V. E. Kisel', S. V. Kuril'chik, and N. V. Kuleshov, "115 fs pulses from Yb^{3+}:$KY(WO_4)_2$ laser with low loss nanostructured saturable absorber," Laser Phys. Lett. **8**(6), 431–435 (2011).

2. A. A. Lagatsky, F. Fusari, S. Calvez, J. A. Gupta, V. E. Kisel, N. V. Kuleshov, C. T. A. Brown, M. D. Dawson, and W. Sibbett, "Passive mode locking of a Tm,Ho:$KY(WO_4)_2$ laser around 2 μm," Opt. Lett. **34**(17), 2587–2589 (2009).

3. F. Brunner, G. J. Spühler, J. A. Au, L. Krainer, F. Morier-Genoud, R. Paschotta, N. Lichtenstein, S. Weiss, C. Harder, A. A. Lagatsky, A. Abdolvand, N. V. Kuleshov, and U. Keller, "Diode-pumped femtosecond Yb:$KGd(WO_4)_2$ laser with 1.1-W average power," Opt. Lett. **25**(15), 1119–1121 (2000).

4. U. Griebner, S. Rivier, V. Petrov, M. Zorn, G. Erbert, M. Weyers, X. Mateos, M. Aguiló, J. Massons, and F. Díaz, "Passively mode-locked Yb:$KLu(WO_4)_2$ oscillators," Opt Express **13**(9), 3465–3470 (2005).

5. A. A. Kaminskii, P. V. Klevtsov, L. Li, and A. A. Pavlyuk, "Stimulated emission from $KY(WO_4)_2$: Nd^{3+} crystal laser," Phys Status Solidi A **5**(2), K79–K81 (1971).

6. V. Petrov, M. C. Pujol, X. Mateos, Ò. Silvestre, S. Rivier, M. Aguiló, R. M. Solé, J. Liu, U. Griebner, and F. Díaz, "Growth and properties of $KLu(WO_4)_2$, and novel ytterbium and thulium lasers based on this monoclinic crystalline host," Laser Photonics Rev. **1**(2), 179–212 (2007).

7. S. Aravazhi, D. Geskus, K. van Dalfsen, S. A. Vázquez-Córdova, C. Grivas, U. Griebner, S. M. Garcia-Blanco, and M. Pollnau, "Engineering lattice matching, doping level, and optical properties of $KY(WO_4)_2$:Gd, Lu, Yb layers for a cladding-side-pumped channel waveguide laser," Appl. Phys. B **111**(3), 433–446 (2013).

8. N. Thilmann, G. Strömqvist, M. C. Pujol, V. Pasiskevicius, V. Petrov, and F. Díaz, "Nonlinear refractive indices in Yb^{3+}-doped and undoped monoclinic double tungstates $KRE(WO_4)_2$ where RE=Gd, Y, Yb, Lu," Appl. Phys. B **96**(2–3), 385–392 (2009).

9. K. Ikeda, R. E. Saperstein, N. Alic, and Y. Fainman, "Thermal and Kerr nonlinear properties of plasma-deposited silicon nitride/silicon dioxide waveguides," Opt. Express **16**(17), 12987–12994 (2008).

10. C. J. Krückel, A. Fülöp, T. Klintberg, J. Bengtsson, P. A. Andrekson, and V. Torres-Company, "Linear and nonlinear characterization of low-stress

high-confinement silicon-rich nitride waveguides," Opt. Express **23**(20), 25827–25837 (2015).

11. J. A. Piper and H. M. Pask, "Crystalline Raman Lasers," IEEE J. Sel. Top. Quantum Electron. **3**(13), 692–704 (2007).

12. Z. Cong, Z. Liu, Z. Qin, X. Zhang, H. Zhang, J. Li, H. Yu, and W. Wang, "LD-pumped actively Q-switched Nd:KLu(WO$_4$)$_2$ self-Raman laser at 1185 nm," Opt. Laser Technol. **73**, 50–53 (2015).

13. Y.-S. Yong, S. Aravazhi, S. A. Vázquez-Córdova, J. J. Carvajal, F. Díaz, J. L. Herek, S. M. Garcia-Blanco, and M. Pollnau, "Direct confocal lifetime measurements on rare-earth-doped media exhibiting radiation trapping," Opt. Mater. Express **7**(2), 527–532 (2017).

14. S. A. Vázquez-Córdova, S. Aravazhi, C. Grivas, Y.-S. Yong, S. M. Garcia-Blanco, J. L. Herek, and M. Pollnau, "High optical gain in erbium-doped potassium double tungstate channel waveguide amplifiers," Opt. Express **26**(5), 6260–6266 (2018).

15. K. van Dalfsen, S. Aravazhi, C. Grivas, S. M. Garcia-Blanco, and M. Pollnau, "Thulium channel waveguide laser with 1.6 W of output power and ~80% slope efficiency," Opt. Lett. **39**(15), 4380–4383 (2014).

16. D. Geskus, S. Aravazhi, C. Grivas, K. Wörhoff, and M. Pollnau, "Microstructured KY(WO$_4$)$_2$:Gd^{3+}, Lu^{3+}, Yb^{3+} channel waveguide laser," Opt. Express **18**(9), 8853 (2010).

17. G. Lin, A. Coillet, and Y. K. Chembo, "Nonlinear photonics with high-Q whispering-gallery-mode resonators," Adv. Opt. Photonics, AOP **9**(4), 828–890 (2017).

18. S. M. Spillane, T. J. Kippenberg, and K. J. Vahala, "Ultralow-threshold Raman laser using a spherical dielectric microcavity," Nature **415**(6872), 621–623 (2002).

19. B. Min, T. J. Kippenberg, and K. J. Vahala, "Compact, fiber-compatible, cascaded Raman laser," Opt. Lett. **28**(17), 1507–1509 (2003).

20. C. I. van Emmerik, S. M. Martinussen, J. Mu, M. Dijkstra, R. Kooijman, and S. M. Garcia-Blanco, "A novel polishing stop for accurate integration of potassium yttrium double tungstate on a silicon dioxide platform," in Proc. SPIE (2018), **10535**.

21. M. A. Sefünç, F. B. Segerink, and S. M. Garcia-Blanco, "High index contrast passive potassium double tungstate waveguides," Opt. Mater. Express **8**(3), 629–638 (2018).

22. R. N. Frentrop, V. Tormo-Márquez, J. Olivares, and S. M. García-Blanco, "High-contrast slab waveguide fabrication in KY(WO$_4$)$_2$ by swift heavy ion irradiation," in Proc. SPIE (2018), **10535**.

23. F. Schrempel, Th. Gischkat, H. Hartung, E.-B. Kley, and W. Wesch, "Ion beam enhanced etching of LiNbO$_3$," Nucl. Instrum. Methods. Phys. Res. B **250**(1), 164–168 (2006).
24. A. Crunteanu, G. Jänchen, P. Hoffmann, M. Pollnau, C. Buchal, A. Petraru, R. W. Eason, and D. P. Shepherd, "Three-dimensional structuring of sapphire by sequential He+ ion-beam implantation and wet chemical etching," Appl. Phys. A **76**(7), 1109–1112 (2003).
25. L. Capuano, R. Pohl, R. M. Tiggelaar, J. W. Berenschot, J. G. E. Gardeniers, and G. R. B. E. Römer, "Morphology of single picosecond pulse subsurface laser-induced modifications of sapphire and subsequent selective etching," Opt. Express **26**(22), 29283–29295 (2018).
26. S. Lee, K. Jo, H. Keum, S. Chae, Y. Kim, J. Choi, H. H. Lee, and H. J. Kim, "Nanowall formation by maskless wet-etching on a femtosecond laser irradiated silicon surface," Appl. Surf. Sci **437**, 190–194 (2018).
27. R. Osellame, H. J. W. M. Hoekstra, G. Cerullo, and M. Pollnau, "Femtosecond laser microstructuring: an enabling tool for optofluidic lab-on-chips," Laser Photonics Rev. **5**(3), 442–463 (2011).
28. K. Sugioka, Y. Hanada, and K. Midorikawa, "Three-dimensional femtosecond laser micromachining of photosensitive glass for biomicrochips," Laser Photonics Rev. **4**(3), 386–400 (2010).
29. P. D. Nicola, S. Sugliani, G. B. Montanari, A. Menin, P. Vergani, A. Meroni, M. Astolfi, M. Borsetto, G. Consonni, R. Longone, A. Nubile, M. Chiarini, M. Bianconi, and G. G. Bentini, "Fabrication of Smooth Ridge Optical Waveguides in LiNbO$_3$ by Ion Implantation-Assisted Wet Etching," J. Light. Technol. **31**(9), 1482–1487 (2013).
30. L. a. M. Barea, F. Vallini, A. R. Vaz, J. R. Mialichi, and N. C. Frateschi, "Low-roughness active microdisk resonators fabricated by focused ion beam," J. Vac. Sci. Technol. B **27**(6), 2979–2981 (2009).
31. Y. Romanyuk, "Liquid-phase epitaxy of doped KY(WO$_4$)$_2$ layers for waveguide lasers," PhD Thesis, École Polytechnique Fédérale de Lausanne (2005).
32. M. Boulova and G. Lucazeau, "Crystallite Nanosize Effect on the Structural Transitions of WO$_3$ Studied by Raman Spectroscopy," J. Solid State Chem. **167**(2), 425–434 (2002).
33. D. R. Lide, *CRC Handbook of Chemistry and Physics: A Ready-Reference Book of Chemical and Physical Data* (CRC-Press, 1995).
34. R. Legtenberg and H. A. C. Tilmans, "Electrostatically driven vacuum-encapsulated polysilicon resonators Part I. Design and fabrication," Sens Actuators A Phys **45**(1), 57–66 (1994).

35. S. M. Martinussen, R. N. Frentrop, M. Dijkstra, F. Segerink, V. Tormo-Márquez, J. Olivares, and S. M. Garcia-Blanco, "Pedestal disk resonator in potassium yttrium double tungstate," in *Proc. SPIE* (2018), **10535**.

CHAPTER 5

High-Q Al_2O_3 racetrack resonators with anomalous integrated dispersion

In this paper we present dispersion engineered racetrack resonators with quality factors up to 7.67×10^5 at C-band wavelengths in high-index reactive sputtered Al_2O_3. The rings are engineered for anomalous dispersion, making them suitable for nonlinear integrated photonics, and have a free spectral range of 124 GHz. Propagation losses down to 0.47 dB/cm in fully-etched, highly confined, high-index strip Al_2O_3 waveguides are experimentally demonstrated.

5.1 Introduction

Aluminum oxide, Al_2O_3, is a promising material platform for integrated optics [1]. It has a wide transparency range [2], spanning from 150 nm to 5.5 μm, can easily be doped with rare-earth ions for use in on-chip amplifiers [3–5] and lasers [4,6,7], and has been successfully used for highly sensitive biosensors [8–11]. The nonlinear refractive index, n_2, is estimated to be 4.77×10^{-20} m^2W^{-1} [12], and four-wave mixing has been demonstrated [13]. Furthermore, it can be integrated with silicon nitride technology [14–16] or with itself in a photonic dual damascene process [17] to combine active and passive functionalities on one chip.

Resonators are a key component in several of the integrated optical devices listed above. Furthermore, they are essential for more complex nonlinear devices such as frequency combs and quantum-coherent frequency conversion [18]. Such devices are promising for quantum communications [19], astrospectroscopy [20], and many other advanced applications [21].

These devices rely on $\chi^{(3)}$ processes, which are quite weak and require high performance resonators. Such a resonator should exhibit a high Q-factor, typically higher than 10^6 over a wide spectral range. It should also have a small mode volume to maximize the electric field enhancement. Maximizing the Q-factor is especially important in the case of Al_2O_3, due to its comparatively low n_2 relative to other materials of similar refractive index, such as Hydex [22].

Furthermore, the resonator should be dispersion engineered to have anomalous group velocity dispersion [23]. This means that around the pump wavelength, the group velocity should increase with increasing wavelength. This is necessary in order to generate and sustain bright solitons or to excite Turing roll patterns [23]. In this work, we fabricate racetrack resonators in highly confined high refractive index Al_2O_3 channel waveguides and characterize their Q-factors and dispersion characteristics.

5.2 Device fabrication

The layers were grown on a (1 0 0) Si wafer overgrown with 8 μm of thermal oxide, with the Al_2O_3 deposited in an AJA ATC 15000 RF reactive co-sputtering system [13]. In this process, based on Emmerik et al [24], the chamber pressure was 3.4 mTorr, the Ar flow was 30 sccm and the O_2 flow was 1.6 sccm. The wafer was kept at a setpoint of 700 °C during the deposition

by backside illumination with halogen lamps. The RF power was 200 W and the bias voltage remained stable between 612 V and 613 V throughout the sputtering process. Under these conditions, the Ar partial pressure was 3.3 mTorr ± 0.1 mTorr and the O_2 partial pressure was 0.1 mTorr ± 0.1 mTorr. A 1.26 μm thick Al_2O_3 layer was deposited, at a rate of 3.82 nm/minute.

The layer was characterized by ellipsometry in a J.A. Woollam M-2000 ellipsometer, using a deuterium lamp and a quartz tungsten halogen lamp, which cover the wavelength range from 400 nm to 1600 nm. The resulting layer thickness in the center of the wafer was 1260 nm, with Cauchy coefficients $A = 1.722$ and $B = 0.0102$. This results in a refractive index from 1.72 at 1550 nm to 1.76 at 400 nm, which is significantly higher than commonly reported [13–15], indicating denser layers, possibly including a polycrystalline phase [25]. Figure 5.1 shows light propagating along this Al_2O_3 layer under prism coupling in a Metricon 2010M setup, which shows very low propagation losses. Propagation losses <0.1 dB/cm at 1550 nm have been measured in similar layers of reduced thickness (~490 nm) [25].
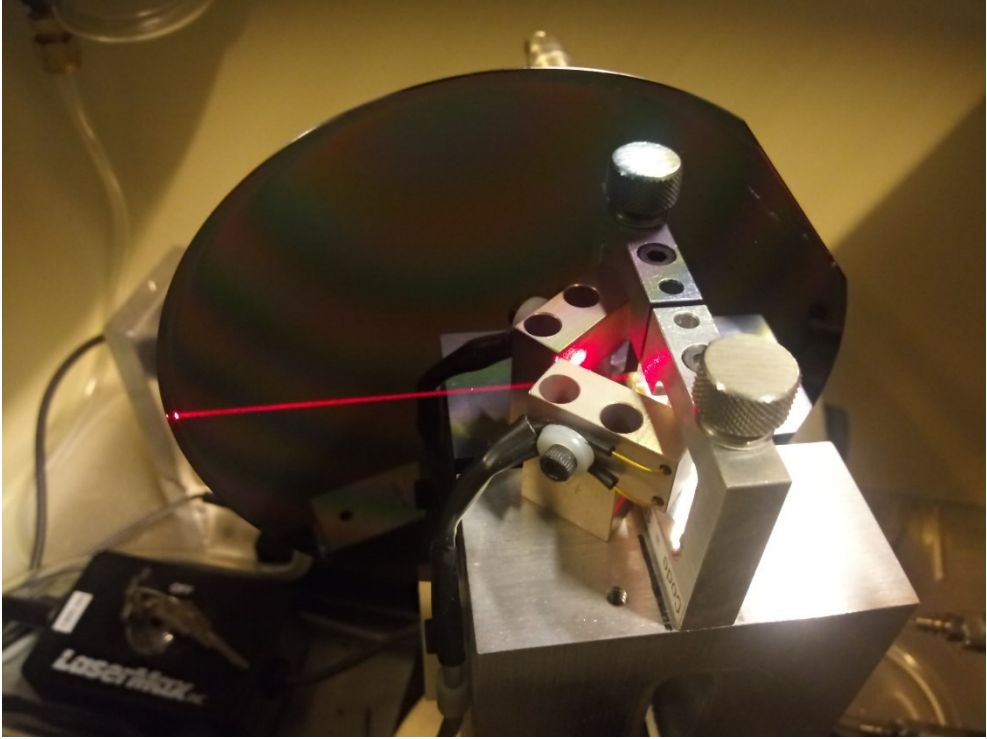
Figure 5.1: Light strike at 632.8 nm of wavelength propagating along the high refractive index thick Al_2O_3 slab waveguide after coupling in a prism coupler setup.

The waveguides were patterned using an EV620 mask aligner with 1.7 µm thick Olin OiR 907-17 photoresist. A 200 nm AZ BARLi-II layer was spin coated below the photoresist and an AZ Aquatar-VIII 45 layer was spin coated on top, as anti-reflection coatings. Etching was performed in an Oxford Instruments PlasmaPro 100 Cobra ICP-RIE system, using a 25 sccm:10 sccm BCl_3:HBr gas mixture, 175 W ICP power and 20 W RF CCP power at a chamber pressure of 3 mTorr. After etching, a cladding layer of 5 µm SiO_2 was deposited by plasma enhanced chemical vapor deposition (PECVD) over the resonators for improved in-coupling efficiency and robustness.

The waveguides were inspected by scanning electron microscopy (SEM) in an FEI Nova FIB/SEM. The resulting images of an uncladded analysis chip are shown in Figure 5.2 (a-c). Figure 5.2 (a) shows a cross-section of a SiO_2 cladded waveguide with a nominal width in the photolithography mask of 2400 nm. This is 400 nm wider than the waveguides analyzed in this work. The cross-section is made at a 1000 nm wide coupling gap between two Al_2O_3

waveguides, demonstrating that there is only slight distortion at the gaps due to proximity effects. Nearly complete etching of the Al_2O_3 inside the gap can be observed, indicating a small amount of RIE lag [26].

A keyhole defect in the PECVD SiO_2 cladding is clearly visible above the coupling gap. This type of defect commonly occurs in silane-based PECVD due to the "bread-loaf" effect [27] where the film grows more rapidly on corners than inside the gap, leaving a void above a filled trench. Solutions include high-density plasma CVD and using TEOS- rather than silane-based processes.

Figure 1 (b) shows a side view of an uncladded waveguide at a bend, revealing some sidewall roughness. This image is from a different wafer fabricated using the same process but without cladding, as it is impossible to inspect the sidewalls of the cladded waveguides directly.

The resonators used in this work have a racetrack configuration with a coupling length of 50 μm, an example of which is shown in Figure 1 (c). The measured waveguide base width is 2.2 μm, the top width is 1.3 μm, and the sidewall angle is 70°. This is 400 nm narrower than the waveguide shown in Figure 5.2 (a), as the nominal width in the photolithography mask was 2 μm for the analyzed structures. The radius is 200 μm in order to minimize bend losses as well as transition losses between the bent and straight sections while maintaining a small *FSR* of 124 GHz. This yields a total roundtrip length of 1.35 mm. The simulated TE mode area is 2.1 μm^2, and the TM mode area is 2.2 μm^2.
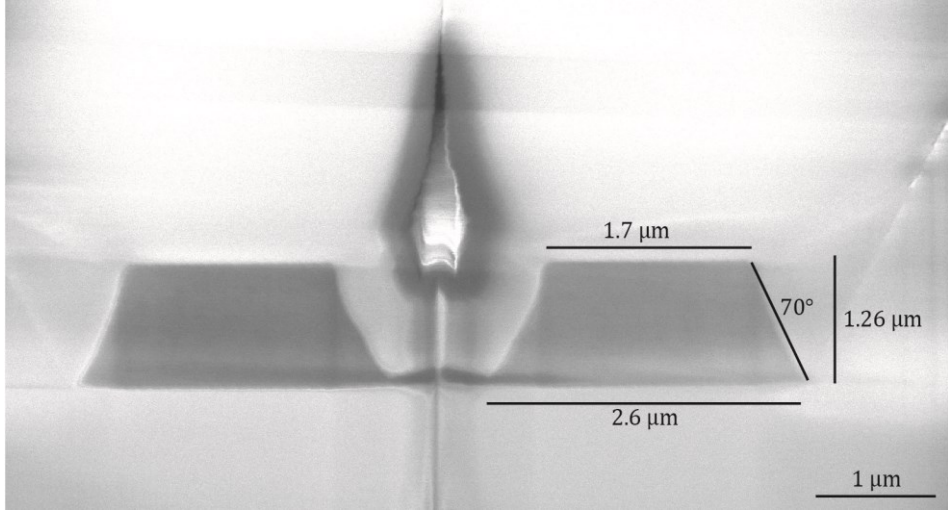
(a)
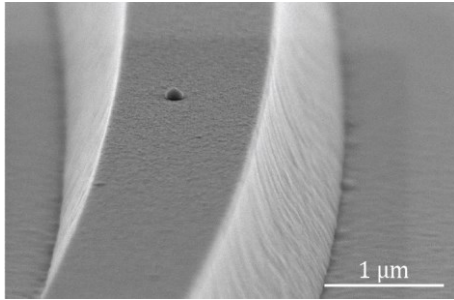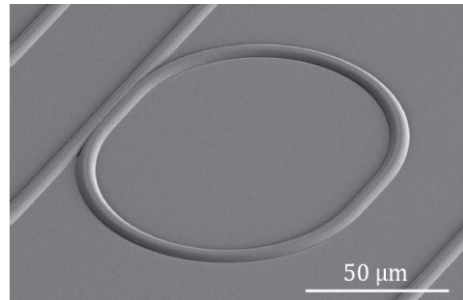
(b)   (c)

Figure 5.2: (a) SEM image of a diced cross-section of a directional coupler with a 1000 nm wide coupling gap. The waveguide has a base width of 2.6 µm and a height of 1.26 µm, and is 400 nm wider than the waveguide optically characterized in this work. (b) Close-up view of a bent waveguide showing some sidewall roughness and a surface defect. (c) SEM top view of a SiO$_2$ cladded racetrack resonator with radius 50 µm and directional coupler length of 50 µm.

5.3 Optical characterization

The resonator was characterized by coupling light into the bus waveguide using a single mode polarization maintaining fiber (PM1500-XP) with a 10.1 µm mode field diameter. Both TE and TM polarizations were studied with a incident power of -10 dBm. An Agilent 81646 tunable laser was used to scan the wavelength in the range of 1460 nm to 1620 nm with a step size of 1 pm. The scanning speed utilized was 10 nm/s, at which the rated absolute wavelength accuracy of the laser is ±4.0 pm. The measured resonances were

fitted to Lorentzian functions, from which the *FWHM* and extinction ratio were extracted [28]. These were then used to calculate the *Q*-factors of the resonances.

The fitting parameters, i.e., peak threshold depth for inclusion in the fit and fitting range around the peak, were optimized by minimizing the standard deviation of the measured resonance *Q*-factors. Only those modes that could be lined up to closely fit a resonance spectrum with a constant *FSR* were included in the *Q*-factor calculation.

Two loss figures can be extracted, corresponding to the propagation and coupling losses. These loss figures can be distinguished provided that the wavelength sweep is performed over a sufficient wavelength range [29], or by comparing identical devices with different coupling gaps.

Figure 5.3 shows the measured transmission spectrum of the racetrack resonator at TM polarization for the whole wavelength range. The inset shows a resonance at 1529.1 nm, with a *FWHM* of 2.5 pm, corresponding to 320 MHz. From this measurement, a loaded *Q*-factor of 6.17×10^5 is extracted, with a finesse of 392. With a fitted extinction ratio of 2.4, this yields an internal *Q*-factor of 7.49×10^5. The average internal *Q*-factor of the resonator is 6.76×10^5, which corresponds to an average propagation loss of 0.48 dB/cm.

The free spectral range of the resonator is 125 GHz in TE and 124 GHz in TM, and the total in-and outcoupling losses are 5.5 dB per facet. The bus to ring coupling coefficient is calculated as 5×10^{-4} dB, and the roundtrip loss is 6.5×10^{-2} dB, which indicates strong undercoupling. For the fundamental TE mode, the average measured propagation loss is 0.52 dB/cm and the average internal *Q*-factor is 6.11×10^5.
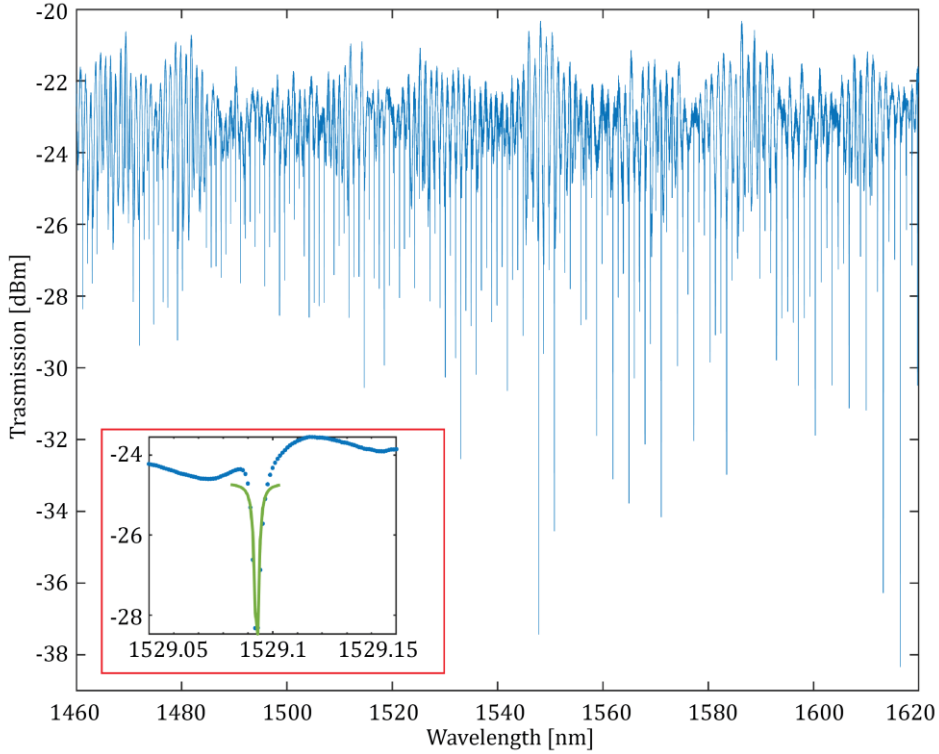
Figure 5.3: Measured TM transmission spectrum of the racetrack resonator with a roundtrip length of 1.35 mm and *FSR* of 124 GHz. The inset shows a resonance peak with an extinction ratio of 2.4, with a *Q* factor of 617000 and a finesse of 392. The Lorentzian fit is included in green.

The group index n_g is shown for both polarizations in Figure 5.4. The TM polarization shows a marginally higher n_g than TE, at 1.773 rather than 1.769. The TE polarization has a slightly increasing n_g with respect to wavelength, indicating anomalous dispersion. The TM polarization, however, has dispersion too close to zero to distinguish the slope from measurement noise.

A significant amount of measurement noise is apparent, which may be related to the scan step size of 1 pm: Using Equation (1.17) with λ = 1550 nm and *FSR* = 1 nm, which are values taken from these measurements, changing *FSR* to 1.001 nm changes n_g by 0.0017.
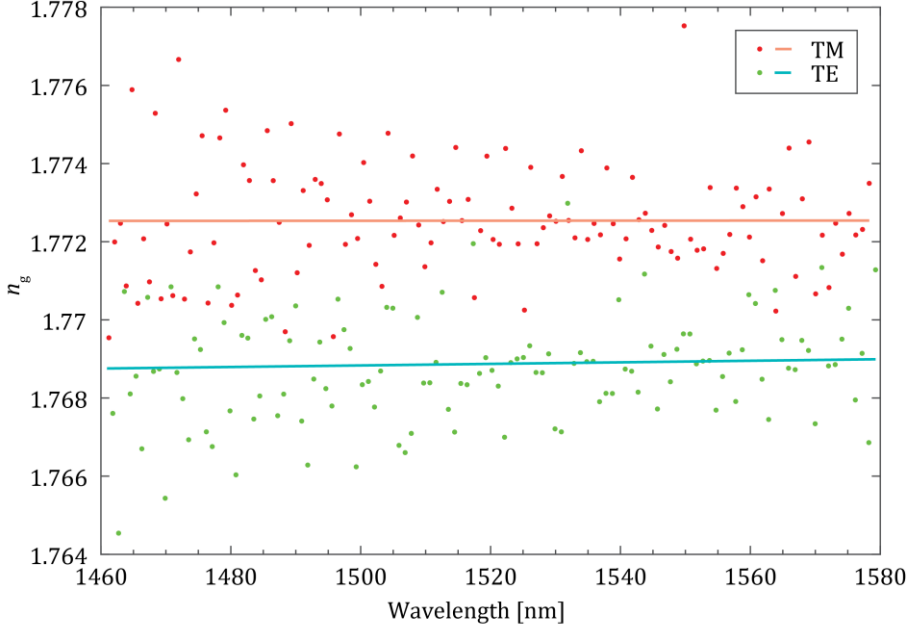
Figure 5.4: Measured group indices (dots) and linear fits (lines) for the fundamental modes of both polarizations in a racetrack resonator with bend radius 200 µm.

The integrated dispersion of a resonator can be extracted by Taylor expanding the resonance frequencies around a central, pumped mode ω_0 [30], such that

$$\omega_\mu = \omega_0 + \sum_j \left. D_j \mu^j \middle/ j! \right. \tag{5.1}$$

In this formalism, $D_1/2\pi$ is the *FSR* and D_2 is proportional to the group velocity dispersion (β_2):

$$D_2 = 8\pi^2 v_g^3 \frac{\beta_2}{L^2} \tag{5.2}$$

It is convenient to lump D_2 and the higher-order terms ($D_3, D_4, \ldots$) together as a whole. By comparing the resonance frequencies with those of an ideal, nondispersive resonator with constant *FSR* [31,32], the so-called integrated dispersion, $D_{\text{int}}(\mu)$, can be calculated as [33]:

$$D_{\text{int}}(\mu) = \omega_\mu - (\omega_0 + D_1\mu) \tag{5.3}$$

In practical terms, the idealized grid frequencies, $\omega_{grid}(\mu)= \omega_0+D_1\mu$, are calculated by setting D_1 in (1.27) to the *FSR* of the resonator at ω_0. The integrated dispersion is then calculated by subtracting $\omega_{grid}(\mu)$ from the measured resonance frequencies ω_μ.

Figure 5.5 (a) shows the integrated dispersion, $D_{int}(\mu)/2\pi$, calculated from the transmission spectrum in TE polarization of the racetrack resonator under study (Figure 5.3). Only the peaks in the transmission spectrum with an extinction of more than 1 dB are included in the integrated dispersion plot. The fundamental TE mode highlighted in cyan is most prominent, with the highest degree of coupling. Traces of the fundamental TM mode are also visible, either due to slight polarization rotation at the in-coupling fiber, or due to mode conversion at the straight-bend transition. More modes are detected that do not fit either mode spectrum, and these are thus assumed to be of higher order. As these have significantly different *FSR* than the fundamental modes, they do not form easily recognizable lines in this plot.

At wavelengths longer than approximately 1580 nm, the TE and TM spectra nearly overlap. This causes a distortion of the measured mode spectra, likely due to an avoided mode crossing. To avoid these distortions from disturbing the calculations, all modes above 1580 nm are not included in the fit of Figure 5.5 (b).

Figure 5.5 (b) shows a magnified fit of the integrated dispersion $(D_{int}(\mu)/2\pi)$ of the fundamental TE mode. A third order polynomial fit yields $D_2/2\pi = 0.33$ MHz $\pm$ 39 KHz 95% confidence bounds, demonstrating anomalous group velocity dispersion. A third order fit was used in order to decouple higher order dispersion terms from D_2. In the fit, the constant and first order term represent deviations from ω_0 (-34 MHz) and D_1 (-4.7 MHz), which are very small in a resonator with 124 GHz *FSR*.

The dispersion calculations are influenced by measurement noise. Even a 6th order polynomial fit, which minimizes the error at the cost of overfitting, has an RMS error of 76 MHz. This corresponds to 0.6 pm. Although this is a lower error than the specification of the laser, it is likely that a more precise frequency standard must be used to produce more accurate measurements.
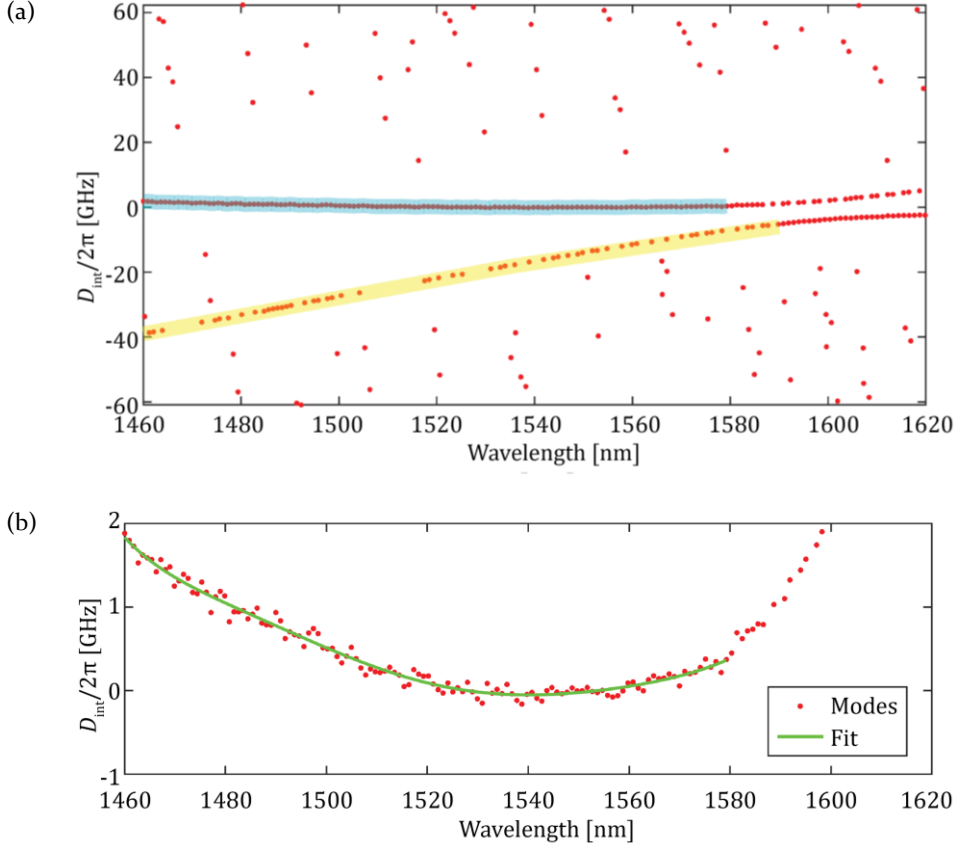
Figure 5.5: (a) Integrated dispersion of a racetrack resonator with bend radius 200 μm. Only resonances with an extinction larger than 1 dB have been considered. The *FSR* at the ω_0 corresponding to λ_0=1550.7 nm is 125 GHz. The fundamental TE mode is highlighted with cyan, and the weakly excited fundamental TM mode is indicated with yellow. Higher order modes are also present, but do not form a clear pattern as their group index is far removed from the fundamental modes. Modes at wavelengths above 1580 nm are assumed to be influenced by an avoided crossing and are not considered. (b) Integrated dispersion of the fundamental TE mode, fitted to a 3rd order polynomial. An anomalous dispersion of $D_2/2\pi$ = 0.33 MHz is extracted.

5.4 Discussion

In this work we have demonstrated, for the first time, a racetrack resonator in Al_2O_3 exhibiting anomalous dispersion, which is a prerequisite for the realization of Kerr frequency combs [23]. To achieve anomalous dispersion, thick (1260 nm) high refractive index (n~1.72 at 1550 nm) Al_2O_3 layers patterned into 2 μm wide fully etched channel waveguides were utilized. Q-factors above 6×10^5 were experimentally demonstrated, which correspond to propagation losses of 0.48 dB/cm. Although not the lowest losses reported in Al_2O_3 channel waveguides, with propagation losses as low as 0.2 dB/cm

previously demonstrated [34], these are the lowest losses reported to date for a fully etched thick highly confined Al_2O_3 channel waveguide.

However, the obtained losses are still too high to achieve efficient Kerr comb generation. The threshold power required for a generation of a Kerr comb can be calculated, as discussed in Chapter 1, as $P_{th} = \frac{\omega n_0^2 A_{\text{eff}} L}{4 c n_2 Q^2}$ (1.31), with $A_{\text{eff}} = \frac{\left(\iint |E|^2 dxdy\right)^2}{\iint |E|^4 dxdy}$ (1.3). The calculated threshold pump power in our resonator is still high at 478 mW, which, in combination with a strong under-coupling, makes Kerr comb generation challenging.

Further work should focus on increasing the coupling efficiency and reducing the losses, in order to increase Q. The current waveguides were fabricated by UV contact lithography, which produces sidewall roughness. Electron beam lithography to produce smaller gaps in combination with a reflow process to further reduce sidewall roughness should be investigated. Furthermore, a chemical-mechanical polishing process can be developed to reduce top surface roughness [35]. Sidewall roughness may be further reduced by means of an annealing step in the correct atmosphere [36]. The resonator can also be optimized by implementing adiabatic bends to eliminate the straight-to-bend transition losses. The waveguides can be made narrower to ensure single-mode operation, or a single mode region may be introduced to remove higher order modes [31].

5.5 Conclusion

We have demonstrated integrated racetrack resonators in high-index ($n{\sim}1.72$ at 1550 nm), highly confined Al_2O_3 waveguides. Internal Q factors up to 676000 were obtained. Using thicker layers, deeper etching, and a higher index material than other previously reported approaches, we have produced the first dispersion engineered low-loss waveguides in Al_2O_3. This is an important step towards nonlinear optical functionality in this material system, including the generation of Kerr combs.

Bibliography

1. W. A. P. M. Hendriks, L. Chang, C. I. van Emmerik, J. Mu, M. de Goede, M. Dijkstra, and S. M. Garcia-Blanco, "Rare-earth ion doped Al_2O_3 for active integrated photonics," Adv. Phys. X **6**(1), 1833753 (2021).
2. E. R. Dobrovinskaya, L. A. Lytvynov, and V. Pishchik, *Sapphire: Material, Manufacturing, Applications* (Springer US, 2009).
3. S. A. Vázquez-Córdova, M. Dijkstra, E. H. Bernhardi, F. Ay, K. Wörhoff, J. L. Herek, S. M. García-Blanco, and M. Pollnau, "Erbium-doped spiral amplifiers with 20 dB of net gain on silicon," Opt. Express **22**(21), 25993–26004 (2014).
4. J. D. B. Bradley and M. Pollnau, "Erbium-doped integrated waveguide amplifiers and lasers," Laser Photonics Rev. **5**(3), 368–403 (2011).
5. K. Worhoff, J. D. B. Bradley, F. Ay, D. Geskus, T. P. Blauwendraat, and M. Pollnau, "Reliable Low-Cost Fabrication of Low-Loss Al_2O_3:Er^{3+} Waveguides With 5.4-dB Optical Gain," IEEE J. Quantum Electron. **45**(5), 454–461 (2009).
6. E. H. Bernhardi, H. A. G. M. van Wolferen, K. Wörhoff, R. M. de Ridder, and M. Pollnau, "Highly efficient, low-threshold monolithic distributed-Bragg-reflector channel waveguide laser in Al_2O_3:Yb^{3+}," Opt. Lett. **36**(5), 603–605 (2011).
7. N. Li, G. Singh, E. S. Magden, Z. Su, N. Singh, M. Moresco, G. Leake, J. D. B. Bradley, and M. R. Watts, "Reliable Integrated Photonic Light Sources Using Curved Al_2O_3:Er^{3+} Distributed Feedback Lasers," IEEE Photon. J. **9**(4), 1–9 (2017).
8. M. de Goede, L. Chang, J. Mu, M. Dijkstra, R. Obregón, E. Martínez, E. Martínez, E. Martínez, L. Padilla, F. Mitjans, and S. M. Garcia-Blanco, "Al_2O_3:Yb^{3+} integrated microdisk laser label-free biosensor," Opt. Express **44**(24), 5937–5940 (2019).
9. M. de Goede, M. Dijkstra, R. Obregón, J. Ramón-Azcón, E. Martínez, L. Padilla, F. Mitjans, and S. M. Garcia-Blanco, "Al_2O_3 microring resonators for the detection of a cancer biomarker in undiluted urine," Opt. Express **27**(13), 18508–18521 (2019).
10. M. de Goede, M. Dijkstra, L. Chang, N. Acharyya, N. Acharyya, G. Kozyreff, R. Obregón, E. Martínez, E. Martínez, E. Martínez, and S. M. García-Blanco, "Mode-splitting in a microring resonator for self-referenced biosensing," Opt. Express **29**(1), 346–358 (2021).
11. L. Chang, M. de Goede, M. Dijkstra, C. I. van Emmerik, and S. M. García-Blanco, "Modular microring laser cavity sensor," Opt. Express **29**(2), 1371–1383 (2021).

12. N. Boling, A. Glass, and A. Owyoung, "Empirical relationships for predicting nonlinear refractive index changes in optical solids," IEEE J. Quantum Electron. **14**(8), 601–608 (1978).

13. H. C. Frankis, Z. Su, Z. Su, N. Li, N. Li, E. S. Magden, M. Ye, M. R. Watts, M. R. Watts, and J. D. B. Bradley, "Four-Wave Mixing in a High-Q Aluminum Oxide Microcavity on Silicon," in *Conference on Lasers and Electro-Optics (2018)* (Optical Society of America, 2018), p. STh3I.3.

14. J. Mu, M. Dijkstra, Y.-S. Yong, M. de Goede, L. Chang, and S. M. García-Blanco, "Monolithic Integration of Al_2O_3 and Si_3N_4 Toward Double-Layer Active–Passive Platform," IEEE J. Sel. Top. Quantum Electron. **25**(5), 1–11 (2019).

15. J. Mu, M. Dijkstra, and S. M. García-Blanco, "Resonant Coupling for Active–Passive Monolithic Integration of Al_2O_3 and Si_3N_4," IEEE Photon. Technol. Lett. **31**(10), 771–774 (2019).

16. J. Mu, M. Dijkstra, J. Korterik, H. Offerhaus, and S. M. García-Blanco, "High-gain waveguide amplifiers in Si_3N_4 technology via double-layer monolithic integration," Photon. Res. **8**(10), 1634–1641 (2020).

17. C. I. van Emmerik, M. Dijkstra, M. de Goede, L. Chang, J. Mu, and S. M. Garcia-Blanco, "Single-layer active-passive Al_2O_3 photonic integration platform," Opt. Mater. Express **8**(10), 3049–3054 (2018).

18. D. V. Strekalov, C. Marquardt, A. B. Matsko, H. G. L. Schwefel, and G. Leuchs, "Nonlinear and quantum optics with whispering gallery resonators," J. Opt. **18**(12), 123002 (2016).

19. C. Reimer, M. Kues, P. Roztocki, B. Wetzel, F. Grazioso, B. E. Little, S. T. Chu, T. Johnston, Y. Bromberg, L. Caspani, D. J. Moss, and R. Morandotti, "Generation of multiphoton entangled quantum states by means of integrated frequency combs," Science **351**(6278), 1176–1180 (2016).

20. M.-G. Suh, X. Yi, Y.-H. Lai, S. Leifer, I. S. Grudinin, G. Vasisht, E. C. Martin, M. P. Fitzgerald, G. Doppmann, J. Wang, D. Mawet, S. B. Papp, S. A. Diddams, C. Beichman, and K. Vahala, "Searching for exoplanets using a microresonator astrocomb," Nat. Photonics **13**(1), 25–30 (2019).

21. A. L. Gaeta, M. Lipson, and T. J. Kippenberg, "Photonic-chip-based frequency combs," Nat. Photonics **13**(3), 158 (2019).

22. D. J. Moss, R. Morandotti, A. L. Gaeta, and M. Lipson, "New CMOS-compatible platforms based on silicon nitride and Hydex for nonlinear optics," Nat. Photonics **7**(8), 597–607 (2013).

23. G. Lin, A. Coillet, and Y. K. Chembo, "Nonlinear photonics with high-Q whispering-gallery-mode resonators," Adv. Opt. Photonics, AOP **9**(4), 828–890 (2017).

24. C. I. van Emmerik, W. A. P. M. Hendriks, M. M. Stok, M. de Goede, L. Chang, M. Dijkstra, F. Segerink, D. Post, E. G. Keim, M. J. Dikkers, and S.

M. García-Blanco, "Relative oxidation state of the target as guideline for depositing optical quality RF reactive magnetron sputtered Al_2O_3 layers," Opt. Mater. Express **10**(6), 1451–1462 (2020).

25. W. A. P. M. Hendriks, M. Dijkstra, C. I. van Emmerik, I. Hegeman, and S. M. G. Blanco, "High refractive index low-loss aluminium oxide waveguides," in (2020).

26. R. A. Gottscho, C. W. Jurgensen, and D. J. Vitkavage, "Microscopic uniformity in plasma etching," J. Vac. Sci. Technol. B **10**(5), 2133–2147 (1992).

27. D. R. Cote, S. V. Nguyen, A. K. Stamper, D. S. Armbrust, D. Tobben, R. A. Conti, and G. Y. Lee, "Plasma-assisted chemical vapor deposition of dielectric thin films for ULSI semiconductor circuits," IBM J. Res. Dev. **43**(1.2), 5–38 (1999).

28. I. M. White and X. Fan, "On the performance quantification of resonant refractive index sensors," Opt Express **16**(2), 1020–1028 (2008).

29. W. R. McKinnon, D.-X. Xu, C. Storey, E. Post, A. Densmore, A. Delâge, P. Waldron, J. H. Schmid, and S. Janz, "Extracting coupling and loss coefficients from a ring resonator," Opt. Express **17**(21), 18971–18982 (2009).

30. T. J. Kippenberg, A. L. Gaeta, M. Lipson, and M. L. Gorodetsky, "Dissipative Kerr solitons in optical microresonators," Science **361**(6402), (2018).

31. M. H. P. Pfeiffer, A. Kordts, V. Brasch, M. Zervas, M. Geiselmann, J. D. Jost, and T. J. Kippenberg, "Photonic Damascene process for integrated high-Q microresonator based nonlinear photonics," Optica **3**(1), 20–25 (2016).

32. P. Del'Haye, "Optical Frequency Comb Generation in Monolithic Microresonators," PhD Thesis, Ludwig-Maximilians-Universität München (2011).

33. T. Herr, "Solitons and dynamics of frequency comb formation in optical microresonators," École Polytechnique Fédérale de Lausanne (2013).

34. J. D. B. Bradley, F. Ay, K. Wörhoff, and M. Pollnau, "Fabrication of low-loss channel waveguides in Al_2O_3 and Y_2O_3 layers by inductively coupled plasma reactive ion etching," Appl. Phys. B **89**(2), 311–318 (2007).

35. X. Ji, F. A. S. Barbosa, S. P. Roberts, A. Dutt, J. Cardenas, Y. Okawachi, A. Bryant, A. L. Gaeta, and M. Lipson, "Ultra-low-loss on-chip resonators with sub-milliwatt parametric oscillation threshold," Optica **4**(6), 619–624 (2017).

36. H. E. Dirani, L. Youssef, C. Petit-Etienne, S. Kerdiles, P. Grosse, C. Monat, E. Pargon, and C. Sciancalepore, "Ultralow-loss tightly confining Si_3N_4 waveguides and high-Q microresonators," Opt. Express **27**(21), 30726–30740 (2019).

CHAPTER 6

Thick waveguides in low-stress stoichiometric silicon nitride on sapphire

Silicon nitride waveguides with an unprecedented thickness of up to 1350 nm and widths of 2200 nm were fabricated on a single LPCVD deposition step on sapphire substrates. The waveguides show calculated anomalous dispersion over a wide frequency range. Our process offers a new route to high confinement Si_3N_4 waveguides, enabling applications in nonlinear and mid-IR integrated photonics.

6.1 Introduction

Silicon nitride is one of the most used materials for integrated optics. It is transparent over a wide wavelength range (i.e., 400 to 6700 nm [1]) with channel losses below 1 dB/m having been experimentally reported [2]. Its high linear refractive index of $n{\sim}1.98$ at a wavelength of 1550 nm [3] and nonlinear refractive index of $n_2 = 2.5 \times 10^{-19}$ m^2W^{-1} at 1550 nm [4] in combination with the very low losses make Si_3N_4 an excellent material for the realization of nonlinear optical devices [5–9]. However, non-linear applications typically require channel waveguides exhibiting anomalous dispersion, which can only be achieved by highly confined Si_3N_4 channel waveguides of thicknesses above 700 nm [5,10]. Applications in the mid infrared (i.e., ~3.5 μm) also require thick Si_3N_4 layers of thicknesses above 300 nm [11].

Low-loss stoichiometric Si_3N_4 is typically deposited by low pressure chemical vapor deposition (LPCVD) on oxidized silicon substrates [12]. High residual tensile stress, frequently above 1 GPa [13–15] and dependent on process parameters, is present in these Si_3N_4 films [16], which limits the thickness of the deposited Si_3N_4 layer to typically <250-400 nm. Above this thickness, the layer is prone to cracking, either during or after deposition, severely limiting the performance of the devices. Several techniques have been developed to achieve high confinement thick Si_3N_4 waveguides. Gondarenko et. al. [17] developed a method by which crack-free layers of thicknesses up to 744 nm were deposited. Losses of 0.12 dB/cm were achieved in channel waveguides of 644 nm high and 900 nm wide. The proposed method consisted of sequential depositions of thin (< 400 nm) Si_3N_4 layers, followed by cooling down to room temperature. In another study by the same group, trenches were etched into the silicon substrate prior to Si_3N_4 deposition [18]. These trenches terminate any cracks in the Si_3N_4 layer that propagate from the substrate edge, and can be used to define a protected crack-free region for fabricating the devices. Waveguides up to 910 nm of thickness (deposited in two deposition steps of 400 nm and 510 nm followed by anneal at 1200 °C) were experimentally demonstrated with losses as low as 4.2 dB/m for a 1800 nm wide waveguide. Rotating the wafers by 45 deg after each deposition of 365 nm of Si_3N_4 was proposed by El Dirani et. al. to eliminate cracking due to the uniaxial strain accumulated in the Si_3N_4 film [15]. Propagation losses of channels 750 nm wide on 730 nm thick Si_3N_4 layers of 1.7 dB/cm were demonstrated. In a subsequent study, the same authors reduced dramatically the propagation losses of highly confined 1600 nm wide by 800 nm high Si_3N_4 waveguides by

implementing a chemical mechanical polishing step to reduce surface roughness of the layer and several annealing steps to reduce sidewall roughness and hydrogen content in the waveguides. Propagation losses as small as 3 dB/m were demonstrated [19].

The photonics damascene process, where deep trenches are dry etched into the thermal oxide layer of the silicon substrate and the Si_3N_4 is conformally deposited inside the trench [5,10] has been also proposed for the fabrication of highly confined thick Si_3N_4 waveguides with the potential for dispersion engineering. The residual Si_3N_4 on the substrate surface is then removed by chemical-mechanical polishing, resulting in Si_3N_4 waveguides embedded in the trenches. This process has yielded waveguide thicknesses up to 1.35 µm, although their width becomes limited by stress [10]. Furthermore, reflow of the trenches etched in the thermal oxide prior to LPCVD Si_3N_4 deposition has led to dramatic reduction of the propagation losses down to 0.05 dB/cm [20].

Finally, other approaches to achieve thick Si_3N_4 waveguides utilize low-temperature deposition methods. This includes liquid source CVD with TEOS as a precursor and a temperature of 150°C, resulting in a thickness of 900 nm [21], but with high propagation losses of 2.5 dB/cm. PECVD in pulsed LF/HF mode giving 580 nm layers [22,23] has also been used, with losses down to ~0.6 dB/cm.

Silicon dioxide has a limited transparency window, extending to ~3500 nm [1] limiting the extent of the frequency combs or continuum generation that can be achieved using the non-linear devices.

In this work we experimentally demonstrate low-loss highly confined Si_3N_4 waveguides of thickness 1.35 µm deposited in a single LPCVD step. Sapphire substrates are utilized, which drastically reduce the residual tensile stress present in the deposited Si_3N_4 films to ~120 MPa. Such low residual tensile stress increases the thickness at which cracks appear in the layer. Propagation losses <10 dB/cm have been measured in waveguide of cross-section 1500 nm × 590 nm. The proposed technology can find many interesting applications in the fields of non-linear photonics, mid-IR spectroscopy and visible light integrated photonics.

6.2 Characterization of thick Si$_3$N$_4$-on-sapphire layers

6.2.1 Layer deposition

Si$_3$N$_4$ layers of various thicknesses ranging from ~290 nm to 1335 nm were deposited on 675 µm thick SA100 monocrystalline sapphire substrates from Kyocera Fine Ceramics GmbH. The sapphire substrates are diced in the *c*-plane, and the flat is oriented perpendicular to the *a*-axis, with a tolerance of ±0.5°. The deposition was performed in a Tempress horizontal LPCVD furnace. Before deposition, the substrates were cleaned using ozone steam. The LPCVD deposition parameters were 22 sccm SiH$_2$Cl$_2$, 66 sccm NH$_3$, 800 °C and a pressure of 200 mTorr. Three depositions with deposition times of 60 minutes (1 wafer), 120 minutes (1 wafer) and 300 min (4 wafers) were performed. The Si$_3$N$_4$ layers were stripped from the backside of the sapphire wafers using reactive ion etching (RIE) in a custom-made parallel plate etcher.

A reference Si$_3$N$_4$ layer was deposited on a (100)-oriented double side polished silicon substrate with a deposition time of 120 minutes and a measured thickness of ~580 nm. Prior to Si$_3$N$_4$ deposition, the silicon wafer was dipped into an 1% HF solution for 60 seconds to remove the native oxide.

6.2.2 Layer thickness measurement

Ellipsometric measurements were performed using a J.A. Woollam M-2000UI ellipsometer with both a quartz tungsten halogen lamp and a deuterium lamp, covering the spectral range 400-1600 nm. The incident light was oriented in the *a-c* plane at angles of 65°, 70° and 75° from the substrate. Measurements were collected on 25 locations on each wafer, excluding the outer 1 cm. Each datapoint was fitted to a model consisting of a sapphire substrate ("Sapphire (ordinary)" provided by J.A. Woollam) and a layer following a generic Cauchy model, using *A*, *B*, *C* and the thickness as fit variables. Although sapphire is weakly birefringent and this model is only valid for a single angle of incidence, this model was selected because it achieved fits with lower mean square error (MSE) than other available models.

The measured Si$_3$N$_4$ thicknesses for the 6 wafers described above are given in Table 6.1, indicating the thickness and deposition rate both at the center and edge of the wafer. The thickness was found to be much less uniform for higher deposition times, with the average deposition rate slowing down significantly, especially at the wafer center. Furthermore, the thickness varies significantly from wafer to wafer at these longer deposition times within a single deposition

run. Wafers 3-6 were positioned in sequential order in the furnace, showing a deposition thickness gradient, likely specific to the particular LPCVD furnace utilized. No cracks were observed in any of the wafers upon inspection with grazing angle lighting, even several months after deposition. The 580 nm thick reference layer deposited on a silicon substrate exhibited a crack extending from the wafer flat.

Table 6.1: Thickness and deposition rate of the Si_3N_4 layers on sapphire, measured by ellipsometry.

Wafer number	1	2	3	4	5	6
Time [min]	60	120	300	300	300	300
t_{center} [nm]	289.7	584.3	1221	1282	1315	1331
t_{edge} [nm]	293.3	587.7	1319	1354	1376	1388
r_{center} [nm/min]	4.83	4.87	4.07	4.27	4.38	4.44
r_{edge} [nm/min]	4.89	4.90	4.40	4.51	4.59	4.63

The optimized Cauchy parameters at the center of wafer 6 are summarized in Table 6.2. While the optimization yields slightly different values for each point on the wafer, the differences are minute: The average refractive index and standard deviation at 633 nm are $2.0057 \pm 4.5 \times 10^{-4}$. At 1550 nm the average value is $1.9770 \pm 4.1 \times 10^{-4}$.

Table 6.2: Cauchy parameters, refractive index at 633 nm and 1550 nm, and thickness measured at the center of wafer 6.

A	1.971674
B [μm^2]	0.01266
C [μm^4]	0.000443
n_{633}	2.0060
n_{1550}	1.977
t [nm]	1331.5

6.3 Layer stress

The residual stress in the Si_3N_4 films was characterized by profilometric curvature measurements, using a Veeco Dektak 150. A height line trace is measured across the wafer (i.e., excluding the outer 1 cm) and leveled so that the outermost points are at zero height, permitting to obtain the wafer deflection. The wafer deflection is measured three times, namely before deposition, after deposition and after RIE removal of the Si_3N_4 layer from the backside of the wafer. The change in the deflection of the wafer is then studied

in order to gain understanding on the residual stress present on the Si_3N_4 layer.

Wafer deflection measurements were performed at in-plane rotation angles of 0°, 45°, 60°, 90° and 120° with respect to the flat to investigate the influence of the trigonal crystal structure of sapphire on the residual stress in the Si_3N_4 layers. The measurements revealed that the in-plane crystalline structure did not play an important role on the resulting film residual stress. Therefore, mean values with their standard deviation are reported.

Table 6.3 shows the change in measured wafer deflection, δ, of several sapphire wafers. δ is defined by the difference in deflection between the uncoated wafer, and after thick (~1.3 μm) LPCVD Si_3N_4 deposition and backside Si_3N_4 removal by RIE. Wafer 4 has been excluded because it had a wave-like curvature before deposition. This gave a deflection measurement with two dips, which is difficult to reliably analyze.

The change in wafer deflection is negative, which implies that the Si_3N_4 layer exhibits a tensile residual stress [24]. The error reported in the measured wafer deflection corresponds to the standard deviation of the 5 measurements carried out at the 5 different angles described above.

Table 6.3: Residual stress measurements of Si_3N_4 films deposited on sapphire and on a reference silicon wafer. Wafer 4 is not shown due to an abnormal deflection of the wafer prior to deposition, which makes the understanding of the stress measurements difficult.

	Si	Sapphire			
		Wafer 3	Wafer 5	Wafer 6	avg
Y_s [GPa]	130 [25]	430 [26]			
v_s	0.28 [25]	0.223 [27]			
t_s [μm]	525	675			
δ [μm]	-56.3	-2.97±0.07	-3.02±0.05	-3.00±0.1	-3.0±0.06
t_f [nm]	581	1260	1338	1354	1315
σ_f [MPa]	-1004	-124 ± 3	-118 ± 2	-116 ± 4	-119 ± 3

The residual stress in the Si_3N_4 film is calculated using Stoney's formula [28]:

$$\sigma_f = \frac{4}{3}\frac{Y_s}{(1-v_s)}\frac{t_s^2}{d^2}\frac{\delta}{t_f} \tag{6.1}$$

where, σ_f is the Si_3N_4 layer residual stress (in GPa), Y_s is the Young's modulus of the substrate (in GPa), v_s is the Poisson's ratio of the substrate, t_s is the

substrate thickness (in μm), d is the measurement length (in μm), δ is the change in deflection due to the deposition of the Si_3N_4 film (in nm) (i.e., the deflection of the film after Si_3N_4 deposition and backside stripping minus the deflection of the as-received sapphire substrate) and t_f is the thickness of the deposited Si_3N_4 layer (in nm). In these experiments the measurement length, d, was 80 mm.

The measured residual stress can be seen in the last row of Table 6.3. The thinner (~580 nm) Si_3N_4 layer deposited on silicon (column 2 of Table 6.3) exhibited a high residual tensile stress of ~1 GPa, comparable to layers in previous reports [13–15], which resulted in the onset of cracking. The measured residual stress on the ~1.3 μm thick Si_3N_4 layers on sapphire substrates is an order of magnitude lower, with an average of ~120 MPa. Such low residual tensile stress allows the direct deposition of thick Si_3N_4 layers without cracking.

The mechanism of residual stress reduction is probably thermal stress compensation. During the LPCVD deposition process, the Si_3N_4 layer is grown in a stretched-out state, i.e. under tensile intrinsic stress [24]. Since the LPCVD process takes place at high temperature (850 °C), the sapphire wafer is also in an expanded state during deposition. The wafer then compresses when it is cooled to room temperature after Si_3N_4 deposition. The deposited Si_3N_4 layer also compresses upon cooling.

Since the thermal expansion coefficient of sapphire (5.38×10^{-6} K^{-1} to 9.29×10^{-6} K^{-1} between 293 K and 1100 K) is larger than that of Si_3N_4 (1.79×10^{-6} K^{-1} [29]), the sapphire substrate applies a compressive thermal stress to the Si_3N_4 layer. The total residual stress can be calculated as the sum of the intrinsic stress and the thermal stress. The compressive thermal stress applied by the sapphire substrate is larger than the one applied by a silicon substrate, which has a coefficient of thermal expansion of 2.69×10^{-6} K^{-1} to 4.27×10^{-6} K^{-1} between 336 K and 1059 K [30]. Therefore, the residual stress is drastically reduced when depositing the Si_3N_4 films on sapphire substrates, as seen in the experimental results shown in Table 6.3. The thermal expansion of sapphire is isotropic in the c-plane, due to sapphire's threefold rotational symmetry.

The sapphire substrate curvature increased significantly after deposition, and stripping the backside layer relaxed the curvature to an intermediate value. As an example, wafer 4 initially had a concave curvature of 0.2 μm. After

deposition, the curvature increased to 5.9 µm, and after backside stripping the curvature decreased to 3.0 µm.

Because LPCVD process deposits the layers symmetrically on both sides of the substrate, it is normally assumed that the curvature should be equal before and after deposition. In practice there may be deviations from this assumption, although in this case the deviation is especially severe.

The temperature-stress curve of Si_3N_4 films on sapphire has been shown to cross zero close to room temperature by other researchers [29]. Deposition at a different temperature may shift this curve close to the zero point, or even past it, which makes a compressive residual stress plausible.

Because the backside of the sapphire substrate is unpolished, it is not suitable for either profilometric or ellipsometric measurements, and the backside layer is therefore not easily examined. However, it is plausible that the stress of a layer deposited on a severely rough surface is different than that on a smooth surface. A compressive backside layer stress would cause an exaggerated bow such as is seen in this work. Detailed characterization of the backside layer may be possible using a mapping optical technique such as k-space multi-beam optical sensor measurements [24,31].

6.4 Waveguide definition

Waveguides were defined in wafers 2 and 6 using Olin OiR 907-17 photoresist and contact UV-photolithography in an EV620 mask aligner with a broadband source. Etching of Si_3N_4 was performed in a Plasmatherm PT790 parallel plate etcher. The etching parameters were 100 sccm CHF_3, 9 sccm O_2, 40 mTorr chamber pressure and 250 W CCP power. The etch rate is 36 nm/minute in Si_3N_4 and around 3.5 nm/minute in sapphire.

Waveguide facets were defined by dicing, comparing two techniques: Wafer 2 was diced in a Loadpoint Micro Ace 3 dicing saw using Thermocarbon 2.187-12A blades with a 2000-grit roughness. These blades are not optimized for sapphire dicing, and several passes are necessary to cut through the 675 µm thick substrate. Most of the facets produced by this method were of low quality, although some were very smooth, as shown in Figure 6.1.
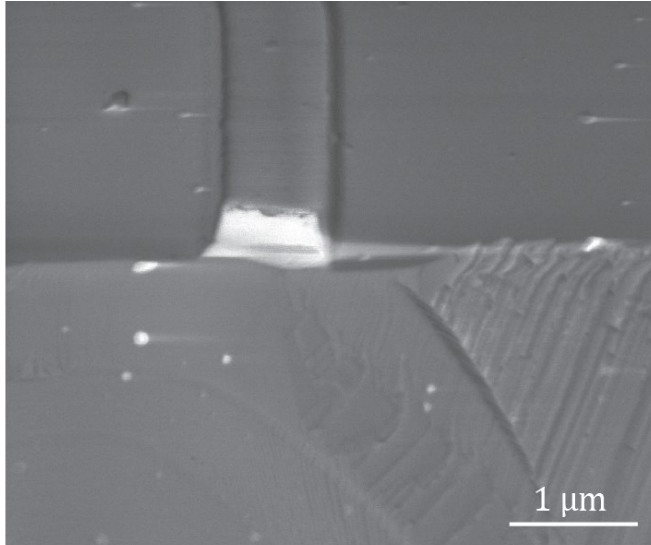
Figure 6.1: SEM image of the facet of a silicon nitride waveguide on a sapphire substrate created by dicing. The waveguide, which is the in-coupling taper, is 1 μm wide and 590 nm thick. The picture is distorted near the edges as an artifact of the SEM operating in high-resolution mode.

Wafer 6 was cladded after deposition in a 1 μm thick TEOS layer in a Tempress LPCVD furnace and was annealed at 1100°C to convert the TEOS to SiO_2. It was then singulated into individual dice. In order to achieve good quality end-facets, wafer 6 was partially diced from the backside to a limited depth, leaving untouched the top 220 μm of the sapphire, which was subsequently cleaved mechanically. The described partial dicing was performed in a Disco DAD3220 dicing saw using VT07-SD280-VC100-100 - 52 × 0.4 A3 × 40 - L dicing blades with a 280-grit roughness, designed specifically for sapphire dicing. The dicing was performed at a rotation speed of 20000 RPM and a dicing speed of 0.5 mm/s.

The resulting endfacets of the thick Si_3N_4 waveguide are shown in Figure 6.2. Figure 6.2 (a) shows the facet immediately after dicing. A small amount of flaking is visible, mostly originating in the SiO_2 cladding. Figure 6.2 (b) shows the same facet after focused ion beam (FIB) polishing. The waveguide cross-section can be clearly seen in this picture. The waveguide, with a nominal width of 2.4 μm on the photomask, has a top width of 2.2 μm, a base width of 2.7 μm, a height of 1.35 μm and sidewall angles of 80°. The widths are determined by SEM imaging and are subject to some uncertainty, however, the thickness was determined by profilometry before SiO_2 cladding and is highly accurate, on the order of a few nm.

Figure 6.3 shows a close-up image of the sidewall of the waveguide. Although some particles are visible, the sidewall roughness is low, which shows that deep etching is feasible without introducing serious defects.
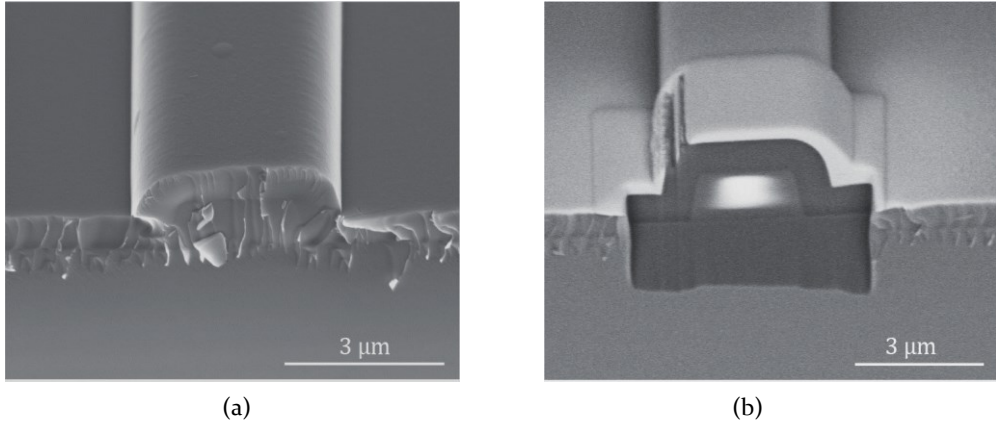

(a)   (b)

Figure 6.2: SEM image of the facet of a silicon nitride waveguide on a sapphire substrate created by partial backside dicing and cleaving. (a) The facet immediately after dicing. Small amounts of roughness are visible, mostly from the TEOS SiO_2 cladding. (b) The same facet after FIB polishing. The waveguide is 1.35 µm thick, width a base width of 2.7 µm, a top width of 2.2 µm and a sidewall angle of 80°. The nominal width on the photomask is 2.4 µm. A layer of platinum is deposited in the FIB before cross-sectioning to improve the image quality.
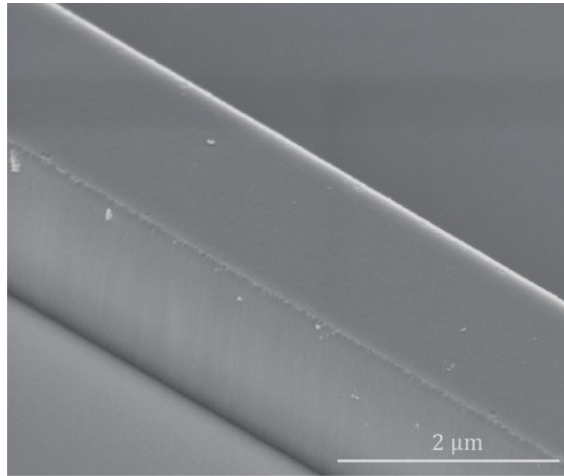
Figure 6.3: SEM image of the sidewall of a 1.35 µm thick Si_3N_4 waveguide on sapphire.

6.5 Optical mode simulations

The optical modes supported by the Si_3N_4 on sapphire waveguides were simulated using finite difference eigenmode (FDE) analysis in Ansys Lumerical MODE. The Cauchy parameters shown in Table 6.2 were utilized in the simulations for the Si_3N_4. Sapphire was modeled using data from Palik [32].

The 1.5 µm wide, 590 nm thick waveguide shows 10 TE and 10 TM modes at a wavelength of 633 nm. The single mode cutoff wavelength for both TE and TM is at 1.15 µm and the propagation cutoff is 1.8 µm. The waveguide shows exclusively normal dispersion.

The 2.2 µm wide, 1350 nm thick, cladded waveguide shown in Figure 6.2 supports 3 TE and 3 TM modes at a wavelength of 1550 nm. The single-mode cutoff wavelength for TE is 2.25 µm and the propagation cutoff is 5 µm, allowing operation throughout the transparency window of sapphire [33]. In order to fully benefit from this extended operating range, the SiO_2 cladding should in the future be removed, or exchanged for a material with mid-IR transparency, such as Al_2O_3.

The calculated second order dispersion of the waveguide is shown in Figure 6.4. Both the fundamental TE and TM modes show anomalous dispersion from a wavelength of around 1.3 µm into the mid-infrared, making them suitable for nonlinear frequency conversion. The TM mode has two zero-dispersion wavelengths, at 1.29 µm and 2.66 µm. The TE mode, however, has one zero-dispersion wavelength at 1.34 µm, with the dispersion remaining anomalous until at least 5 µm. However, we note that these calculated values are sensitive to the material models used in the simulation, and might not be highly reliable outside the spectral region where the refractive index was measured, in this case 400 nm-1600 nm.

The effective mode area A_{eff} of the fundamental TE mode is 2.3 µm^2 at a wavelength of 1.55 µm, calculated by Equation (1.3):

$$A_{\text{eff}} = \frac{(\iint |E|^2 dx dy)^2}{\iint |E|^4 dx dy} \qquad (1.3)$$

This yields a nonlinear parameter, γ, of 0.42 W^{-1}cm^{-1}. This is somewhat lower than values achieved in photonic damascene processes, typically

1-1.4 W^{-1}cm^{-1} [5,7]. The reason for the decrease is the larger mode area of the Si$_3$N$_4$ on sapphire waveguides, however this may be optimized in the future.
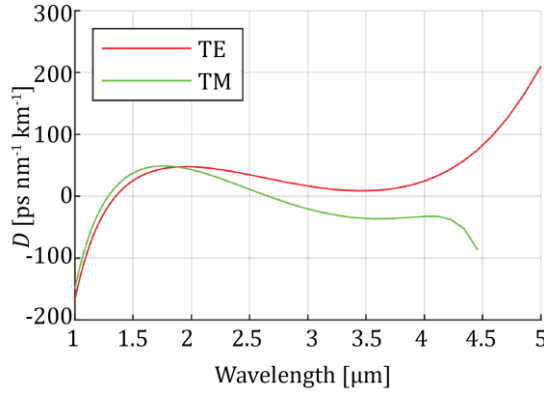

Figure 6.4: Calculated second order dispersion parameter, $D(\lambda)$, for the fundamental TE and TM modes of a 2.2 μm wide, 1350 nm thick Si$_3$N$_4$ waveguide on sapphire with 1 μm thick SiO$_2$ cladding. Both modes exhibit low, anomalous dispersion from around 1.3 μm into the mid-infrared. The fundamental TE mode shows anomalous dispersion throughout the transparency range.

6.6 Optical characterization

The 590 nm thick, 1.5 μm wide uncladded waveguide was coupled into using a free-space coupling setup, using a 633 nm HeNe laser. The waveguide was imaged from above using a BFLY-U3-23S6M-C monochrome CMOS camera. The microscope image used for the following measurements is shown in Figure 6.5.
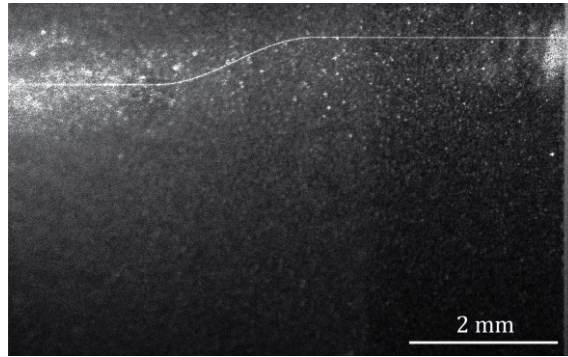
Figure 6.5: Microscope image of light at a wavelength of 633 nm propagating in a 1.5 μm wide, 590 nm thick uncladded waveguide. The light propagates from left to right.

Due to the short length of the waveguide and the significant scattered background light, it is not feasible to accurately determine the losses. With significant filtering and background removal it is possible to find loss values on the order of several dB/cm at 633 nm, however the exact value depends strongly on the start and endpoints of the sampled data. These values, although highly uncertain, are plausible due to the short wavelength, lack of cladding and the high number of modes present. Improvements in the measurements may be achieved by using a longer spiral waveguide configuration and reducing the background scattered light. This may be achieved in the cleaved waveguides with improved facets.

6.7 Conclusion

Stoichiometric LPCVD silicon nitride layers with a thickness up to 1388 nm have been deposited in a single deposition step on sapphire substrates without cracking. The measured residual tensile stress of the Si_3N_4 film was 119 MPa, which is a reduction of 88% compared to thick Si_3N_4 layers on silicon. Crack-free waveguides with predicted anomalous dispersion were patterned in 1350 nm thick Si_3N_4 layers. Propagation has been demonstrated in 590 nm thick waveguides. These findings open the door to a new material platform for non-linear integrated optics, leveraging established fabrication technology and extending the Si_3N_4 operating window into the mid-infrared, up to 5.5 μm.

Bibliography

1. R. Soref, "Mid-infrared photonics in silicon and germanium," Nat. Photonics **4**(8), 495–497 (2010).
2. X. Ji, F. A. S. Barbosa, S. P. Roberts, A. Dutt, J. Cardenas, Y. Okawachi, A. Bryant, A. L. Gaeta, and M. Lipson, "Ultra-low-loss on-chip resonators with sub-milliwatt parametric oscillation threshold," Optica **4**(6), 619–624 (2017).
3. J. Mu, M. Dijkstra, Y.-S. Yong, M. de Goede, L. Chang, and S. M. García-Blanco, "Monolithic Integration of Al_2O_3 and Si_3N_4 Toward Double-Layer Active–Passive Platform," IEEE J. Sel. Top. Quantum Electron. **25**(5), 1–11 (2019).
4. A. L. Gaeta, M. Lipson, and T. J. Kippenberg, "Photonic-chip-based frequency combs," Nat. Photonics **13**(3), 158 (2019).
5. M. H. P. Pfeiffer, A. Kordts, V. Brasch, M. Zervas, M. Geiselmann, J. D. Jost, and T. J. Kippenberg, "Photonic Damascene process for integrated high-Q microresonator based nonlinear photonics," Optica **3**(1), 20–25 (2016).
6. M. H. P. Pfeiffer, C. Herkommer, J. Liu, H. Guo, M. Karpov, E. Lucas, M. Zervas, and T. J. Kippenberg, "Octave-spanning dissipative Kerr soliton frequency combs in Si_3N_4 microresonators," Optica **4**(7), 684–691 (2017).
7. J. P. Epping, T. Hellwig, M. Hoekman, R. Mateman, A. Leinse, R. G. Heideman, A. van Rees, P. J. M. van der Slot, C. J. Lee, C. Fallnich, and K.-J. Boller, "On-chip visible-to-infrared supercontinuum generation with more than 495 THz spectral bandwidth," Opt. Express **23**(15), 19596–19604 (2015).
8. Y. Okawachi, K. Saha, J. S. Levy, Y. H. Wen, M. Lipson, and A. L. Gaeta, "Octave-spanning frequency comb generation in a silicon nitride chip," Opt. Lett. **36**(17), 3398–3400 (2011).
9. M. A. G. Porcel, F. Schepers, J. P. Epping, T. Hellwig, M. Hoekman, R. G. Heideman, P. J. M. van der Slot, C. J. Lee, R. Schmidt, R. Bratschitsch, C. Fallnich, and K.-J. Boller, "Two-octave spanning supercontinuum generation in stoichiometric silicon nitride waveguides pumped at telecom wavelengths," Opt. Express **25**(2), 1542–1554 (2017).
10. J. P. Epping, M. Hoekman, R. Mateman, A. Leinse, R. G. Heideman, A. van Rees, P. J. M. van der Slot, C. J. Lee, and K.-J. Boller, "High confinement, high yield Si_3N_4 waveguides for nonlinear optical applications," Opt. Express **23**(2), 642–648 (2015).
11. P. Muñoz, G. Micó, L. A. Bru, D. Pastor, D. Pérez, J. D. Doménech, J. Fernández, R. Baños, B. Gargallo, R. Alemany, A. M. Sánchez, J. M. Cirera,

R. Mas, and C. Domínguez, "Silicon Nitride Photonic Integration Platforms for Visible, Near-Infrared and Mid-Infrared Applications," Sensors **17**(9), 2088 (2017).

12. K. Wörhoff, R. G. Heideman, A. Leinse, and M. Hoekman, "TriPleX: a versatile dielectric photonic platform," Adv. Opt. Technol. **4**(2), 189–207 (2015).

13. S. Hong, T. P. Weihs, J. C. Bravman, and W. D. Nix, "Measuring stiffnesses and residual stresses of silicon nitride thin films," JEM **19**(9), 903 (1990).

14. M. Melchiorri, N. Daldosso, F. Sbrana, L. Pavesi, G. Pucker, C. Kompocholis, P. Bellutti, and A. Lui, "Propagation losses of silicon nitride waveguides in the near-infrared range," Appl. Phys. Lett. **86**(12), 121111 (2005).

15. H. El Dirani, A. Kamel, M. Casale, S. Kerdiles, C. Monat, X. Letartre, M. Pu, L. K. Oxenløwe, K. Yvind, and C. Sciancalepore, "Annealing-free Si_3N_4 frequency combs for monolithic integration with Si photonics," Appl. Phys. Lett. **113**(8), 081102 (2018).

16. N. Daldosso, M. Melchiorri, F. Riboli, M. Girardini, G. Pucker, M. Crivellari, P. Bellutti, A. Lui, and L. Pavesi, "Comparison among various Si_3N_4 waveguide geometries grown within a CMOS fabrication pilot line," J. Light. Technol. **22**(7), 1734–1740 (2004).

17. A. Gondarenko, J. S. Levy, and M. Lipson, "High confinement micron-scale silicon nitride high Q ring resonator," Opt. Express **17**(14), 11366–11370 (2009).

18. K. Luke, A. Dutt, C. B. Poitras, and M. Lipson, "Overcoming Si_3N_4 film stress limitations for high quality factor ring resonators," Opt. Express, OE **21**(19), 22829–22833 (2013).

19. H. E. Dirani, L. Youssef, C. Petit-Etienne, S. Kerdiles, P. Grosse, C. Monat, E. Pargon, and C. Sciancalepore, "Ultralow-loss tightly confining Si_3N_4 waveguides and high-Q microresonators," Opt. Express **27**(21), 30726–30740 (2019).

20. M. H. P. Pfeiffer, J. Liu, A. S. Raja, T. Morais, B. Ghadiani, and T. J. Kippenberg, "Ultra-smooth silicon nitride waveguides based on the Damascene reflow process: fabrication and loss origins," Optica **5**(7), 884–892 (2018).

21. X. Cheng, J. Hong, A. M. Spring, and S. Yokoyama, "Fabrication of a high-Q factor ring resonator using LSCVD deposited Si_3N_4 film," Opt. Mater. Express **7**(7), 2182–2187 (2017).

22. K. Ikeda, R. E. Saperstein, N. Alic, and Y. Fainman, "Thermal and Kerr nonlinear properties of plasma-deposited silicon nitride/silicon dioxide waveguides," Opt. Express **16**(17), 12987–12994 (2008).

23. L. Wang, W. Xie, D. V. Thourhout, Y. Zhang, H. Yu, and S. Wang, "Nonlinear silicon nitride waveguides based on a PECVD deposition platform," Opt. Express **26**(8), 9645–9654 (2018).
24. N. Sharma, M. Hooda, and S. K. Sharma, "Stresses in thin films: an experimental study," Indian. J. Phys. **93**(2), 159–167 (2019).
25. M. A. Hopcroft, W. D. Nix, and T. W. Kenny, "What is the Young's Modulus of Silicon?," J. Microelectromech. Syst. **19**(2), 229–238 (2010).
26. J. B. Wachtman, W. E. Tefft, D. G. Lam, and R. P. Stinchfield, "Elastic Constants of Synthetic Single-Crystal Corundum at Room Temperature," J. Am. Ceram. Soc. **43**(6), 334–334 (1960).
27. L. Wheeler, C. Y. Guo, L. Wheeler, Cliff, and Y. Guo, "Symmetry analysis of extreme areal Poisson's ratio in anisotropic crystals," J. Mech. Mater. Struct. **2**(8), (2007).
28. G. G. Stoney and C. A. Parsons, "The tension of metallic films deposited by electrolysis," Proc. R. Soc. Lond. A **82**(553), 172–175 (1909).
29. S. Habermehl, "Coefficient of thermal expansion and biaxial Young's modulus in Si-rich silicon nitride thin films," J. Vac. Sci. Technol. A **36**(2), 021517 (2018).
30. Y. Okada and Y. Tokumaru, "Precise determination of lattice parameter and thermal expansion coefficient of silicon between 300 and 1500 K," J. Appl. Phys. **56**(2), 314–320 (1984).
31. E. Chason, "Resolution and sensitivity of stress measurements with the k-Space Multi-beam Optical Sensor (MOS) system," Sandia National Laboratories (2005).
32. E. D. Palik, *Handbook of Optical Constants of Solids* (Academic Press, 1998).
33. E. R. Dobrovinskaya, L. A. Lytvynov, and V. Pishchik, *Sapphire: Material, Manufacturing, Applications* (Springer US, 2009).

CHAPTER 7

Conclusion

Progress is brought about by two forms of innovation: One is the invention of devices, and the other is the invention of tools. This thesis falls into the latter category. In this work, we advance the fabrication technology for the three material systems $KY(WO_4)_2$, Al_2O_3, and Si_3N_4. The goal has been to develop structures appropriate for third-order nonlinear optics, with Kerr frequency combs being the main target. These structures have taken the form of ~μm-sized high index contrast waveguides.

In Chapters 2-3, we have investigated techniques to structure $KY(WO_4)_2$ beyond what has been shown before. This material is used for high performance lasers and amplifiers, however nearly all existing waveguides are either in slab or low contrast waveguide configurations. Our goal has been to advance lithography and etching in order to create high index contrast waveguides, as well as resonator structures, both of which will improve efficiency. To this end, we create narrower and deeper etched waveguides than in other work, and achieve smooth, redeposition-free sidewalls. Importantly, we have demonstrated a HCl wet etching process for redeposited $KY(WO_4)_2$, even though $KY(WO_4)_2$ is widely considered impervious to chemical etching. This process lets us strip redeposition from sidewalls, which easily and effectively dissolves a problem that has caused great problems for previous researchers. We also develop a chuck that reduces the problem of photoresist edge bead on small samples, and a chuck for contact lithography that reduces the risk of sample or mask damage.

In Chapter 4, we implement a variation on the wet etch process of Chapter 3 on swift heavy ion irradiated $KY(WO_4)_2$. This ion irradiation process creates an amorphous sub-surface layer while leaving the top 1 μm $KY(WO_4)_2$ crystal

structure intact. Similar to redeposited $KY(WO_4)_2$, the amorphous layer is chemically susceptible to etching, whereas the crystalline is not. When used after a focused ion beam milling step, the process can therefore etch horizontally, but not vertically. This gives an underetch and lets us produce disks that stand on small pedestals in the very same piece of material from which they were made.

In Chapter 5, we have created high-Q Al_2O_3 resonators with anomalous dispersion, an important step towards Kerr frequency combs in this emerging material. Our Al_2O_3 has a higher refractive index than is commonly reported for amorphous layers, which indicates that it may be polycrystalline. We have achieved losses down to 0.48 dB/cm and Q-factors of 767000. SEM images reveal some sidewall roughness and surface defects, which indicates that the losses may be improved by standard processes like chemical-mechanical polishing, and electron beam lithography rather than photolithography. In their current state, the threshold pump power for comb generation of 478 mW is too high for practical use. However, this is the first demonstration of high refractive index Al_2O_3, and as the fabrication technique is optimized the losses will go down, taking the threshold power down with them.

In Chapter 6 we have demonstrated a novel material system, namely Si_3N_4 on sapphire. Si_3N_4 is an excellent material for nonlinear integrated optics, but high stress limits the layer thickness and makes dispersion engineering challenging. Depositing the Si_3N_4 on sapphire rather than on oxidized silicon bypasses this challenge by reducing the layer stress by 88%. In a single step we deposit 1350 nm thick layers and etch completely through to create dispersion engineered waveguides only using standard techniques.

In summary, this work presents several new techniques that advance the state of the art in three promising material systems. The parameter space for design in $KY(WO_4)_2$ and Al_2O_3 is greater than ever, and unprecedented thick layers of Si_3N_4 are now available.

APPENDIX

Derivation of D_1 and D_2 in integrated dispersion

In waveguide structures, dispersion is a relatively straightforward concept: Looking at Equation (1.4), the propagation constant β has a wavelength dependence, and the dependence on ω_1, ω_2, ω_3, and so forth constitute the first, second, third, and higher order dispersion terms:

$$\beta(\omega) = \beta_0 + \beta_1(\omega - \omega_0) + \frac{1}{2}\beta_2(\omega - \omega_0)^2 + \cdots, \qquad (1.4)$$

$$\beta_m = \left(\frac{d^m\beta}{d\omega^m}\right)_{\omega_0} \qquad (1.5)$$

β_0 is linked to the effective index n_{eff}, β_1 to the group index n_{g}, β_2 to the dispersion parameter D and so forth. These terms are intimately linked with the mode spacing of a ring resonator. However, a resonator may be more complex than a straight waveguide. For example, a racetrack resonator has both straight and bent sections, which have different values of $\beta(\omega)$.

The integrated dispersion approach solves this added complication by considering only the mode spacing itself, decoupled from the propagation constant. However, it is not immediately obvious that the D_2 term corresponds to the dispersion parameter D, nor that a positive D_2 indicates anomalous dispersion:

$$\omega_\mu = \omega_0 + \sum_j D_j\mu^j\Big/j! \qquad (1.25)$$

We will here motivate the use of integrated dispersion by analyzing the simple case of a ring resonator with roundtrip length L. We first consider the frequency dependence of the free spectral range, neglecting all terms above β_2 in equation (1.4):

$$FSR_\omega(\omega) = \frac{c}{n_g(\omega)L} = \frac{2\pi}{L}\left(\frac{d\beta(\omega)}{d\omega}\right)^{-1}$$

$$= \frac{2\pi}{L}\left(\frac{d}{d\omega}\left(\beta_0 + \beta_1(\omega - \omega_0) + \frac{1}{2}\beta_2(\omega - \omega_0)^2\right)\right)^{-1}$$

$$= \frac{2\pi}{L}\left(\beta_1 + \beta_2(\omega - \omega_0)\right)^{-1} \tag{A.1}$$

Evaluating $FSR_\omega(\omega)$ at the center frequency ω_0 yields

$$FSR_\omega(\omega_0) = \frac{2\pi}{L\beta_1} \equiv \Delta\omega \tag{A.2}$$

To evaluate $FSR_\omega(\omega)$ at the resonance frequencies ω_μ, we make the assumption that $\omega_\mu = \omega_0 + \mu\Delta\omega$. While this seems contrary to the goal of examining the second order dispersion, it is only a small deviation in the frequency at which $FSR_\omega(\omega_\mu)$ is evaluated, with negligible influence on its actual value.

$$FSR_\omega(\omega_\mu) = \frac{2\pi}{L}\left(\beta_1 + \mu\beta_2\Delta\omega\right)^{-1} \tag{A.3}$$

The values of ω_μ can now be obtained by summing every FSR_ω from ω_0 to ω_μ. However, performing a summation of (A.3) over μ is not trivial, and to simplify this expression, we perform a Taylor expansion to first order:

$$FSR_\omega(\omega_\mu) \approx \frac{2\pi}{L}\left(\frac{1}{\beta_1} - \frac{\mu\beta_2\Delta\omega}{\beta_1^2}\right) = \frac{2\pi}{L}\frac{1}{\beta_1} - \left(\frac{2\pi}{L}\right)^2\frac{\mu\beta_2}{\beta_1^3} \tag{A.4}$$

$$\Rightarrow \omega_\mu = \omega_0 + \sum_{\mu'=0}^{\mu-1} FSR_\omega(\omega_{\mu'}) \tag{A.5}$$

$$\approx \omega_0 + \sum_{\mu'=0}^{\mu-1}\left(\frac{2\pi}{L}\frac{1}{\beta_1} - \left(\frac{2\pi}{L}\right)^2\frac{\mu'\beta_2}{\beta_1^3}\right) \tag{A.6}$$

$$= \omega_0 + \left(\mu \frac{2\pi}{L} \frac{1}{\beta_1} + \frac{(\mu - \mu^2)}{2} \left(\frac{2\pi}{L} \right)^2 \frac{\beta_2}{\beta_1^3} \right) \tag{A.7}$$

$$= \omega_0 + \mu \left(\frac{2\pi}{L} \frac{1}{\beta_1} + \frac{1}{2} \left(\frac{2\pi}{L} \right)^2 \frac{\beta_2}{\beta_1^3} \right) - \frac{1}{2} \mu^2 \left(\frac{2\pi}{L} \right)^2 \frac{\beta_2}{\beta_1^3} \tag{A.8}$$

$$\approx \omega_0 + \mu \frac{2\pi}{L} \frac{1}{\beta_1} - \frac{1}{2} \mu^2 \left(\frac{2\pi}{L} \right)^2 \frac{\beta_2}{\beta_1^3} \tag{A.9}$$

Comparing (A.9) with (1.25), we separate the terms proportional to μ and μ^2:

$$D_1 = \frac{2\pi}{L\beta_1} = FSR_\omega(\omega_0) \tag{A.10}$$

$$D_2 = - \left(\frac{2\pi}{L} \right)^2 \frac{\beta_2}{\beta_1^3} \tag{A.11}$$

This proportionality of D_2 to $-\beta_2$ proves that D_2 is a measure of second-order dispersion in a ring resonator, and that a positive value of D_2 indicates anomalous dispersion. Furthermore, the value of β_2 can be calculated by

$$\beta_2 = - \frac{n_g}{c} \frac{D_2}{D_1^2} \tag{A.12}$$

Scientific output

Peer-reviewed papers

- S. M. Martinussen, R. N. Frentrop, M. Dijkstra, F. Segerink, V. Tormo-Márquez, J. Olivares, and S. M. Garcia-Blanco, "Pedestal microdisks in potassium yttrium double tungstate," Opt. Mater. Express **9**(8), 3371–3378 (2019).

  Included as Chapter 4.

- S. M. Martinussen, R. N. Frentrop, M. Dijkstra, and S. M. Garcia-Blanco, "Redeposition-Free Deep Etching in Small $KY(WO_4)_2$ Samples," Micromachines **11**(12), 1033 (2020).

  Included as Chapter 3.

- S. Martinussen, W.A.P.M. Hendriks, M. Dijkstra, N. Schilder, C. van Emmerik, M. Stok, and S. M. Garcia-Blanco, "High-Q Al_2O_3 racetrack resonators with anomalous dispersion", in preparation.

- S. Martinussen, E. Berenschot, R. Tiggelar, W. Hendricks, R. Frentrop, L. Chang, M. Dijkstra, B. Borgelink, N. Tas, S. M. Garcia-Blanco, "Thick waveguides in low-stress stoichiometric silicon nitride on sapphire," in preparation.

Conference contributions

- S. M. Martinussen, M. Dijkstra, S. M. Garcia-Blanco, and Optical Sciences, "Reducing redeposition on KYW waveguides through hard mask engineering," in 22nd Annual Symposium of the IEEE Photonics Benelux Chapter (2017).

- S. M. Martinussen, R. N. Frentrop, M. Dijkstra, F. Segerink, V. Tormo-Márquez, J. Olivares, and S. M. Garcia-Blanco, "Pedestal disk resonator in potassium yttrium double tungstate," Proc. SPIE (2018), **10535**.

- S. Martinussen, M. Dijkstra, and S. G. Blanco, "Roughness reduction through chemical etching of amorphized residues," in Photonics Event, Veldhoven, Netherlands (2017), poster presentation.

- S. M. Martinussen, R. N. Frentrop, and S. M. Garcia-Blanco, "Design of pedestal disk resonators in $KY(WO_4)_2$ for Kerr frequency combs," in 23rd Annual Symposium of the IEEE Photonics Benelux Chapter (2018).

- C. I. van Emmerik, S. M. Martinussen, J. Mu, M. Dijkstra, R. Kooijman, and S. M. Garcia-Blanco, "A novel polishing stop for accurate integration of potassium yttrium double tungstate on a silicon dioxide platform," Proc SPIE (2018), **10535**.

     Contributed to design and fabrication.

- C.I. van Emmerik, S.M. Martinussen, J. Mu, M. Dijkstra, S.M. García Blanco, "A novel polishing stop for accurate integration of potassium yttrium double tungstate on silicon dioxide," Proc. 22th Annu. Symp. IEEE Photonics Society Benelux Chapter, Delft (2017)

     Contributed to design and fabrication.

- C. I. van Emmerik, S. M. Martinussen, J. Mu, M. A. Sefünc¸ M. Dijkstra, S. M. Garcia-Blanco, "Toward highly confined potassium double tungstate waveguides for laser applications," Proc. 21th Annu. Symp. IEEE Photonics Society Benelux Chapter, Ghent (2016)

     Contributed to design and fabrication.

Acknowledgements

As this chapter of my life comes to a close, I look back at it with gratitude, pride and fondness. I have gone through a great deal of personal and professional development, and it is in no small part because of the wonderful people I have been surrounded by.

Sonia, thank you for bringing me here and for your supervision over the past five years. You have granted me a lot of freedom in my research, and your perpetually optimistic and motivating leadership has pushed me through many challenging moments. **Jennifer** and **Herman**, thank you for always being available and for fostering my curiosity. Together, the three of you and your human-centered leadership has created a working environment that stresses the importance of personal well-being and mental health.

The other PhD students in the RENOS team, **Carlijn** and **Raimond**, have been my closest collaborators and intellectual sparring partners. Thank you for countless hours of brainstorming experiments, interpreting results and piecing together the puzzle of our parallel projects. **Meindert's** advice on everything cleanroom related has been critically important at every step along the way. Without you OS would grind to a halt.

Jeroen, thank you for our long and interesting discussions about everything from optics to audio. **Frans**, your steady hands and infinite patience defy all laws of engineering. **Karen**, thank you for keeping everything running smoothly and keeping the bureaucracy at a safe distance from the rest of us.

Ward, it's been great training, teaching, lecturing about coffee and working with you. One day I'll beat you at the Thorlabs challenge. I'm grateful to **Lantian** for all your help inside and outside the lab. **Pablo**, teaching together with you taught me a lot. **Ivo**, thank you for your help with my thesis. **Jose**, you have improved my time here with your food, dance and the great people you've brought over. **Sergio** and **Mustafa**, you were invaluable helping me get up to speed during my first months here. **Vlad**, **Rafa**, **Hosein**, **Ewoud**, **Lisanne**, and everyone else, thank you for contributing to my experience at OS. **Yean-Sheng**, thank you for everything.